RF POWER AND SIGNAL TRANSMISSION IN PARTICLE ACCELERATORS

by

Ezgi Sunar

B.S., Physics, Boğaziçi University, 2018

Submitted to the Institute for Graduate Studies in
Science and Engineering in partial fulfillment of
the requirements for the degree of
Master of Science

Graduate Program in Physics

Boğaziçi University

2018

I want to dedicate my thesis to my beloved parents,

Aylin & Engin Sunar

ACKNOWLEDGEMENTS

First of all, I would like to thank Christine Vollinger for accepting me in her team as a technical student and letting me take a part in her studies. She shared her knowledge and experience during our studies. I sincerely want to thank my colleagues in the team, starting with Aaron Farricker, Branko Popovic, Patrick Kramer, Nasrin Nasresfahani and all the other BE-RF-BR section members. When I have had a problem or a question, they have always answered or solved them with a great patience.

I would also like to thank Salim Ogur and all KAHVE Laboratory members who taught me a lot of things as being an accelerator physicist as well as an experimental physicist. I also want to thank to my professors at Bogazici University, especially to my referees; M. Burcin Unlu and M. Naci Inci.

I would like to express my great thankfulness to my two supervisors; *Erkcan Ozcan* and *Gokhan Unel*. They are not only my academic mentors but also the people whose opinions I care in every perspective. They always teach me how to look at my life in a different way and they contribute to my personal development with their life perspectives. I have learnt from them how to be an experimental physicist and an ethical scientist.

Last but not least, I have the greatest appreciation to my beloved family for being always with me and supporting me at every step in my life. I am thankful to them for believing in me.

ABSTRACT

RF POWER AND SIGNAL TRANSMISSION IN PARTICLE ACCELERATORS

RF waves have key applications for particle accelerators in transmitting both signal and power. In this thesis, we summarize work covering both of these complementary functions of the RF waves, applied to two separate projects. One of the projects is the design and construction of an RF transmission line and circulator at the KAHVE Laboratory of Boğaziçi University. As part of this project, we describe simulations and characterization measurements of various power transmission line components running at 800 MHz. The second project is about the developing a methodology that would allow in-situ determination of the presence of previously installed shields used in bellows connected to beam pickup monitors on the CERN SPS accelerator, and confirmation of whether their performance is adequate in eliminating 1.3GHz intrinsic resonance arising from the limits of the longitudinal beam coupling impedance. For both projects, detailed simulations have been performed and compared to the measurements and the obtained results are in line with the project targets.

ÖZET

PARÇACIK HIZLANDIRICILARINDA RF GÜÇ VE SİNYAL İLETİMİ

Parçacık hızlandırıcılarında RF dalgaları sinyal ve güç iletiminde anahtar roller oynar. Bu tezde, RF dalgaların bu iki eşlenik fonksiyonun uygulaması olan iki ayrı projedeki çalışmalar sunulmaktadır. Projelerden biri, Boğaziçi Üniversite'sindeki KAHVE Laboratuvarı'nda inşa edilmekte olan bir RF iletim hattı ve dolaştırıcının modellenip kurulmasıdır. Bu projenin bir parçası olarak 800 MHz'de çalışacak şekilde tasarlanan çeşitli iletim hattı elemanlarının bilgisayarla benzetimleri ve karakteristik ölçümleri gerçekleştirilmiştir. İkinci proje ise, CERN'deki SPS hızlandırıcısı üzerindeki demet ölçüm ekranlarına bağlı metal körüklerin kimilerinin içlerine daha önceden monte edilmiş zırhların varlığını belirleyecek bir yöntemin geliştirilmesi ve ayrıca bu zırhların SPS'nin eksenel demet eşleşme empedansı kaynaklı oluşan 1.3 GHz'deki rezonansın giderilmesinde yeterli olup olmadığına karar verilmesi üzerinedir. Her iki projede de yapılan detaylı benzetim çalışmaları deneysel ölçümlerle karşılaştırılmış ve hedeflenen amaçlara ulaşılmıştır.

TABLE OF CONTENTS

LIST OF FIGURES

LIST OF TABLES

LIST OF SYMBOLS

f_c	Cutoff frequency
f_{res}	Resonance frequency
$Q-$ factor	Quality factor
Q_{ext}	External quality factor
Q_L	Loaded quality factor
Q_0	Unloaded quality factor
R_s	Shunt impedance
R_s/Q	Characteristic impedance
w	Angular frequency
w_{res}	Angular frequency at one resonance mode
β	$\frac{v}{c}$, Speed as a fraction of the speed of light
β_c	Cutoff wave number
β_{coup}	Cavity coupling coefficient
δ	Skin depth
λ	Wavelength

LIST OF ACRONYMS/ABBREVIATIONS

CERN	The European Organization for Nuclear Research
CST MWS	Computer Simulation Technology Microwave Studio
DUT	Device under test
EM-Field	Electromagnetic Field
HOM	Higher Order Mode
Hi-Lumi/HL-LHC	High Luminosity LHC
LIU-Project	LHC Injectors Upgrade Project
LHC	Large Hadron Collider
MBA	Main Bending Magnet after coming QF-magnet
MBA	Main Bending Magnet
PS	Proton Synchrotron
QF	Quadrupole Focusing Magnet
QF	Quadrupole Focusing
RF	Radio Frequency
RLC circuit	An electrical circuit consisting of a capacitor, a resonator and an inductor
S-parameter	Scattering parameter
SPS	Super Proton Synchrotron
SW	Standing wave
TE-Mode	Transverse Electric Mode
TM-Mode	Transverse Magnetic Mode
TEM-Mode	Transverse Electromagnetic Mode
TW	Travelling wave
VF	Vacuum Flange
VNA	Vector Network Analyzer

1. INTRODUCTION

Particle accelerators can be divided into two fundamental types according to their power sources: electrostatic accelerators and electromagnetic/electrodynamic accelerators. The Cockcroft-Walton and the Van de Graaff accelerators are examples of electrostatic type. In this kind, electrostatic field, constant in time, is used for acceleration; therefore the accelerating voltage determines the maximum accessible energy. However, these accelerators are not feasible for modern experiments due to the limitations originating from electrical breakdowns. The second kind of accelerators, which are also known as resonant accelerators rely on electromagnetic fields that change over time periodically. In other words, an oscillating radio frequency (RF) field is used. (The large electric fields stored in the resonant cavities lead to the first limitation encountered with RF accelerators, known as RF-breakdown.)

The first RF accelerator, LINear ACcelerator (linac) proposed by Rolf Widerøe in 1927. In linacs, alternating current (AC) voltage and a series of drift tubes are used. The particles experience peaks of the AC voltage waves and movement occurs. As expected while the electric fields in the direction of the current increase the energy of the particles, negative electric fields apply a decelerating influence (for positive charged particles). In order to prevent this reverse impact, drift tubes are used to shield the particles. These drift tubes behave as antennae at high frequencies because of their metallic composition. In addition, they need to be built longer at each step of the acceleration in order to keep particles synchronized with the RF as they traverse the tubes faster. These two consequences bring some limitations to Widerøe type linacs [1].

In 1948, a more effective linac type was developed by Alvarez (Figure 1.2). The drift tubes in the new linac structure were put in a large metallic cylindrical tank to prevent radiating power generated by the drift tubes which would act as antennae. The drift tubes are placed at some distance, $d = \beta\lambda$, (where β is the relative speeds of particle and light) from each other. When the applied field is in its decelerating phase,

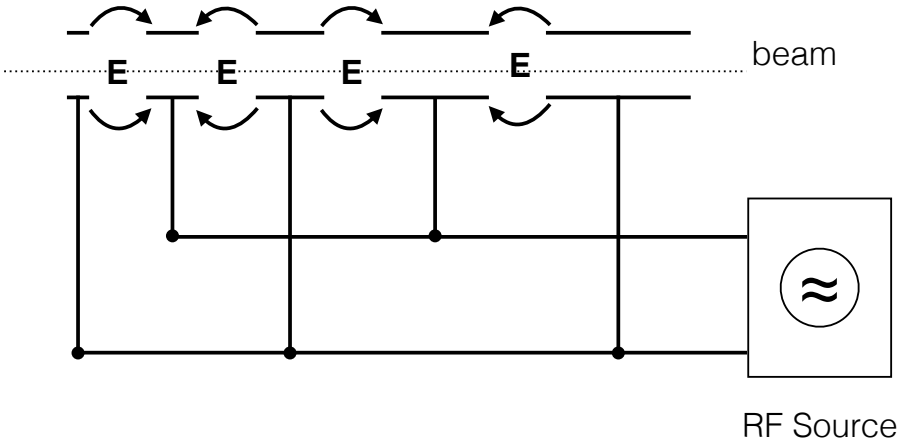

Figure 1.1. Widerøe Linac [1]

the particles are shielded inside the drift tubes.

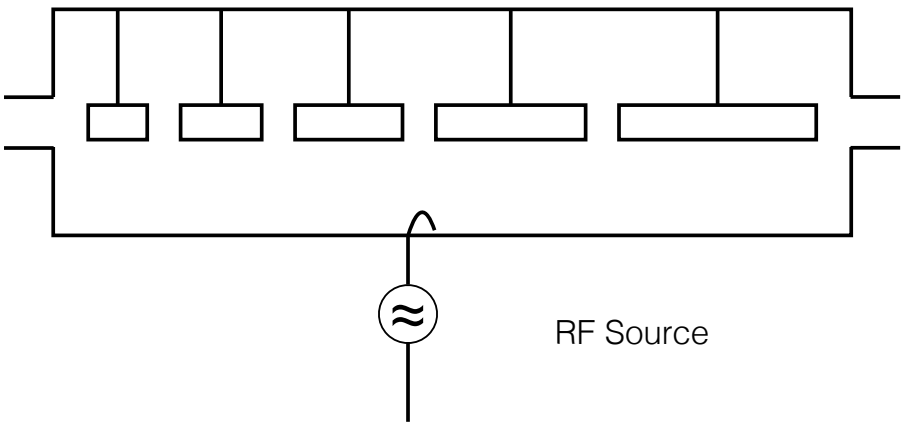

Figure 1.2. Alvarez Linac [1]

In this regard, RF waves are significant for accelerators. RF waves can be used to transmit power or signal. In fact, these two concepts; power and signal transmissions are basically same mathematically but their real-life implementations vary. This thesis will focus mostly on signal transmission and a brief discussion of power transmission will be presented in the sixth chapter.

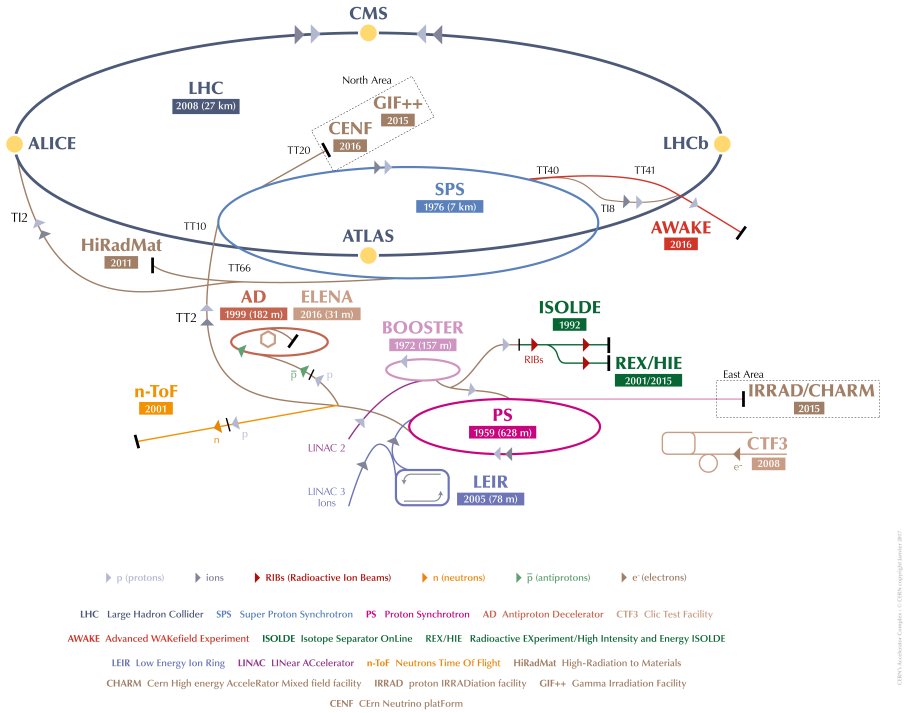

Figure 1.3. The CERN Accelerator Complex [2]

1.1. CERN

The Large Hadron Collider (LHC) at CERN being the largest circular collider in the world, is fed by two counter rotating proton or ion beams. The LHC injector chain mainly consists of Linac2 for proton and Linac3 for ions, then the Proton Synchrotron Booster (PSB), the Proton Synchrotron (PS), and the Super Proton Synchrotron (SPS) as illustrated in Figure 1.3. As a brief review of the injector chain, the proton particle beams start to accelerate in Linac2 or in Linac3 and follow to a four-vane radio frequency quadrupole (RFQ) with the 750 keV extraction energy. Then, the three tank drift tube linac (DTL) comes after the RFQ with focusing quadrupoles in the drift tubes. An 80 m long transfer line carries 50 MeV beams to the PSB. In the PSB, 4 rings having quarter length of the circumference of the PS stand top of each other. PSB allows to extract sequentially each beam to the PS. The beams circulating inside the PS can be accelerated up to 14 GeV for the SPS physics or up to 26 GeV for the

LHC physics. The beams injected to the SPS accelerated up to 450 GeV final energy before entering the LHC ring. In addition to these accelerators and energy information, it is worth noting that the circumferences ratio of the PS to SPS is 1/11 and that of the SPS to LHC is 7/27 [7].

Long Shutdown (LS) periods are needed to maintain and upgrade the LHC machine. Regular upgrades are needed not only because of various limitations in the LHC and the other accelerators, but also to increase the luminosity for future. According to the scenario described in the High Luminosity-LHC (HL−LHC) project, an upgrade and modification of the SPS is compulsory [8,9]. When the present beam measurements and the longitudinal impedance model at the SPS are taken into account, the various contributors to beam instabilities are identified to come from the accelerating and Landau cavities, the extraction kickers, the vacuum flanges, the Beam Position Monitors (BPM), the pumping ports, the so-called Y-chambers, the beam scrapers, resistive wall and space charge impedance at low energy, as shown in Figure 1.4 [3, 10–12].

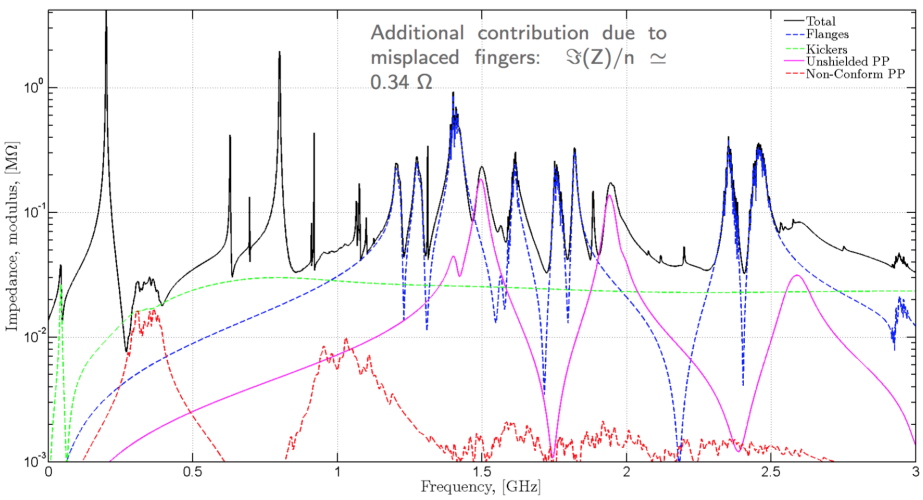

Figure 1.4. Current Longitudinal Impedance Model at SPS [3].

The dominant suspects of beam instabilities, causing to growth of beam or loss of intensity, can be cited as the accelerating cavities, the extraction kickers and the vacuum flanges, especially one specific type of the vacuum flange located at the horizontal BPM (BPH) and the focusing quadrupole (QF) magnet (BPH–QF) junction [10–12].

These vacuum flanges are found to have been responsible for single and multi-bunch longitudinal instabilities. Therefore, several impedance reduction campaigns for vacuum flanges have been performed since 2000. However, the status of these shields have never been checked up to now. For this reason, a task was foreseen by CERN, inclusive of the LIU project to find a method for identifying those situations without dismounting the shield locations of the SPS machine. The chapters three, four and five examine the effects of the vacuum flanges located at BPH-QF junctions at SPS and shows the results of the presence of the implemented shields.

In the second chapter, the RF related concepts and theories will be reviewed. These reviews are needed to understand the comparison of the simulations and the measurements to come.

In the third chapter, simulation results will be shown.

In chapters four and five, the measurement technique will be discussed and measurement results will be shown.

In the sixth chapter, there will be explained an ongoing project to transmit low power at the transmission line of the project. The project is namely 'Design, Simulation and Production of an RF Circulator and Transmission Line' at the KAHVE Laboratory of Boğaziçi University will be mentioned. There are three goals in this project. The first one is the design of an RF circulator and the RF transmission line connecting to the circulator for high-power and high frequency (UHF) implementations. The second aim is to model and to perform the computer simulations of the designed components. The final goal is to produce, to test and to develop all of these designed elements in Turkey.

In the final chapter, various outcomes from both projects will be summarized and a discussion for future work will be delivered.

2. THEORY

The electromagnetic (EM) theory of waves in waveguides will be the first topic in this chapter. It will help to understand how a wave can behave in a medium within specific boundary conditions and what kind of EM-configurations can be observed. The frequency modes can be easily determined with the EM theory. The first case will be rectangular shape waveguides. This concept will be important for the ongoing project at KAHVE Lab on the design of an 800 MHz circulator and RF transmission line in which the particular operating frequency is selected at 800 MHz. The mode concept will be significant for this aim. The circular waveguides will be studied for the research at CERN.

As described by Zotter [13], the interaction of the charged particles can be described by impedances in the frequency domain, or equivalently by wakefields in the time domain. Impedances and wakes for a complete accelerator have complicated or nearly impossible calculation. For this reason, the calculation is done by separating the complete accelerator into elements and then contribution from each element is added individually. Calculating numerically is simpler in the frequency domain in which coupling impedance calculation, taken the Fourier transforms of the wake functions is easier. Therefore, these two main concepts will also be mentioned in detail in this chapter. The last section of the chapter will be about the scattering parameters.

2.1. EM Waves and TE-TEM-TM Modes

Differential forms of Maxwell's equations [14, 15]:

$$\begin{array}{lrcl} \text{Gauss's Law} & \vec{\nabla}\cdot\vec{E} & = & \mu_0 c^2\rho \quad , \\ \text{Gauss's Law for Magnetism} & \vec{\nabla}\cdot\vec{B} & = & 0 \quad , \\ \text{Maxwell-Faraday Equation} & \vec{\nabla}\times\vec{E}+\frac{\partial}{\partial t}\vec{B} & = & 0 \quad , \\ \text{Ampere's Law} & \vec{\nabla}\times\vec{B}-\frac{1}{c^2}\frac{\partial}{\partial t}\vec{E} & = & \mu_0\vec{J} \quad . \end{array} \tag{2.1}$$

where $\mu_0 = 4\pi \times 10^{-7}$ Henry/m is the permeability value of the free space and $\varepsilon_0 = 1/\mu_0 c^2 = 8.854 \times 10^{-12}$ Farad/m is the permittivity value of free space.

Assuming that current and charge are zero, differential forms of Maxwell's equations can be turned into:

$$\begin{aligned} \vec{\nabla} \cdot \vec{E} &= 0 \quad , \\ \vec{\nabla} \cdot \vec{B} &= 0 \quad , \\ \vec{\nabla} \times \vec{E} + \frac{\partial}{\partial t}\vec{B} &= 0 \quad , \\ \vec{\nabla} \times \vec{B} - \frac{1}{c^2}\frac{\partial}{\partial t}\vec{E} &= 0 \quad . \end{aligned} \tag{2.2}$$

Using the triple vector identity $\vec{\nabla} \times \vec{\nabla} \times \vec{A} = \vec{\nabla}(\vec{\nabla} \cdot \vec{A}) - (\vec{\nabla} \cdot \vec{\nabla})\vec{A}$, the wave equation of the electric field can be obtained with following steps:

$$\begin{aligned} \vec{\nabla} \times \vec{E} + \frac{\partial}{\partial t}\vec{B} &= 0 \quad , \\ \vec{\nabla} \times \Big(\vec{\nabla} \times \vec{E}\Big) + \frac{\partial}{\partial t}\vec{\nabla} \times \vec{B} &= 0 \quad , \\ \vec{\nabla}\Big(\vec{\nabla} \cdot \vec{E}\Big) - \Big(\vec{\nabla} \cdot \vec{\nabla}\Big)\vec{E} + \frac{1}{c^2}\frac{\partial^2 \vec{E}}{\partial t^2} &= 0 \quad . \end{aligned} \tag{2.3}$$

The gradient of the electric field is zero in source-free region which is $\vec{\nabla} \cdot \vec{E} = 0$. By using this result, Equation 2.3 becomes:

$$\begin{aligned} -\vec{\nabla} \cdot \vec{\nabla}\vec{E} + \frac{1}{c^2}\frac{\partial^2 \vec{E}}{\partial t^2} &= 0 \quad , \\ \nabla^2 \vec{E} - \frac{1}{c^2}\frac{\partial^2 \vec{E}}{\partial t^2} &= 0 \quad , \end{aligned} \tag{2.4}$$

where $\nabla^2 = \frac{\partial^2}{\partial x^2} + \frac{\partial^2}{\partial y^2} + \frac{\partial^2}{\partial z^2}$ is the Laplace operator in Cartesian coordinates. In a similar way, the wave equation of magnetic induction can be written as:

$$\nabla^2 \vec{B} - \frac{1}{c^2}\frac{\partial^2 \vec{B}}{\partial t^2} = 0 \quad . \tag{2.5}$$

These equations are valid in the vacuum. If they are in a medium, they become

$$\nabla^2\vec{E} - \frac{1}{v^2}\frac{\partial^2\vec{E}}{\partial t^2} = 0 \quad , \tag{2.6}$$

$$\nabla^2\vec{B} - \frac{1}{v^2}\frac{\partial^2\vec{B}}{\partial t^2} = 0 \quad , \tag{2.7}$$

where $v = \frac{c}{\sqrt{\frac{\varepsilon\mu}{\varepsilon_0\mu_0}}}$ is the speed of light in the medium and ε as well as μ are the permittivity and the permeability of the medium, respectively.

Assume that the electric field function can be written as:

$$\vec{E}(x,y,z,t) = \vec{E}(x,y,z)e^{j\omega t} \quad . \tag{2.8}$$

By inserting this function in the wave equations, the Helmholtz equation can be obtained:

$$\begin{aligned}
\left(\nabla^2 - \frac{1}{c^2}\frac{\partial^2}{\partial t^2}\right)\vec{E}(x,y,z)e^{j\omega t} &= 0 \quad , \\
\nabla^2\vec{E}(x,y,z)e^{j\omega t} - \frac{(i\omega)^2}{c^2}\vec{E}(x,y,z)e^{j\omega t} &= 0 \quad , \\
\nabla^2\vec{E}(x,y,z) + \frac{\omega^2}{c^2}\vec{E}(x,y,z) &= 0 \quad , \\
\nabla^2\vec{E}(x,y,z) + \beta^2\vec{E}(x,y,z) &= 0 \quad ,
\end{aligned} \tag{2.9}$$

where $\beta = \omega/c = \omega\sqrt{\varepsilon\mu}$ is the wave number and ω is the angular frequency.

These derived Helmholtz equations in 3D are important because they have separable solutions for each 1-dimension. To obtain these three solutions is more trivial than to get one general 3D solution. Each separated dimension has a solution for one specific general solution. After the product of the solutions for each dimension, the general solution can be obtained by summing these combined solutions. For this reason, the separated equations will be used in upcoming sections.

2.1.1. Rectangular Cross-section Waveguides

Consider that a waveguide has an infinite length and is filled with a material of permittivity μ as well as permeability ε (as shown in Figure 2.1). The aim is to find out possible configurations/modes inside the guide. The configurations of the fields can be described as transverse electric (TE), transverse magnetic (TM), and transverse electromagnetic (TEM). TEM field modes, which cannot be observed in a waveguide, will not be explained in this thesis because TEM configuration does not fulfil/satisfy the boundary conditions on the waveguide. Therefore, only TE and TM modes will be described below.

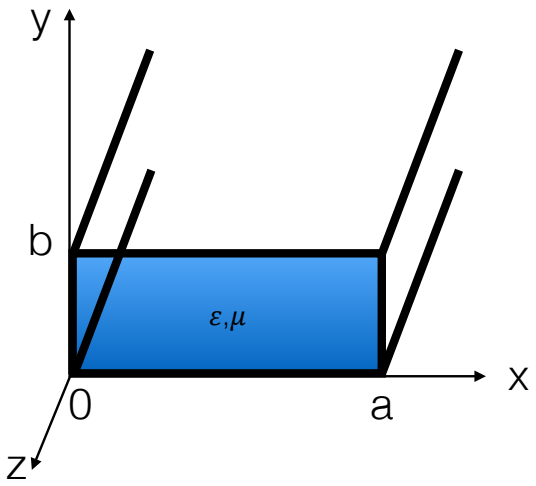

Figure 2.1. Rectangular waveguide (z axis is chosen to align with the direction of propagation of the wave)

2.1.1.1. TE Mode. TE mode refers to Transverse Electric field mode, which has zero electric field in the z-direction ($E_z = 0$). The following equations indicate how the electric and magnetic fields in TE mode can be expressed using the z-component of a

vector potential function, $\vec{A}_z(x,y,z)$ using Maxwell's equations:

$$\begin{aligned}
E_x &= -\frac{1}{\varepsilon}\frac{\partial A_z}{\partial y} \quad , \\
E_y &= \frac{1}{\varepsilon}\frac{\partial A_z}{\partial x} \quad , \\
E_z &= 0 \quad , \\
H_x &= -j\frac{1}{\omega\mu\varepsilon}\frac{\partial^2 A_z}{\partial x \partial z} \quad , \\
H_y &= -j\frac{1}{\omega\mu\varepsilon}\frac{\partial^2 A_z}{\partial y \partial z} \quad , \\
H_z &= -j\frac{1}{\omega\mu\varepsilon}\Big(\frac{\partial^2}{\partial z^2} + \beta^2\Big)A_z
\end{aligned} \tag{2.10}$$

where $\beta^2 = \frac{\omega^2}{c^2}$ and A_z satisfies the wave equation:

$$\vec{\nabla}^2 A_z(x,y,z) + \beta^2 A_z(x,y,z) = 0 \quad . \tag{2.11}$$

Using the separation of variables method, the solution of $A_z(x,y,z)$ can be given by:

$$A_z(x,y,z) = f(x)g(y)h(z) \quad . \tag{2.12}$$

Note that the functions in transverse directions ($x-y$ directions) can act as a standing wave due to the enclosed waveguide in the transverse directions as shown in Figure 2.1. Hence, the solutions of the functions, $f(x)$ and $g(y)$ can be chosen as:

$$f(x) = a_1\cos(\beta_x x) + b_1\sin(\beta_x x) \quad , \tag{2.13}$$

$$g(y) = a_2\cos(\beta_y y) + b_2\sin(\beta_y y) \quad . \tag{2.14}$$

Due to the infinite length of the guide, the fields in the longitudinal direction (z-direction) can be represented as travelling waves and the solution for $h(z)$ can be written as:

$$h(z) = a_3 e^{-j\beta_z z} + b_3 e^{j\beta_z z} \quad , \tag{2.15}$$

where the first term indicates the propagating waves in the $+z$-direction and the second one is travelling in the $-z$ direction. With this convention, for the rest of Chapter 2, we assume that the waves travel in $+z$-direction by taking $b_3 = 0$.

With the above assumptions, the potential function can be written as:

$$A_z(x,y,z) = \Big[a_1\cos(\beta_x x) + b_1\sin(\beta_x x)\Big] a_3 e^{-j\beta_z z}\Big[a_2\cos(\beta_y y) + b_2\sin(\beta_y y)\Big] \quad (2.16)$$

where $\beta_x^2 + \beta_y^2 + \beta_z^2 = \beta^2 = w^2\mu\epsilon = w^2/c^2$ and a_1, a_2, a_3, b_1, b_2, are arbitrary constants. The constants with β_x and β_y will be substituted by applying the boundary conditions as written below:

$$E_x(0 \le x \le a, y = 0, z) = E_x(0 \le x \le a, y = b, z) = 0 \quad , \quad (2.17)$$

$$E_y(x = 0, 0 \le y \le b, z) = E_y(x = a, 0 \le y \le b, z) = 0 \quad , \quad (2.18)$$

$$E_z(x = 0, 0 \le y \le b, z) = E_z(x = a, 0 \le y \le b, z) = 0 \quad , \quad (2.19)$$

$$E_z(0 \le x \le a, y = 0, z) = E_z(0 \le x \le a, y = b, z) = 0 \quad . \quad (2.20)$$

Since $E_z = 0$ in the TE modes, the boundary conditions written along the z-direction, E_z, are automatically satisfied. The electric field in the x-direction can be written after inserting Equation 2.10 with the boundary condition, $E_x(0 \le x \le a, y = 0, z) = 0$ as:

$$\begin{aligned}
E_x(x,y,z) &= -\frac{1}{\varepsilon}\frac{\partial A_z}{\partial y} \quad , \\
&= -\frac{\beta_y}{\varepsilon}\Big[a_1\cos(\beta_x x) + b_1\sin(\beta_x x)\Big] \\
&\times a_3 e^{-j\beta_z z}\Big[-a_2\sin(\beta_y y) + b_2\cos(\beta_y y)\Big] \quad , \\
E_x(0 \le x \le a, y = 0, z) &= -a_3\frac{\beta_y}{\varepsilon}\Big[a_1\cos(\beta_x x) + b_1\sin(\beta_x x)\Big] \\
&\times a_3 e^{-j\beta_z z}\Big[-a_2\sin(0) + b_2\cos(0)\Big] \quad , \\
&= -a_3\frac{\beta_y}{\varepsilon}a_3 e^{-j\beta_z z}\Big[a_1\cos(\beta_x x) + b_1\sin(\beta_x x)\Big]\Big[b_2\Big] \quad , \\
&= 0 \quad .
\end{aligned} \quad (2.21)$$

Equation 2.21 can be satisfied if $b_2 = 0$.

By inserting the other boundary condition, $E_x(0 \leq x \leq a, y = b, z) = 0$, $E_x(x, y, z)$ can be reduced to:

$$\begin{aligned} E_x(x, y, z) &= -a_3 \frac{\beta_y}{\varepsilon} \Big[a_1 \cos(\beta_x x) + b_1 \sin(\beta_x x) \Big] \Big[-a_2 \sin(\beta_y y) \Big] a_3 e^{-j\beta_z z}, \\ &= 0 \quad , \\ E_x(0 \leq x \leq a, y = b, z) &= -a_3 \frac{\beta_y}{\epsilon} \Big[a_1 \cos(\beta_x x) + b_1 \sin(\beta_x x) \Big] \Big[-a_2 \sin(\beta_y b) \Big] a_3 e^{-j\beta_z z}, \\ &= 0 \quad . \end{aligned} \tag{2.22}$$

The condition that satisfies Equation 2.22 is:

$$\begin{aligned} \sin(\beta_y b) = 0 \quad &\longrightarrow \quad \beta_y b = n\pi \quad , \\ &\longrightarrow \quad \beta_y = \frac{n\pi}{b} \end{aligned} \tag{2.23}$$

where n is an integer, $n = 0, 1, 2, 3, ...$ and β_y can be referred as an eigenvalue of an eigenfunction. Likewise, by enforcing the boundary conditions, $E_y(x = 0, 0 \leq y \leq b, z) = E_y(x = a, 0 \leq y \leq b, z) = 0$, β_x function, which is taken by $a_1 = 0$ can be given by:

$$\begin{aligned} \sin(\beta_x a) = 0 \quad &\longrightarrow \quad \beta_x a = m\pi \quad , \\ &\longrightarrow \quad \beta_x = \frac{m\pi}{a} \end{aligned} \tag{2.24}$$

where m is an integer, $m = 0, 1, 2, 3, ...$

As a result of all these steps, the potential function, $A_z(x, y, z)$ becomes:

$$A_z(x, y, z) = A_{mn} \cos(\beta_x x) \cos(\beta_y y) e^{-j\beta_z z} \tag{2.25}$$

where A_{mn} is the product of all constants; a_1, b_1 and a_3. The subscripts of m and n are used for describing the field TE_{mn} modes.

In brief, all components of TE_{mn} modes are given by:

$$\begin{aligned}
E_x &= A_{mn}\frac{\beta_y}{\varepsilon}\cos(\beta_x x)\sin(\beta_y y)e^{-j\beta_z z} \quad , \\
E_y &= -A_{mn}\frac{\beta_x}{\varepsilon}\sin(\beta_x x)\cos(\beta_y y)e^{-j\beta_z z} \quad , \\
E_z &= 0 \quad , \\
H_x &= A_{mn}\frac{\beta_x\beta_z}{\omega\mu\varepsilon}\sin(\beta_x x)\cos(\beta_y y)e^{-j\beta_z z} \quad , \\
H_y &= A_{mn}\frac{\beta_y\beta_z}{\omega\mu\varepsilon}\cos(\beta_x x)\sin(\beta_y y)e^{-j\beta_z z} \quad , \\
H_z &= -jA_{mn}\frac{\beta_c^2}{\omega\mu\varepsilon}\cos(\beta_x x)\cos(\beta_y y)e^{-j\beta_z z} \quad ,
\end{aligned} \tag{2.26}$$

where $\beta_c^2 \equiv \beta^2 - \beta_z^2 = \beta_x^2 + \beta_y^2 = (m\pi/a)^2 + (n\pi/b)^2$ and it is referred to as the *cutoff wave number*. The cutoff frequency, $f_{c,mn}$ for a given TE_{mn} mode can be obtained by using the cutoff wave number, β_c:

$$\begin{aligned}
\beta_c &= \frac{2\pi f_c}{c} = \sqrt{\left(\frac{m\pi}{a}\right)^2 + \left(\frac{n\pi}{b}\right)^2} \quad , \\
f_{c,mn} &= \frac{c}{2\pi}\sqrt{\left(\frac{m\pi}{a}\right)^2 + \left(\frac{n\pi}{b}\right)^2} \quad .
\end{aligned} \tag{2.27}$$

It is worth noting that the modes having the same cutoff frequency (with nonzero m and n values) are known as *degenerate* modes. In order to examine the effect of the cutoff frequency in detail, $\beta_{z,mn}$ can be expressed as:

$$\beta_{z,mn} = \begin{cases}
\beta\sqrt{1 - \left(\frac{f_{c,mn}}{f}\right)^2} & \text{for} \quad f > f_{c,mn} \quad , \\
0 & \text{for} \quad f = f_{c,mn} \quad , \\
-j\beta\sqrt{\left(\frac{f_{c,mn}}{f}\right)^2 - 1} & \text{for} \quad f > f_{c,mn} \quad .
\end{cases} \tag{2.28}$$

where $n, m \geq 0$ and $m \neq n = 0$ for TE mode. The conditions on $f_{c,mn}$ indicate whether the wave is propagating or not. $f > f_{c,mn}$ means that the wave propagates inside the structure. $f < f_{c,mn}$ is the evanescent wave condition. The standing wave mode is under $f = f_{c,mn}$ condition and this frequency is referred to as cutoff frequency. It is worth noting that the operational frequency should be chosen higher than the cutoff

frequency, $f_{c,mn}$, not to attenuate the fields.

Consider that the long side of the rectangular waveguide is a ($a > b$). The lowest cutoff frequency in TE mode is TE_{10} and it is usually referred to as the *dominant mode*. If, on the other hand $b > a$, then the dominant mode will be TE_{01}. The cutoff frequency of the dominant mode is written by:

$$f_{c,10} = \frac{c}{2\pi}\frac{\pi}{a} = \frac{c}{2a} \quad . \tag{2.29}$$

2.1.1.2. TM Mode. TM mode refers to transverse magnetic field mode. It has zero magnetic field in the z-direction ($H_z = 0$). Steps similar to these used for the TE modes can be used to derive the TM field functions. The TM field functions will also be obtained by using a vector potential function, $\vec{A} = \hat{n}A_z(x, y, z)$. The whole set of equations for electric and magnetic fields of TM modes are:

$$\begin{aligned}
E_x &= -j\frac{1}{\omega\mu\varepsilon}\frac{\partial^2 A_z}{\partial x \partial z} \quad , \\
E_y &= -j\frac{1}{\omega\mu\varepsilon}\frac{\partial^2 A_z}{\partial y \partial z} \quad , \\
E_z &= -j\frac{1}{\omega\mu\varepsilon}\Big(\frac{\partial^2}{\partial z^2} + \beta^2\Big)A_z \quad , \\
H_x &= \frac{1}{\mu}\frac{\partial A_z}{\partial y} \quad , \\
H_y &= -\frac{1}{\mu}\frac{\partial A_z}{\partial x} \quad , \\
H_z &= 0 \quad .
\end{aligned} \tag{2.30}$$

In order to satisfy the wave equation, the vector potential function, A_z, can be written as:

$$\begin{aligned}
A_z(x, y, z) = &\Big[a_1\cos(\beta_x x) + b_1\sin(\beta_x x)\Big] \\
&\times \Big[a_2\cos(\beta_y y) + b_2\sin(\beta_y y)\Big] \\
&\times \Big[a_3 e^{-j\beta_z z} + b_3 e^{j\beta_z z}\Big].
\end{aligned} \tag{2.31}$$

This can be reduced to:

$$A_z(x,y,z) = B_{mn}\sin(\beta_x x)\sin(\beta_y y)e^{-j\beta_z z} \tag{2.32}$$

where $\beta_x = \frac{m\pi}{a}$ and $\beta_y = \frac{n\pi}{b}$, m and n are both positive integers. Using the simplified vector potential function, the following set of equations can be obtained:

$$\begin{aligned}
E_x &= -B_{mn}\frac{\beta_x\beta_z}{\omega\mu\varepsilon}\cos(\beta_x x)\sin(\beta_y y)e^{-j\beta_z z} \quad , \\
E_y &= -B_{mn}\frac{\beta_y\beta_z}{\varepsilon}\sin(\beta_x x)\cos(\beta_y y)e^{-j\beta_z z} \quad , \\
E_z &= -jB_{mn}\frac{\beta_c^2}{\omega\mu\varepsilon}\sin(\beta_x x)\sin(\beta_y y)e^{-j\beta_z z} \quad , \\
H_x &= B_{mn}\frac{\beta_y}{\mu}\sin(\beta_x x)\cos(\beta_y y)e^{-j\beta_z z} \quad , \\
H_y &= -B_{mn}\frac{\beta_x}{\mu}\cos(\beta_x x)\sin(\beta_y y)e^{-j\beta_z z} \quad , \\
H_z &= 0 \quad .
\end{aligned} \tag{2.33}$$

where β_c is the cutoff wave number as defined before. Consequently, the cutoff wave number and the cutoff frequency can be written in the same way as in the TE mode as:

$$\begin{aligned}
\beta_c = \frac{2\pi f_c}{c} &= \sqrt{\left(\frac{m\pi}{a}\right)^2 + \left(\frac{n\pi}{b}\right)^2} \quad , \\
f_{c,mn} &= \frac{c}{2\pi}\sqrt{\left(\frac{m\pi}{a}\right)^2 + \left(\frac{n\pi}{b}\right)^2} \quad .
\end{aligned} \tag{2.34}$$

where $n, m \geq 1$ for TM mode.

The frequency for the dominant TM mode is equal to

$$\begin{aligned}
f_{c,11} &= \frac{c}{2\pi}\sqrt{\left(\frac{\pi}{a}\right)^2 + \left(\frac{\pi}{b}\right)^2} \quad , \\
&= \frac{c}{2}\sqrt{1 + \left(\frac{a}{b}\right)^2} \quad .
\end{aligned} \tag{2.35}$$

Comparing the formula for the dominant modes for each mode, TE and TM, the dominant TE mode can be seen to always be the dominant one because of being smaller than the dominant TM mode:

$$\begin{aligned} f_c^{TE} &< f_c^{TM} \quad , \\ \frac{c}{2a} &< \frac{c}{2a}\sqrt{1+\left(\frac{a}{b}\right)^2} \quad . \end{aligned} \tag{2.36}$$

2.1.2. Circular Cross-section Waveguides

Assume that there is a circular waveguide as shown in Figure 2.2. The structure is filled with the material of permittivity μ and permeability ε.

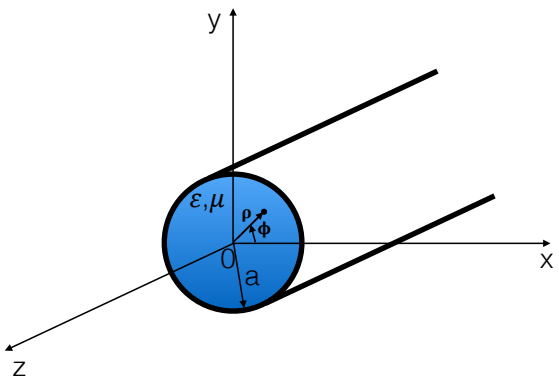

Figure 2.2. Cylindrical waveguide.

2.1.2.1. TE Mode. The vector potential in the z-direction, $A_z(\rho,\phi,z)$ should satisfy the wave equation:

$$\vec{\nabla}^2 A_z(\rho,\phi,z) + \beta^2 A_z(\rho,\phi,z) = 0 \tag{2.37}$$

where $\vec{\nabla}^2 = \frac{\partial^2}{\partial\rho^2} + \frac{q}{\rho}\frac{\partial}{\partial\rho} + \frac{1}{rho^2}\frac{\partial^2}{\partial\phi^2} + \frac{\partial^2}{\partial z^2}$ is Laplacian operator in cylindrical coordinates system. And the functions of electric and magnetic fields in the cylindrical coordinate

system can be given by:

$$
\begin{aligned}
E_\rho &= -\frac{1}{\mu\varepsilon}\frac{\partial A_z}{\partial \phi} \quad , \\
E_\phi &= \frac{1}{\varepsilon}\frac{\partial A_z}{\partial \rho} \quad , \\
E_z &= 0 \quad , \\
H_\rho &= -j\frac{1}{\omega\mu\varepsilon}\frac{\partial^2 A_z}{\partial \rho \partial z} \quad , \\
H_\phi &= -j\frac{1}{\omega\mu\varepsilon\rho}\frac{\partial^2 A_z}{\partial \phi \partial z} \quad , \\
H_z &= -j\frac{1}{\omega\mu\varepsilon}\Big(\frac{\partial^2}{\partial z^2} + \beta^2\Big)A_z \quad .
\end{aligned}
\tag{2.38}
$$

The solution for the wave equation, above, is written likewise done in the rectangular waveguides as:

$$
\begin{aligned}
A_z(\rho,\phi,z) = &\Big[a_1 J_m(\beta_\rho \rho) + b_1 N_m(\beta_\rho \rho)\Big] \\
&\times \Big[a_2 \cos(m\phi) + b_2 \sin(m\phi)\Big] \\
&\times \Big[a_3 e^{-j\beta_z z} + b_3 e^{j\beta_z z}\Big]
\end{aligned}
\tag{2.39}
$$

where $J_m(x)$ are the Bessel functions of the first kind, $N_m(x)$ are the Bessel functions of the second kind or Neumann functions, $\beta^2 = \beta_\rho^2 + \beta_z^2$ and a_1, a_2, a_3, b_1, b_2 and b_3 are arbitrary constants. The constants with β_ρ and β_z can be determined by applying the boundary conditions as:

$$E_\phi(\rho = a, \phi, z) = 0 \quad , \tag{2.40}$$

$$\text{Fields must be finite everywhere} \quad , \tag{2.41}$$

$$\text{Fields must repeat every } 2\pi \text{ radians in } \phi \quad . \tag{2.42}$$

Requiring finite fields everywhere, and noting that $N_m(\rho = 0) = \infty$, b_1 has to be 0 and due to the periodicity, the integer number of m is equal to $m = 0, 1, 2, 3, ...$ Hence, The z component of the electric vector potential for a wave propagating in the $+z$-direction

can be reduced to:

$$A_z(\rho,\phi,z) = A_{mn}J_m(\beta_\rho\rho)\Big[a_2\cos(m\phi)+b_2\sin(m\phi)\Big]e^{-j\beta_z z}. \tag{2.43}$$

By using Equation 2.38, the ϕ component of the electric field can be written as:

$$\begin{aligned} E_\phi &= \frac{1}{\varepsilon}\frac{\partial A_z}{\partial\rho} \quad , \\ &= \beta_\rho\frac{A_{mn}}{\varepsilon}J'_m(\beta_\rho\rho)\Big[a_2\cos(m\phi)+b_2\sin(m\phi)\Big]e^{-j\beta_z z} \quad . \end{aligned} \tag{2.44}$$

where $'$ denotes $\frac{\partial}{\partial(\beta_\rho\rho)}$. When the boundary condition, $E_\phi(\rho=a,\phi,z)=0$ is applied to E_ϕ:

$$E_\phi(\rho=a,\phi,z) = \beta_\rho\frac{A_{mn}}{\varepsilon}J'_m(\beta_\rho a)\Big[a_2\cos(m\phi)+b_2\sin(m\phi)\Big]e^{-j\beta_z z}=0 \quad . \tag{2.45}$$

The above equation can be satisfied by providing the following equation:

$$J'_m(\beta_\rho a)=0 \longrightarrow \beta_\rho a=\chi'_{mn} \longrightarrow \beta_\rho=\frac{\chi'_{mn}}{a} \quad , \tag{2.46}$$

where χ'_{mn} describes as the nth zero of the derivative of the Bessel function J_m of the first kind of order m and their values are listed in Table 2.1.

Table 2.1. Zeroes χ'_{mn} of the derivative $J'_m(\chi'_{mn})$ of the Bessel function of first kind, $J_m(x)$.

$J'_m(\chi'_{mn})=0$	$m=0$	$m=1$	$m=2$
$n=1$	3.8318	1.8412	3.0542
$n=2$	7.0156	5.3314	6.7061
$n=3$	10.1735	8.5363	9.9695

By using β_ρ, $\beta_{z,mn}$ equality can be given by:

$$\beta_{z,mn} = \begin{cases} \sqrt{\beta^2 - \beta_\rho^2} = \sqrt{\beta^2 - \left(\frac{\chi'_{mn}}{a}\right)^2} & \text{for} \quad \beta > \beta_\rho \quad , \\ 0 & \text{for} \quad \beta = \beta_c = \beta_\rho \quad , \\ -j\sqrt{\left(\frac{\chi'_{mn}}{a}\right)^2 - \beta^2} & \text{for} \quad \beta < \beta_\rho \quad . \end{cases} \tag{2.47}$$

The cutoff wave number must be equal to zero, $\beta_{z,mn} = 0$ to obtain the cutoff frequency as:

$$\begin{aligned} \beta_c = \frac{2\pi f_c}{c} = \beta_\rho = \frac{\chi'_{mn}}{a} \quad , \\ f_{c,mn} = \frac{\chi'_{mn} c}{2\pi a} \quad . \end{aligned} \tag{2.48}$$

The whole set of electric and magnetic field components are summarized below:

$$\begin{aligned} E_\rho &= -\frac{1}{\rho\varepsilon}\frac{\partial A_z}{\partial \phi} \\ &= -A_{mn}\frac{m}{\varepsilon\rho}J_m(\beta_\rho\rho)\Big[-a_2\sin(m\phi) + b_2\cos(m\phi)\Big]e^{-j\beta_z z} \quad , \\ E_\phi &= \frac{1}{\varepsilon}\frac{\partial A_z}{\partial \rho} \\ &= A_{mn}\frac{\beta_\rho}{\varepsilon}J'_m(\beta_\rho\rho)\Big[a_2\cos(m\phi) + b_2\sin(m\phi)\Big]e^{-j\beta_z z} \quad , \\ E_z &= 0 \quad , \\ H_\rho &= -j\frac{1}{\omega\mu\varepsilon}\frac{\partial^2 A_z}{\partial\rho\partial z} \\ &= -A_{mn}\frac{\beta_\rho\beta_\phi}{\omega\mu\varepsilon}J'_m(\beta_\rho\rho)\Big[a_2\cos(m\phi) + b_2\sin(m\phi)\Big]e^{-j\beta_z z} \quad , \\ H_\phi &= -j\frac{1}{\omega\mu\varepsilon\rho}\frac{\partial^2 A_z}{\partial\phi\partial z} \\ &= -A_{mn}\frac{m\beta_z}{\omega\mu\varepsilon\rho}J_m(\beta_\rho\rho)\Big[-a_2\sin(m\phi) + b_2\cos(m\phi)\Big]e^{-j\beta_z z}, \\ H_z &= -j\frac{1}{\omega\mu\varepsilon}\Big(\frac{\partial^2}{\partial z^2} + \beta^2\Big)A_z \\ &= -jA_{mn}\frac{m\beta_\rho^2}{\omega\mu\varepsilon}J_m(\beta_\rho\rho)\Big[a_2\cos(m\phi) + b_2\sin(m\phi)\Big]e^{-j\beta_z z} \quad . \end{aligned} \tag{2.49}$$

2.1.2.2. TM Mode. The transverse modes can be derived by using similar steps to those performed in the TE modes. When the vector potential function, $A_z(\rho,\phi,z)$ is inserted into the wave equation, it should satisfy the wave equation and its solution, that is derived in a similar manner can be written as:

$$\begin{aligned} A_z(\rho,\phi,z) = &\Big[a_1 J_m(\beta_\rho \rho) + b_1 N_m(\beta_\rho \rho)\Big] \\ &\times \Big[a_2 \cos(m\phi) + b_2 \sin(m\phi)\Big] \\ &\times \Big[a_3 e^{-j\beta_z z} + b_3 e^{j\beta_z z}\Big] \end{aligned} \tag{2.50}$$

where a_1, a_2, a_3, b_1, b_2 and b_3 are arbitrary constants. The constants with β_ρ and β_z can be substituted by applying the boundary conditions as:

$$E_\phi(\rho = a,\phi,z) = 0 \qquad \text{or} \qquad E_z(\rho = a,\phi,z) = 0 \quad , \tag{2.51}$$

$$\text{Fields must be finite everywhere} \quad , \tag{2.52}$$

$$\text{Fields must repeat every } 2\pi \text{ radians in } \phi \quad . \tag{2.53}$$

As in the same behaviour with previous steps followed for the TE mode, the z component of the electric field can be written by applying the boundary conditions to the solution of the vector potential function, $A_z(\rho,\phi,z)$ as:

$$A_z(\rho,\phi,z) = B_{mn} J_m(\beta_\rho \rho)\Big[a_2 \cos(m\phi) + b_2 \sin(m\phi)\Big] e^{-j\beta_z z} \quad , \tag{2.54}$$

$$\begin{aligned} E_z &= -j\frac{1}{q\mu\varepsilon}\Big(\frac{\partial^2}{\partial z^2} + \beta^2\Big) A_z \quad , \\ &= -jB_{mn}\frac{\beta_\rho^2}{q\mu\varepsilon} J_m(\beta_\rho \rho)\Big[a_2 \cos(m\phi) + b_2 \sin(m\phi)\Big] e^{-j\beta_z z} \quad . \end{aligned} \tag{2.55}$$

The electric field in z-direction can be reduced by applying the boundary condition, $E_z(\rho = a,\phi,z) = 0$ to:

$$E_z(\rho = a,\phi,z) = -jB_{mn}\frac{\beta_\rho^2}{q\mu\varepsilon} J_m(\beta_\rho a)\Big[a_2 \cos(m\phi) + b_2 \sin(m\phi)\Big] e^{-j\beta_z z} = 0 \quad , \tag{2.56}$$

which can be true if the Bessel function of first kind is equal to zero:

$$J_m(\beta_\rho a) = 0 \longrightarrow \beta_\rho a = \chi_{mn} \longrightarrow \beta_\rho = \frac{\chi_{mn}}{a} \tag{2.57}$$

where χ_{mn} denotes the nth zero of the Bessel function J_m of the first kind of order m and their values are listed in Table 2.2. By using β_ρ equality, $\beta_{z,mn}$ can be given by:

Table 2.2. Zeroes χ_{mn} of derivative $J_m(\chi_{mn})$ of the Bessel function of first kind, $J_m(x)$ [5].

$J_m(\chi_{mn}) = 0$	$m = 0$	$m = 1$	$m = 2$
$n = 1$	2.4048	3.8317	5.1356
$n = 2$	5.5201	7.0156	8.4172
$n = 3$	8.6537	10.1735	11.6198

$$\beta_{z,mn} = \begin{cases} \sqrt{\beta^2 - \left(\frac{\chi_{mn}}{a}\right)^2} & \text{for} \quad \beta > \beta_\rho \quad , \\ 0 & \text{for} \quad \beta = \beta_c = \beta_\rho \quad , \\ -j\sqrt{\left(\frac{\chi_{mn}}{a}\right)^2 - \beta^2} & \text{for} \quad \beta < \beta_\rho \quad . \end{cases} \tag{2.58}$$

The cutoff wave number must be equal to zero, $\beta_{z,mn} = 0$ to provide for the cutoff frequency:

$$\begin{aligned} \beta_c = \frac{2\pi f_c}{c} = \beta_\rho = \frac{\chi_{mn}}{a} \quad , \\ f_{c,mn} = \frac{\chi_{mn} c}{2\pi a} \quad . \end{aligned} \tag{2.59}$$

The full set of electric and magnetic field components are summarized below:

$$
\begin{aligned}
E_\rho &= \frac{-j}{\omega\mu\varepsilon}\frac{\partial^2 A_z}{\partial\rho\partial z} = -B_{mn}\frac{\beta_\rho\beta_z}{\omega\mu\varepsilon}J'_m(\beta_{rho}\rho)\Big[a_2\cos(m\phi)+b_2\sin(m\phi)\Big]e^{-j\beta_z z} \quad , \\
E_\phi &= \frac{-j}{\omega\mu\varepsilon\rho}\frac{\partial^2 A_z}{\partial\phi\partial z} = -B_{mn}\frac{m\beta_z}{\omega\mu\varepsilon\rho}J_m(\beta_{rho}\rho)\Big[-a_2\sin(m\phi)+b_2\cos(m\phi)\Big]e^{-j\beta_z z} \quad , \\
E_z &= \frac{-j}{\omega\mu\varepsilon}\Big(\frac{\partial^2}{\partial z^2}+\beta^2\Big)A_z = -jB_{mn}\frac{\beta_\rho^2}{\omega\mu\varepsilon}J_m(\beta_{rho}\rho)\Big[a_2\cos(m\phi)+b_2\sin(m\phi)\Big]e^{-j\beta_z z} \quad , \\
H_\rho &= \frac{1}{\mu\rho}\frac{\partial A_z}{\partial\phi} = B_{mn}\frac{m}{\mu\rho}J_m(\beta_{rho}\rho)\Big[-a_2\sin(m\phi)+b_2\cos(m\phi)\Big]e^{-j\beta_z z} \quad , \\
H_\phi &= \frac{-1}{\mu}\frac{\partial A_z}{\partial\rho} = -B_{mn}\frac{\beta_\rho}{\mu}J'_m(\beta_{rho}\rho)\Big[a_2\cos(m\phi)+b_2\sin(m\phi)\Big]e^{-j\beta_z z} \quad , \\
H_z &= 0 \quad .
\end{aligned}
\tag{2.60}
$$

2.2. Wakefields and Impedances

Wakefields are one of the most substantial concepts when considering the performance of an accelerator. A beam passing near a discontinuity or a surface of finite resistance excites EM-fields which are called "wakefields". These excited fields affect the following bunches and cause several well-known consequences such as beam instabilities.

Consider a charged particle q which is called 'drive charge' moves in z-direction with β velocity in free space (as shown in the Figure 2.3). In the limit of $\beta \approx 1$, no field can exist behind or ahead of the moving drive charge in free space due to the causality. The causality theorem states that nothing can move faster than the speed of light in vacuum. Assume that a test charge has a specific distance to the drive charge and has the same velocity as the drive charge. The test charge will not be affected by the EM-fields generated due to the drive charge because of causality.

Now consider both particles traversing along an axis inside of a perfectly conducting pipe of circular cross-section (as shown in Figure 2.4). The EM-fields due to the drive charge cause an induced charge on the walls of the metallic structure and

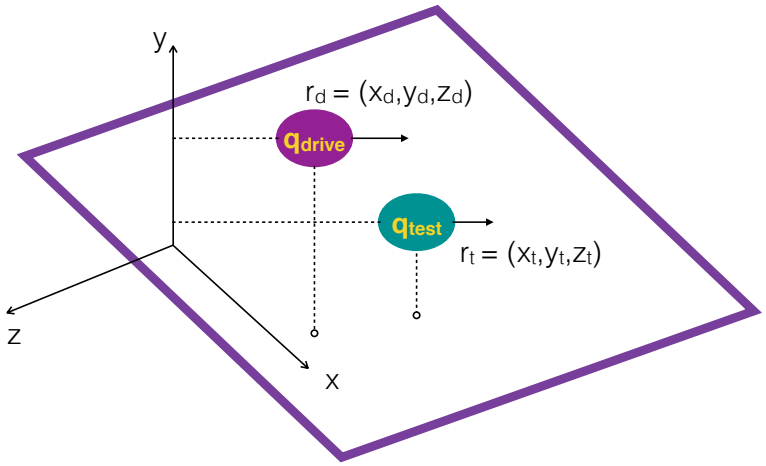

Figure 2.3. Schematic of the test and drive charge in the reference plane.

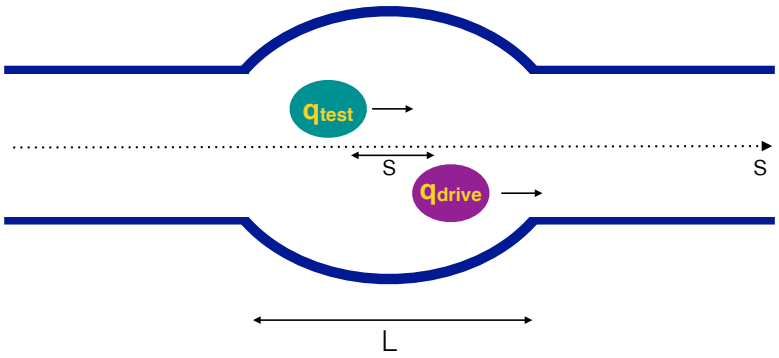

Figure 2.4. Schematic of the relative displacement of the drive and test particles

these image charges move with the same speed as the drive charge. Although the test charge feels the tail of an induced field generated by the image charges, it does not feel/experience the peak of the field. Hence, the effect of the tail of the field can be negligible. Nevertheless, if the perfectly conducting beam pipe is replaced with a

finite conducting material, the image charge falls behind the drive charge due to the resistance of the beam pipe. The lagged particle excites EM-fields and the fields affect the following particle(s) or bunch(es). A similar situation also applies to discontinuous structures such as the walls of the vacuum chamber, collimator, cavities, bellows etc. can be thought. These discontinuities cause resonating EM-fields induced by the drive particle. Generated wakefields may result in disturbing the test charge.

Wakefields are complex functions depending on cavity structures. To simplify their physics, the analysis of the wakefields can be separated into a summation of wake potentials in time domain. Calculation of the wake potentials is easier than the wakefields themselves. In the following section, the derivation of the wake potentials will be shown.

The wakefields can broadly be categorized into two: short range wakes and long range wakes. The short range wakes can be described as acting over several bunch lengths and the head-tail instability is an example of the consequences of this type. Contrary to the short type, the long range wakes affect over many consecutive bunch lengths. It is worth noting that wake function and impedance are two definitions of the same physical phenomenon which is related to the beam and its surroundings. The description in time domain is wake function and impedance is the frequency domain one. They can be converted to each other by using Fourier or inverse Fourier transforms. Impedance is more useful than wake function because the results are given at particular frequencies according to the modes of the cavities.

2.2.1. Wakefield

In this section, wakefields will be explained with starting Lorentz force [16–19]. As shown in the Figure 2.4, the drive and the test charge are assumed to be in a reference plane. The drive charge is moving in space and generates the EM-fields. The relative distance is $\vec{R} = \vec{r_t} - \vec{r_d}$, where $\vec{r_d}$ ($\vec{r_t}$) is the position of the drive (test) charge. The test charge feels the Lorentz force due to the $\vec{E}$-field produced by the driven charge

and the Lorentz force can be written as:

$$\vec{F}(\vec{r_d},\vec{r_t}) \quad = \quad q_t(\vec{E}+\vec{\nu}\times\vec{B}) \tag{2.61}$$

where E-field can be divided into transverse $\vec{E_\perp}$ as well as longitudinal $\vec{E_\parallel}$ components and the force can be also rewritten as these two separated components;

$$\vec{F_\parallel}(\vec{r_d},\vec{r_t}) \quad = \quad q_t\vec{E_\parallel} \quad , \tag{2.62}$$

$$\vec{F_\perp}(\vec{r_d},\vec{r_t}) \quad = \quad q_t(\vec{E_\perp}+\vec{\nu}\times\vec{B}) \tag{2.63}$$

where the transverse component is $\vec{E_\perp} = E_x\hat{x} + E_y\hat{y}$ (as in Equation 2.63), the longitudinal component is $\vec{E_\parallel} = E_z\hat{z}$ and the transverse magnetic component is $B_\parallel = 0$ in the $\hat{z}$-direction.

2.2.1.1. Longitudinal Wake Function and Wakefields of a Bunch. Considering the longitudinal component of the Lorentz force (Equation 2.62), the total energy change of the drive particle can be written by integrating over all space;

$$U_d(\vec{r_d}) \quad = \quad -\int_{-\infty}^{\infty} d\vec{z}\cdot\vec{F}(\vec{r_d}) \tag{2.64}$$

where the force for the drive charge is $\vec{F}(\vec{r_d}) = q_d\vec{E}(\vec{r_d})$. Similarly to this, the energy change due to the drive charge can be calculated for the test particle:

$$U_d(\vec{r_d},\vec{r_t},\vec{\tau}) \quad = \quad -\int_{-\infty}^{\infty} d\vec{z}\cdot\vec{F}(\vec{r_d},\vec{r_t}) \tag{2.65}$$

where the force for the test charge is $\vec{F}(\vec{r_d},\vec{r_t}) = q_t\vec{E}(\vec{r_d},\vec{r_t})$ and the time delay between the two particles is $\tau = \frac{z_d - z_t}{\beta c}$.

When these energy changes are normalized (in the equations 2.64, 2.65), the energy loss for the drive charge can be called the loss factor and for the test charge it can be named longitudinal wake function. The energy losses can be written as below;

$$\begin{array}{lrcl} \text{The Loss Factor} & k_{loss}(\vec{r_d}) & = & \frac{U_d(\vec{r_d})}{q_d^2} \quad , \\ \text{The Longitudinal Wake Function} & w_{\parallel}(\vec{r_d},\vec{r_t},\tau) & = & \frac{U_t(\vec{r_d},\vec{r_t},\tau)}{q_d q_t} \quad . \end{array} \tag{2.66}$$

For an accelerator, the calculations are considered for a bunch of particles instead of a single one. Hence, describing a wake function distribution is needed rather than Equation 2.66 which is defined for a single particle. In general the total charge of a bunch, q_d^{total} can be given by:

$$q_d^{total} = -\int_{-\infty}^{\infty} i_b(\tau) d\tau \tag{2.67}$$

where i_b is the current of the bunch.

In analogy to the calculation of the energy change for a single test particle, the wake function distribution of a bunch can be defined as an infinitesimal small bunch distribution at a specific time τ';

$$dU(\vec{r_t}, \tau - \tau') = q_t' i_b(\tau') \omega_{\parallel}(\vec{r_t}, \tau - \tau') \tag{2.68}$$

where q_t' is the infinitesimal small charge distribution for the bunch. By using Equation 2.66, longitudinal wake function for a bunch known as *wake potential* can be written as:

$$\mathrm{W}_{\parallel}(\vec{r_t}, \tau) = \frac{U(\vec{r_t}, \tau)}{q_d^{total}, q_t'} = \frac{1}{q_d^{total}} \int_{-\infty}^{\infty} i_b(\tau') \omega_{\parallel}(\vec{r_t}, \tau - \tau') d\tau' \quad . \tag{2.69}$$

2.2.1.2. Transverse Wake Function and Wakefields of a Bunch. Now, considering the change of the transverse momentum, it can be written as

$$\vec{p}(\vec{r_d}, \vec{r_t}, \tau) \;=\; \int_{-\infty}^{\infty} \vec{F}_{\perp}(\vec{r_d}, \vec{r_t}) \cdot d\vec{z} \quad . \tag{2.70}$$

And the normalization of the wake function with respect to the two particles can be described as:

$$\omega_{\perp}(\vec{r_d}, \vec{r_t}, \tau) \;=\; \frac{\vec{p}(\vec{r_d}, \vec{r_t}, \tau)}{q_d q_t} \quad . \tag{2.71}$$

Then, the infinitesimal small distribution of the the energy can be given by

$$dU(\vec{r_t}, \tau - \tau') \;=\; q_t' i_b(\tau') \omega_{\perp}(\vec{r_d}, \vec{r_t}, \tau) \quad . \tag{2.72}$$

By using this distribution, transverse wake function for a bunch will be equal to

$$\mathrm{W}_{\perp}(\vec{r_t}.\tau) \;=\; \frac{U(\vec{r_t}, \tau)}{q_d, q_t'} = \frac{1}{q_d} \int_{-\infty}^{\infty} i_b(\tau') \omega_{\perp}(\vec{r_t}, \tau - \tau') d\tau' \quad , \tag{2.73}$$

2.2.1.3. Panofsky - Wenzel Theorem. It is worth mentioning that there is a relation between longitudinal and transverse wake functions and it is known as the Panofsky-Wenzel theorem. This theorem shows that the transverse gradient of the longitudinal wake function is equal to the longitudinal gradient of the transverse wake function [20, 21]. In addition, it is applicable if the input and output beam pipes have the same cross-section.

For the derivation of the theorem, let us start with the Lorentz force acting on the test particle: $\vec{F} = q_t\{\vec{E} + \vec{v} \times \vec{B}\}$. The Lorentz force can be written in another form of the equation by inserting the Faraday's law in integral form $\vec{B} = -\int(\vec{\nabla} \times \vec{E})dt$;

$$\vec{F} \;=\; q_t \left[\vec{E} - \vec{v} \times \int (\vec{\nabla} \times \vec{E}) dt \right] \quad . \tag{2.74}$$

Assume that $\vec{v}$ is constant and by using the vector triple product identity $\vec{a} \times (\vec{b} \times \vec{c}) = \vec{b}(\vec{a} \cdot \vec{c}) - (\vec{a} \cdot \vec{b})\vec{c}$, the general Lorentz force can be rewritten as

$$\vec{F} = q_t \left[\vec{E} - \int \left(\vec{\vec{\nabla}}(\vec{v} \cdot \vec{E}) - \vec{E}(\vec{v} \cdot \vec{\vec{\nabla}}) \right) dt \right] \quad . \tag{2.75}$$

If the movement is in $\hat{z}$-direction, the equation can be reorganized as;

$$\vec{F} = q_t \left[\vec{E} - \int \left(\vec{\vec{\nabla}}(\vec{v} \cdot \vec{E}) - \vec{v}(\vec{\vec{\nabla}}\vec{E}) \right) dt \right] \quad , \tag{2.76}$$

and it can also be separated into longitudinal and transverse components;

$$\vec{F_\parallel} = q_t \vec{E_\parallel} = q_t \vec{E_z} \quad , \tag{2.77}$$

$$\vec{F_\perp} = q_t \left[\vec{E_\perp} - v \int \left(\vec{\nabla}_\perp E_z - \frac{\partial \vec{E_\perp}}{\partial z} \right) dt \right] \tag{2.78}$$

where $\vec{\nabla}_\perp = \frac{\partial}{\partial x} + \frac{\partial}{\partial y}$ is the differential operator in transverse plane. Moreover, by using these components of the Lorentz force, the wake functions of Equations 2.66, 2.71 derived in the Section 2.2.1 become:

$$\omega_\parallel(\vec{r_d}, \vec{r_t}, \tau) = -\frac{1}{q_d} \int dz E_z(\vec{r_d}, \vec{r_t}) \quad , \tag{2.79}$$

$$\omega_\perp(\vec{r_d}, \vec{r_t}, \tau) = -\frac{1}{q_d} \int dz \left[\vec{E_\perp}(\vec{r_d}, \vec{r_t}) - v \int \left(\vec{\nabla}_\perp E_z(\vec{r_d}, \vec{r_t}) - \frac{\partial E_\perp(\vec{r_d}, \vec{r_t})}{\partial z} \right) dt \right] \quad . \tag{2.80}$$

When the perpendicular wake potential function is differentiated by s, the below function can be obtained by using the relation of $s = vt - z \longrightarrow \frac{\partial}{\partial s} = -\frac{\partial}{\partial z}$ and $\frac{\partial}{\partial s} = \frac{1}{v}\frac{\partial}{\partial z}$:

$$\begin{aligned}
\frac{\partial}{\partial s}\omega_{\perp}(\vec{r_d},\vec{r_t},\tau) =& \frac{\partial}{\partial s}\Bigg(-\frac{1}{q_d}\int dz \Bigg[\vec{E_{\perp}}(\vec{r_d},\vec{r_t}) \\
& - v\int \Big(\vec{\nabla}_{\perp}E_z(\vec{r_d},\vec{r_t}) - \frac{\partial E_{\perp}(\vec{r_d},\vec{r_t})}{\partial z}\Big)dt\Bigg]\Bigg) \quad , \\
\frac{\partial}{\partial s}\omega_{\perp}(\vec{r_d},\vec{r_t},\tau) =& -\frac{1}{q_d}\int dz \Bigg[\frac{\partial}{\partial s}\vec{E_{\perp}}(\vec{r_d},\vec{r_t}) \\
& - v\int \Big(\vec{\nabla}_{\perp}E_z(\vec{r_d},\vec{r_t}) - \frac{\partial E_{\perp}(\vec{r_d},\vec{r_t})}{\partial z}\Big)dt\Bigg] \quad , \\
\frac{\partial}{\partial s}\omega_{\perp}(\vec{r_d},\vec{r_t},\tau) =& -\frac{1}{q_d}\int dz \Bigg[-\frac{\partial}{\partial z}\vec{E_{\perp}}(\vec{r_d},\vec{r_t}) \\
& - v\int \Big(\vec{\nabla}_{\perp}E_z(\vec{r_d},\vec{r_t}) - \frac{\partial E_{\perp}(\vec{r_d},\vec{r_t})}{\partial z}\Big)dt\Bigg] \quad , \\
\frac{\partial}{\partial s}\omega_{\perp}(\vec{r_d},\vec{r_t},\tau) =& -\frac{1}{q_d}\int dz \Bigg[-\frac{\partial \vec{E_{\perp}}}{\partial z} + \Big(\vec{\nabla}_{\perp}E_z + \frac{\partial \vec{E_{\perp}}}{\partial z}\Big)\Bigg] \quad .
\end{aligned} \tag{2.81}$$

The first and the third terms inside the integral will cancel each other and the Equation 2.81 becomes:

$$\frac{\partial}{\partial s}\omega_{\perp}(\vec{r_d},\vec{r_t},\tau) \;=\; -\frac{1}{q_d}\int dz\Big(\vec{\nabla}_{\perp}E_z\Big) = \vec{\nabla}_{\perp}\omega_{\parallel}(\vec{r_d},\vec{r_t},\tau) \quad . \tag{2.82}$$

Equation 2.82 shows that the gradient of the longitudinal wake function is equal to the gradient of the transverse wake function.

2.2.2. Impedances

The analogy of wakefields in frequency domain is impedance and it is related through Fourier analysis. Impedance is practical way to study for specific EM problems because Maxwell's equations are linear. It is a complex function which consists of real and imaginary parts. The real part, so-called "resistive" is responsible for energy loss as well as growth rates of the instabilities and the imaginary part, known as "reactive"

is responsible for frequency shift [16].

Impedance can be described as the Fourier transform of the single particle wake function. The impedance equation is given (by using the relation of $s = \nu\tau$) as:

$$Z(\vec{r_d}, \vec{r_t}, \omega) = -\int_{-\infty}^{\infty} W(\vec{r_d}, \vec{r_t}, s) e^{\frac{-i\omega s}{v}} \frac{ds}{v} \quad . \tag{2.83}$$

The equations of the components in longitudinal and transverse directions are:

$$Z_{\parallel}(\vec{r_d}, \vec{r_t}, \omega) = -\int_{-\infty}^{\infty} d\tau \omega_{\parallel}(\vec{r_d}, \vec{r_t}, \tau) e^{-i\omega\tau} \quad , \tag{2.84}$$

$$Z_{\perp}(\vec{r_d}, \vec{r_t}, \omega) = -j\int_{-\infty}^{\infty} d\tau \omega_{\perp}(\vec{r_d}, \vec{r_t}, \tau) e^{-i\omega\tau} \tag{2.85}$$

where the angular frequency is $w = 2\pi f$.

The analytical calculation of impedance is possible for a few structures such as uniform, cylindrical beam pipes or pill-box cavities with (rotational) symmetry. For complicated geometries, numerical techniques can be used and dominant resonance modes and frequencies can be computed. Computer codes can also calculate the wake potentials in the time domain by doing Fourier transformation and using long wakes of short bunches in the code can provide more accurate and yield results with higher frequency resolution. Various results obtained with such computer codes will be described and explained in the next chapter [13, 22].

2.2.2.1. Equivalent Circuit Analogy. Impedance as a function of frequency can be defined as the ratio of the complex voltage and current. Impedance is commonly used for solving the circuit problems in frequency domain. According to this circuit-impedance analogy, an accelerating cavity can be modelled with an equivalent circuit.

As seen in Figure 2.5, a beam passing through a cavity can be described as an equivalent RLC parallel circuit. In this respect, the beam behaves like a current source varying in time and represents resistance R, the metallic walls of the cavity serve as

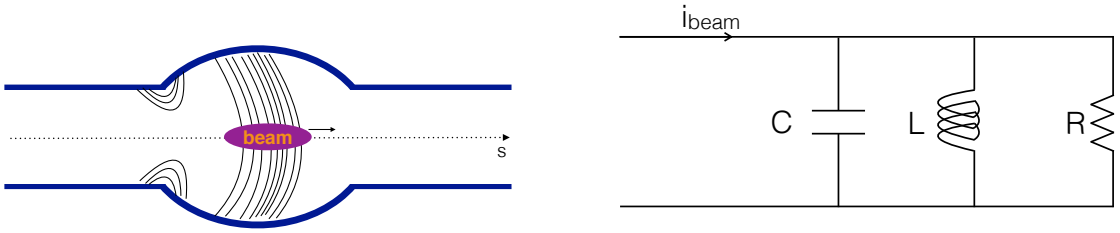

(a) Schematic of a beam passing through a cavity

(b) Parallel RLC circuit

Figure 2.5. Schematic of the RLC parallel equivalent circuit driven by the beam current.

capacitance C, and the induced fields on the cavity due to moving charges produce inductance L. This concept is commonly known as beam coupling impedance.

The impedance Z (Appendix G) for an equivalent circuit can be written as:

$$Z(\omega) = \frac{1}{\frac{1}{R} + j\omega C + \frac{1}{j\omega L}} \quad . \tag{2.86}$$

2.3. Basic Concepts of RF Engineering

2.3.1. Quality Factor

The quality factor can be described as a dimensionless parameter that is related to energy losses of a resonant circuit. It depends on material conductivity. It can be formulated as the ratio of the stored energy W to the energy dissipated P per cycle:

$$Q = \omega_{res} \frac{W_{stored}}{P_{dissipated}} \tag{2.87}$$

where $\omega_{res} = \frac{1}{\sqrt{LC}}$ is the angular frequency at the resonance condition of a parallel RLC circuit. This relation means that lower energy loss indicates higher Q-factor.

The description of the Q-factor can be given three different ways as:

$Q_0 = \frac{\omega W}{P_{dissipated}}$: Unloaded Q-factor is the stand alone cavity mode which is the unperturbed system and it depends on the surface resistance.

$Q_L = \frac{\omega W}{P_{external}+P_{dissipated}}$: Loaded Q-factor is the quality factor for the while system taking into account the losses in both the resonator and the generator as well as the measuring device.

$Q_{ext} = \frac{\omega W}{P_{external}}$: External Q-factor is the quality factor attributed to the losses in the generator and the measuring device $P_{external}$ excluded the resonator losses.

(2.88)

and they are related with each other as:

$$\frac{1}{Q_L} = \frac{1}{Q_0} + \frac{1}{Q_{ext}} \quad . \tag{2.89}$$

It is also worth noting that loaded Q-factor can be obtained from the transmission plot:

$$Q_L = \frac{f_{res}}{\Delta f} \tag{2.90}$$

where $\Delta f = f^+_{3dB} - f^-_{3dB}$ is the width of the range of 3dB value and $f_{res} = \frac{1}{2\pi}\frac{1}{\sqrt{LC}}$ is the resonance frequency.

Consider the simplest metallic structure, pillbox cavity that its dominant mode is TM_{010} mode. Due to having $n = 1$ equality in the middle subscript, the TM wave will be axis symmetric. The field distribution is like a narrow peak with big amplitude. After putting a probe into the cavity from a tiny hole in it, the field can be detected. By moving the probe inside slowly, the amplitude of the field distribution decreases and the distribution broadens. This broadened field means that coupling with the probe has started.

The coupling coefficient κ is the crucial value for the analysis of the cavity design when the electromagnetic coupling of the cavity to an input coupler is considered. It is related with the loaded and external Q-factors as well as unloaded Q-factor via [23]:

$$Q_{loaded} = \frac{Q_0}{1+\kappa} \quad , \tag{2.91}$$

$$Q_{external} = \frac{Q_0}{\kappa} \quad . \tag{2.92}$$

The unloaded quality factor cannot be found from measurements but the approximate value of Q_0 can be obtained by using Equation 2.91. For the reliability of measurements, it is important to get the coupling factors as close to zero as possible and the Q_{loaded} value can be approximately equal to Q_0. By using 3dB bandwidth, Q_{loaded} can be obtained and Q_0 value can thus be estimated.

2.3.2. Shunt Impedance, R and Cavity Geometry Factor, R over Q

The shunt impedance characterizes the efficiency of the accelerating mode. It is the parameter to adjust for maximizing an accelerating field for a given power loss:

$$R = \frac{V_{acc}^2}{2P_{dissipated}} \quad . \tag{2.93}$$

The R/Q, known as the cavity geometry factor, is independent of surface properties which specify the power loss and it depends only on pure geometry.

$$X = \frac{R}{Q} = \omega_{res} L = \frac{1}{\omega_{res} C} = \sqrt{\frac{L}{C}} \quad . \tag{2.94}$$

2.3.3. Voltage Standing Wave Ratio and Reflection Factor, Γ

When power is applied to a system, some of this power is delivered to a load in the system via transmission lines or waveguides. When some of these incident waves are reflected and these incident and reflected waves can result in standing waves. If the waves are measured in terms of voltages, voltage standing wave ratio (VSWR) can be defined as the ratio of the maximum and minimum measured voltages along the transmission line.

Reflection factor is a measure of the impedance matches to the load and the characteristic impedance of the line. It is also known as the ratio of the strengths of the electric fields of the reflected waves over the incident/forward travelling waves.

$$\Gamma = \frac{\mid \vec{E} \mid \text{ of reflection}}{\mid \vec{E} \mid \text{ of transmission}} = \frac{Z_L - Z_c}{Z_L + Z_c} \tag{2.95}$$

where Z_L is the terminating/load impedance and Z_c is the characteristic impedance which is generally chosen to be equal to 50 Ω. It is worth mentioning that common measurement devices and cables have connectors which possess 50 Ω characteristic impedance so that this impedance value is usually the favourable one.

There are three specific cases of the reflection factors;

$$\begin{aligned} \Gamma = +1 &\rightarrow \text{open circuit when } z \rightarrow \infty, \\ \Gamma = 0 &\rightarrow \text{open circuit when } z = 1, \\ \Gamma = -1 &\rightarrow \text{matched load circuit when } z = 0 \end{aligned} \tag{2.96}$$

where z is the ratio of the load and characteristic impedance $= z = Z_L/Z_c$.

2.3.4. Decibel

The unit of decibel is commonly used in RF engineering. When a person deals with very large or small numerical range, take its logarithm is rational thing. Decibel expresses the base ten logarithm of the ratio of two signal powers and it is a dimensionless quantity.

$$P\ [dB] \quad = \quad 10 \times log_{10}\left(\frac{P_{out}}{P_{in}}\right) \tag{2.97}$$

where P_{in} is an incoming signal power and P_{out} is an outgoing signal power. Signal amplitude is also frequently expressed in dB. Because the signal amplitude is proportional to the square root of the power, the expression for the ratio of two voltages becomes

$$V\ [dB] \quad = \quad 20 \times log_{10}\left(\frac{V_{out}}{V_{in}}\right) \tag{2.98}$$

where V_{in} is an input voltage and V_{out} is an output voltage.

In addition to dB, dBm is also common unit which normalizes any power reading to 1 mW into 50 Ω. 1 mW is taken for input signal power and Equation 2.97 becomes a ratio of P_{out} to 1mW [24].

$$P\ [dBm] \quad = \quad 10 \times log_{10}\left(\frac{P_{out}}{1\ mW}\right) \tag{2.99}$$

Some commonly encountered dB values and their conversions to power ratio and amplitude ratios are listed in Table 2.3.

Table 2.3. dB Values and their equivalent values in power and voltage ratios

[dB]	**Power Ratio**	**Voltage Ratio**
-50	0.00001	0.003162
-40	0.0001	0.01
-30	0.001	0.03162
-20	0.01	0.1
-10	0.1	0.3162
-3	0.50	0.71
-1	0.74	0.89
0	1	1
1	1.26	1.12
3	2.00	1.41
10	10	3.162
20	100	10
30	1000	31.62
40	10000	100
50	100000	316.2
$n \times 10$	10^n	$10^{\frac{n}{2}}$

2.3.5. Scattering Parameters

For high frequencies, it is convenient to describe a given network in terms of 'waves' than voltages or currents. For practical reasons, the description in terms of incoming and outgoing waves has been introduced.

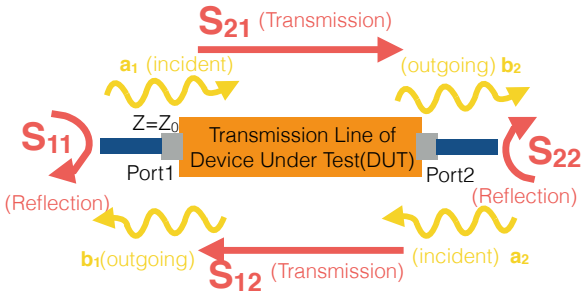

Figure 2.6. Schematic of a 2-port network system.

S-parameters are basically the characterization of n-port networks and can be described as the ratio of the relative powers. (Signal power at RF and microwave frequencies is more easily/efficiently quantized than voltages or currents [25]). Scattering matrix S_{ij} is defined in terms of S-parameters as a complex matrix. The matrix indicates reflection and transmission properties of the network in frequency domain. According to S_{ij} notation, the first subscript denotes the port where the signal arises and the second one represents the port where the signal is applied. When i is equal to j, these S_{ii} coefficients are named as reflection value or return loss. For S_{ij} coefficients, transmission value or insertion loss are commonly used terminologies.

Considering a 2-port network, the matrix S is written as

$$S = \begin{pmatrix} S_{11} & S_{12} \\ S_{21} & S_{22} \end{pmatrix}.$$

These coefficients can be considered as reflected waves normalized to the incident waves and they can be written (as shown in the Figure 2.6) as:

$$\begin{aligned} S_{11} &= \frac{b_1}{a_1} \mid_{a_2=0} : \text{Input reflection coefficient} \quad , \\ S_{12} &= \frac{b_1}{a_2} \mid_{a_1=0} : \text{Backward transmission coefficient} \quad , \\ S_{21} &= \frac{b_2}{a_1} \mid_{a_2=0} : \text{Forward transmission coefficient} \quad , \\ S_{22} &= \frac{b_2}{a_2} \mid_{a_1=0} : \text{Output reflection coefficient} \quad . \end{aligned} \tag{2.100}$$

A network analyzer is one of the most common and valuable measurement devices for RF studies. Their effective frequency range can be from several Hz to a few GHz and the resolution can be up to 0.1 Hz. When a device under test (DUT) is excited via a network analyzer with a specific input, the output is obtained in terms of a complex number for each frequency. The output information of the DUT determines the scattering parameters.

3. SIMULATIONS OF BPH WITH AND WITHOUT SHIELDING

The source of impedance is caused for decreasing the beam quality and increasing the number of instabilities in the machine [8, 9]. In this regard, the 104 horizontal beam position monitors (BPHs) next to the quadrupole focusing (QF) magnets are an important source of impedance at 1.3 GHz resonance in the SPS. A shield placed at the vacuum flange in the junction of BPH and QF magnet was modelled for mitigating the effect of this source of impedance. Several shielding campaigns have been started for mitigating the impedance sources at the machine including the vacuum flanges since 2000 [26]. After 2000, the status of these shields was not checked. Hence, there was a need to find a method to identify the presence and/or condition of these shields (and this task was deemed obligating for raising the beam quality). For this reason, the BPH provided for measuring the undesired resonance without dismounting the positions of the vacuum flanges.

BPH has the shape of shoe box and has two crossed capacitive triangular parallel plates. The idea of beam position monitors is to measure charges induced by the electric field of beam on the capacitive/metal plates. An AC signal occurs on the plates and it causes coupling via an amplifier system connected to the plates. This coupling provides signal reading of the induced charges to get information about position of the bunch [27]. There are two N-type of connection ports, asymmetrically located on the BPH, to read the signal. These N-type connectors were considered as a means of measuring the undesired 1.3 GHz resonant frequency with the help of a VNA. However, that resonance was not detectable via the ports because they are located pretty far away from the vacuum flange to obtain relatively low frequency signal at 1.3 GHz.

Two similar test measurement setups were implemented in the laboratory. One of them was for detecting the 1.3 GHz resonant via a probe to prove the efficiency of the shield. The second one was for detecting a clear indicator that can be measured

from the N-type connectors in the SPS tunnel. The latter one was needed to be used in the SPS tunnel because the only possible solution for obtaining a signal from the device was a transmission (2-port) measurement. Due to the measurement setup, the 1.3 GHz resonance was not detectable and this resonance was not expected to be observed during measurements. Hence, simulations as well as measurements were carried out up to 4 GHz to get an indicator resonance. Higher frequencies were scanned for the indicator due to the cutoff frequencies of beam pipes and 4-convolution and 10-convolution bellows. Because of using the BPH for the measurements, simulated geometry was modelled with not only vacuum flange but also BPH. In brief, results of eigenmode and wakefield simulations of the model will be examined in this chapter.

Two different kinds of 3D electromagnetic (EM) simulations were performed in CST MWS to calculate wakes and impedances:

- eigenmode simulation, for the study of the EM-field pattern of specific modes,
- wakefield simulation, to calculate the beam coupling impedance.

3.1. EM-Simulation Results

The shield was designed to be installed at the location of vacuum flange and 10-convolution bellow (as seen in Figure 3.1) to provide a smooth transition between two slightly different kind of beam pipes which are main bending magnet (MBA) and QF beam pipes. The comparison of longitudinal beam impedance traces is shown in Figure 3.2 as a function of mode frequency. The function was calculated in terms of shunt impedance R and quality factor, Q (as shown in Figure 3.3) which were obtained from eigenmode simulation by using Equation 3.1 (Appendix G).

$$Z(f) \;=\; \sum_n \frac{R_n}{1 + jQ_n\left(\frac{f}{f_n} - \frac{f_n}{f}\right)} \quad . \tag{3.1}$$

Here R_n, Q_n, and f_n are the shunt impedence of the nth mode, the quality factor of the nth mode, and the resonance frequency of the nth mode, respectively. Every mode is

calculated for one frequency and added to each other so that the addition provides an impedance value of that frequency. The impedance values for each frequency within the range (1-4000 MHz) have been computed and plotted the magnitudes of these values (as shown in Figure 3.2) because impedance is a complex number. 120 modes were

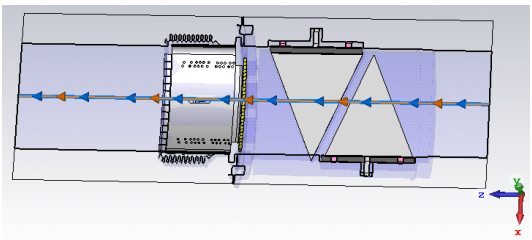

(a) Cut plane of top view of the model including the shield

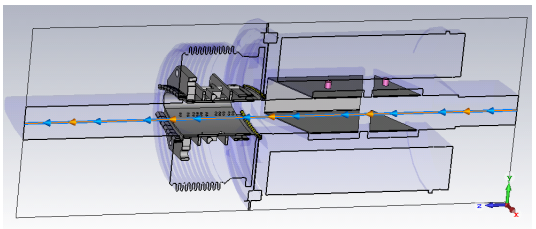

(b) Cut plane of side view of the model including the shield

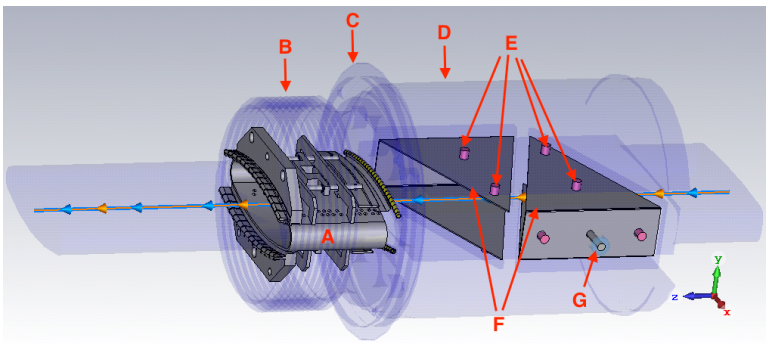

(c) 3D model including the shield

Figure 3.1. 3D geometry with BPH and 10-convolution bellow in CST MWS. A, B, C, D, E, F and G are the shield, the 10-convolution bellow, the vacuum flange, BPH vacuum tank, electrodes, triangular capacitor plates and one of the BPH ports, respectively.

calculated within the frequency range from 1 MHz up to 4000 MHz from eigenmode simulations. For the impedance model, the relevant frequency range is up to around 2 GHz. However, some microwave instabilities can be hidden at higher frequencies. For this reason, the simulations were carried out up to 4 GHz to make sure that there is no invisible/veiled instability. According to the Figure 3.2, implementing a shield inside the position eliminates the resonances at low frequencies including the undesired/targeted peak at 1.3 GHz.

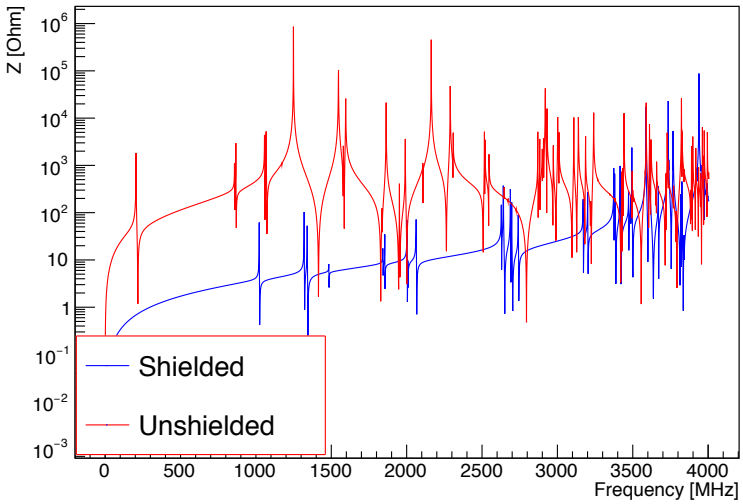

Figure 3.2. Longitudinal beam impedance as a function for mode frequency obtained from eigenmode simulation

In addition to the eigenmode simulation, wakefield simulations were done for shielded and unshielded models as well as the model of BPH, itself which means the model of BPH without the BPH tank, the 10-convolution bellow and the vacuum flange was simulated. As can be seen in Figure 3.4, the amplitudes of the desired frequency at 1.3 GHz have significant difference between the models with and without shielding. BPH itself model was simulated to understand which resonant frequencies are because of the structure of the BPH, itself. It is worth noting that the EM-field configurations of some of these resonances have been illustrated in Appendix F. To conclude, these simulations clearly demonstrate that the presence of the shield is indeed fulfilling its purpose. The shield mitigates one of the known sources of instabilities.

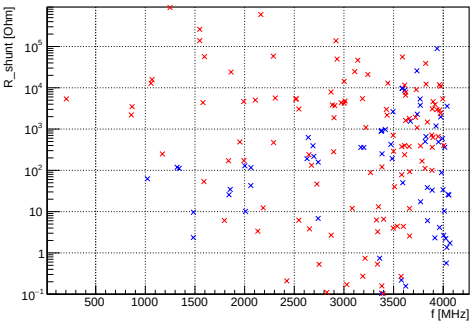

(a) R-shunt

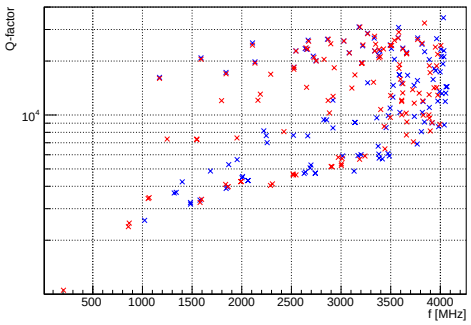

(b) Q-factor

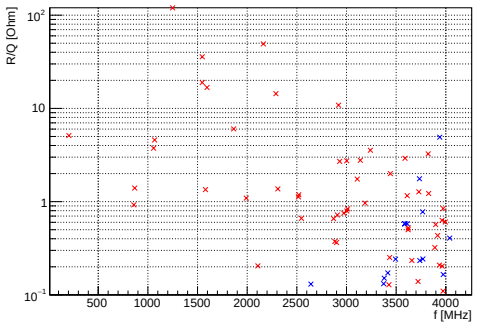

(c) R over Q

Figure 3.3. Shunt impedance and quality factor values from eigenmode simulation

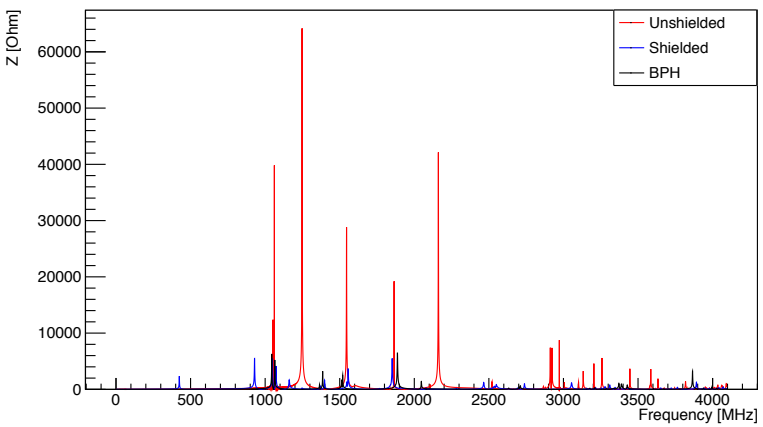

Figure 3.4. Longitudinal beam impedance as a function for mode frequency obtained from wakefield simulation. BPH with black trace denotes simulation without the BPH tank, the 10-convolution bellow and the vacuum flange

4. TEST MEASUREMENTS

The aim of the shields is to eliminate the resonance frequencies at 1.3 GHz and 1.6 GHz. One of the culprits of the instabilities is the resonance at 1.3 GHz in the junction of the vacuum flange between the BPH and QF magnet. Several campaigns, which were mainly aimed to shield pumping ports have been performed to mitigate the multi-bunch instabilities since 2000. According to the reports of these campaigns, 67 shields have been implemented to BPHs. However, there is no information about the current status of these shields [26].

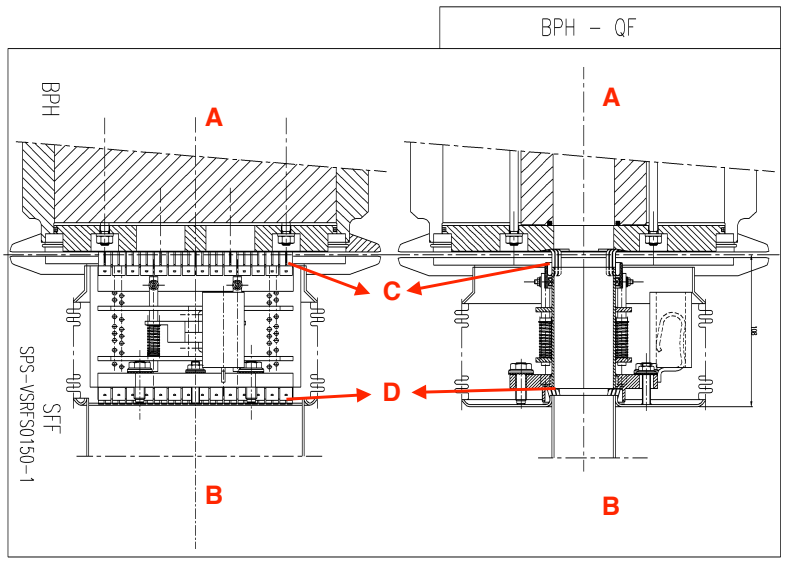

Figure 4.1. Drawing of the shield [4]

In Figure 4.1, the main parts of the drawing are labelled with capital letters. *A* and *B* indicate BPH and QF sides of the interested geometry respectively. *C* shows RF fingers that provide the RF connection between shield and vacuum flange. *D* is the side of the element that is welded to the QF magnet side. The pictures of the RF fingers and vacuum flange can be seen in Figure 4.2.

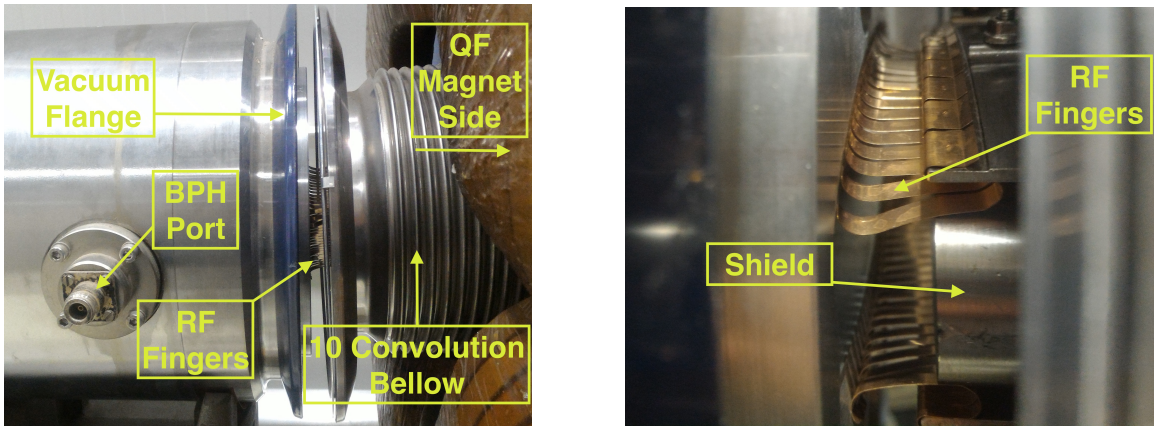

(a) Vacuum Flange (b) Shield with RF Finger

Figure 4.2. The pictures of the vacuum flange as well as the shield with RF fingers.

Dismounting of these parts in the SPS tunnel for checking the situation of the shields is not practical. There are two choices to get the information; either an x-ray scan or the transmission measurement via the scattering parameters. The x-rays scanners are not favoured as a diagnostic tool for the shields because they are troublesome because of not only increasing radiation issues but also for being huge machines. Instead of x-rays, impedance measurements constitute a more preferable method which require a minimum number of equipment to be used. Moreover, the measurements can be performed via the coaxial ports present on the device in the current case. In this respect, the S-parameter measurement method was used and will be explained in this chapter.

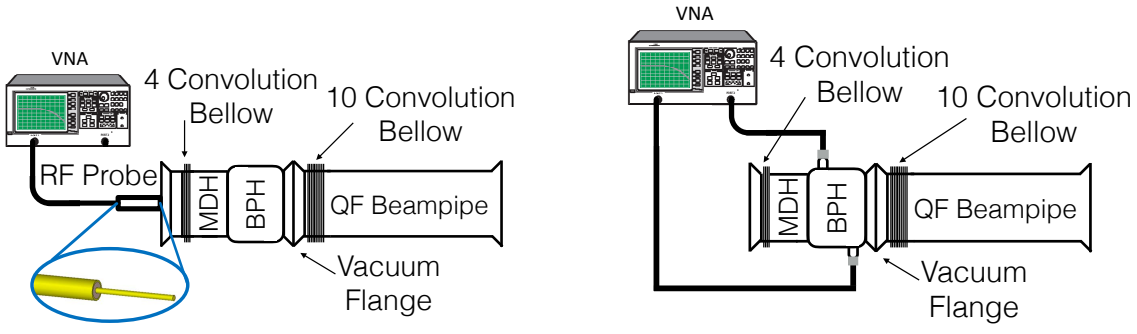

(a) Probe measurement (b) Transmission measurement

Figure 4.3. Test measurement setup in the laboratory.

The reason of beam-coupling impedance at 1.3 GHz is the 10-convolution bellow in the BPH–QF junction. Because of this, the shields were designed, manufactured and implemented to 67 of BPHs. The proof of the effectiveness of the shield and the frequency signal variances around 1.3 GHz could not be obtained directly in the SPS tunnel because it is not possible to dismount the machine and to probe the shielded area. Therefore, a test platform for reflection measurement was prepared for verifying the presence of the shield and their status as seen in Figure 4.3(a). Unfortunately, even that reflection measurement is impractical for the vacuum flanges on the beamline, so apart from the reflection measurement, a transmission measurement is needed for validating the feasibility of the coaxial ports of BPHs in the broadband range. Hence, another test setup was performed as presented in Figure 4.3(b).

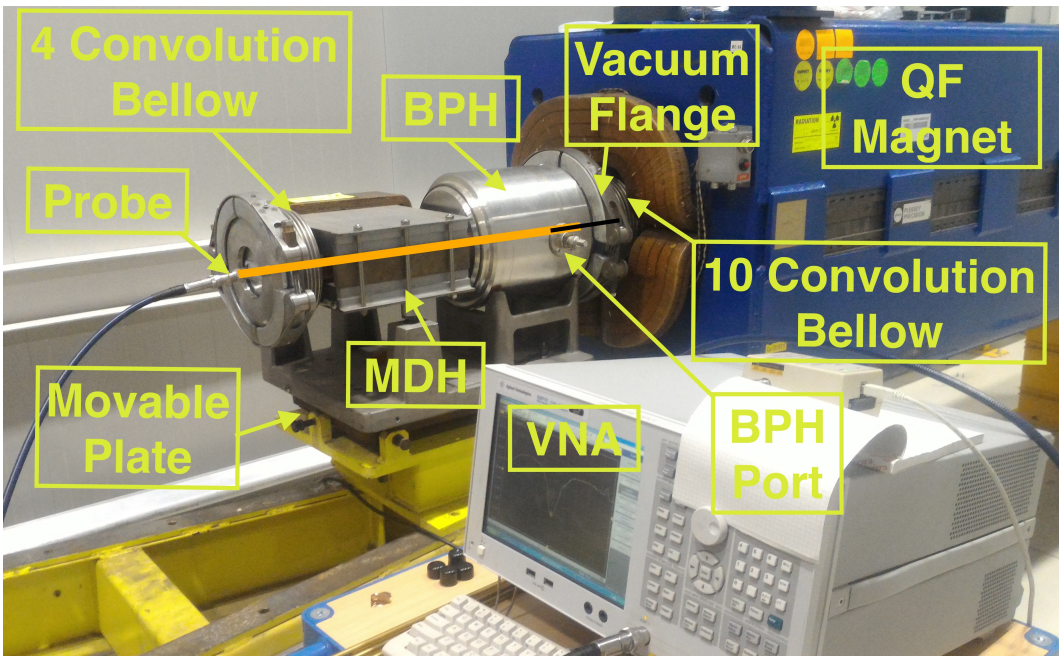

Figure 4.4. Picture of test measurement setup in the laboratory. Orange line drawn on the photo represents the probe inserted into the system reaching up to the target location within the vacuum flange.

Figure 4.4 shows the actual setup that was used for the probe measurement which checks the function of the shield at 1.3 GHz, similar to the schematic in Figure 4.3(a). The probe being used is shown in the Figure 4.5. It is 1 meter long and matched with 50 Ω impedance.

When the probe is put inside the setup, it becomes coupled with some resonances. In other words, the probe creates some artificial modes which are easily detectable during the measurement. These modes can be suppressed by changing the position of the probe. (At the beginning the receiver wire had a loop shape but it could not reach the desired region inside the beam pipe. Hence, this inductive loop was replaced with a capacitive one which is in the shape of a simple antenna and the measurement was done by using this antenna/capacitive probe. It is worth noting that a loop probe mainly detects the magnetic field, while an antenna-shaped probe usually detects the electric field.)

Figure 4.5. Picture of loop probes that were used.

In the probe measurement, the desired resonance peak was at 1.3 GHz so the frequency range in VNA was adjusted to cover from 1.2 GHz to 1.4 GHz. At the beginning, several peaks instead of the one at 1.3 GHz were observed. After moving the probe in and out to a few millimetres, some differences in the amplitude and the peak frequency of some of the traces were observed. The varied peaks are the so called probe modes and they could be eliminated. Besides the probe modes, the only remaining and unchanged peak was the undesired resonance frequency at 1.3 GHz. For examining the actual effectiveness of the shield, a test was conceived in which the contact of the RF fingers on the shield would be decreased. This was provided

for sticking Kapton tape on the fingers as well as moving pieces of the setup further away from each other by means of a movable plate. During the measurements, the shield was welded as one-sided onto the device in the side of the QF magnet. Kapton tape attached to the RF fingers allowed a check of what happens in setups with really poorly contacted shielded. The BPH setup was mounted on a movable plate. Hence, RF fingers could be released and the RF contact could be reduced by moving the BPH away from the QF magnet. When the setup was located further from the QF magnet, the situation resembled a poorly contacting shield, which is similar to unshielded case. While the BPH was in its closest position to the QF magnet, the RF fingers were in full contact with the wall. This situation represented the ideal case for the shielded setup. Finally, another measurement was also done for partially contacted RF fingers scenario by adjusting the movable plate so that an intermediate amount of space was left out between the BPH and the QF magnet.

Figure 4.6 shows the results of these three test cases. The green trace is taken from the setup with Kapton tape which can be assumed to represent the really poor contact case, near the unshielded scenario. The blue one is measured from the shielded BPH with RF fingers in full contact. The pink trace represents the situation in which the RF fingers are partially connected. The reflection value at 1.3 GHz for the unshielded scenario is around -1.8 dB. This value decreases with the implementation of a shield and it becomes -0.7 dB. For the partial connection measurement, the reflection is around -1.1 dB. These measurements provide us with a baseline to compare against and the status of any shield can be estimated by doing this measurement and looking at the amplitude of the peak/depression.

4.2. Transmission (2-Port) Measurements

Before taking measurements at the tunnel, an indicator at some narrow frequency range must have been found via using BPH coaxial ports. Measurements were done at a wide range starting from 1 MHz to 4 GHz via N-type coaxial ports of the BPHs (as seen in Figure 4.3(b)). Wide range trace is significant for observing all possible situation and for a further possible investigation about the BPH in the SPS if it is needed. The

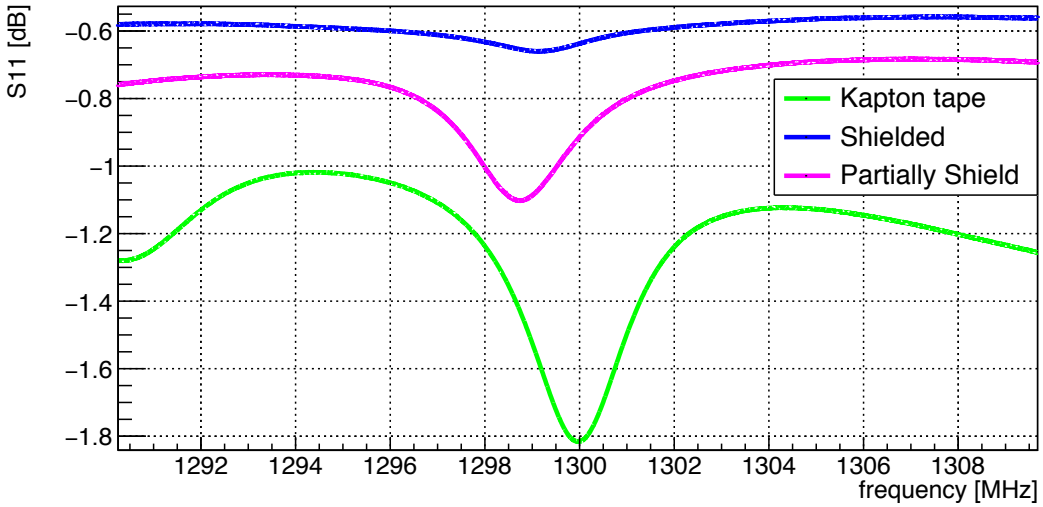

Figure 4.6. Probe measurements at 1.3 GHz for the cases of unshielded, shielded and partially shielded flanges shown in green, blue and pink respectively.

transmission measurements were performed in this range using 8001 sweep points and IF bandwidth of 1 kHz.

When the broad traces have been taken via VNA, the analysis were done by separating smaller subranges. Within the small subranges, some varied resonances around 3.7 GHz were observed depending on the presence of the shield in the setup. Figure 4.7 indicates the test measurement results of the two cases around 3.7 GHz. The green trace is the measurement of the unshielded setup and the blue one is the result of the shielded setup. In the absence of the shield, one resonance peak around 3.7 GHz is relatively damped as seen in the insertion loss in which it is the transmission coefficient (S21 vs. frequency) plot in Figure 4.7(a). This behaviour is also observed from the phase graph in Figure 4.7(b). The difference of them can be observed via the reflection plots in Figure 4.8 as well. Consequently, the analysis were done by using the insertion loss measurements due to the significant difference. The analysis could have done by using the reflection traces but the transmission signal are more clear than the reflection ones.

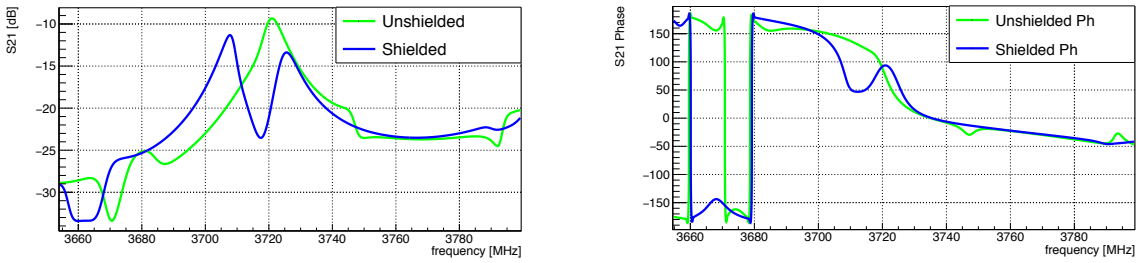

(a) Magnitude of Insertion Loss (b) Phase of Insertion Loss

Figure 4.7. Insertion loss of unshielded and shielded data taken in the laboratory. Green trace shows the unshielded data and blue one indicates the shielded data.

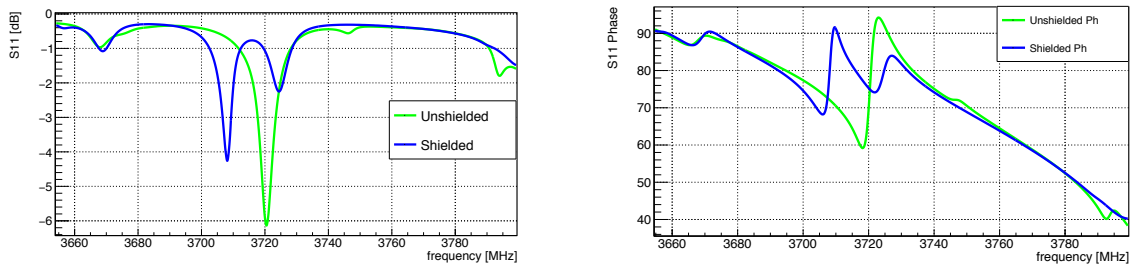

(a) Magnitude of Reflection (b) Phase of Reflection

Figure 4.8. Reflection of unshielded and shielded data taken from laboratory. Green trace shows the unshielded data and blue one indicates the shielded data.

4.3. Sensitivity Measurements

The sensitivity measurements were done for understanding the effects of nearby elements next to the vacuum flange on the resonant frequency at 1.3 GHz in which the elements are 4-convolution and 10-convolution bellows. In addition to nearby elements, the effects of the open-ended and close-ended beam pipes on the resonance were also investigated. For these purposes, four different measurements were performed. These are: open ended flanges at the ends of the beam pipes, closed-ended flanges, disturbed 4-convolution bellow before the BPH and disturbed 10-convolution bellow after the BPH. The relevant part of the machine consists of BPH, vacuum flange, 10-convolution bellow and QF magnet. Before the BPH, different elements such as 4-convolution bellow, sextupole or octupole lenses are connected at some sectors in the tunnel. Therefore, the effects of the various elements were desired to observe. Since a significant amount of time has passed after the commissioning of the shields on the SPS, some bellows could have gotten damaged and these ones can affect the undesired resonance as well as

beam quality. As a result, the sensitivity measurements were needed for these reasons.

The most sensitive elements should be the bellows and Figures 4.9, 4.10 show that they are not as sensitive as expected. The effect of the volumetric changes should be observed at high frequency but Figures 4.9(b), 4.10(b) demonstrate that the fluctuation at 3.7 GHz frequency of the indicator is almost negligent. This means that the BPH with elements of varying geometry would not affect the measurement results.

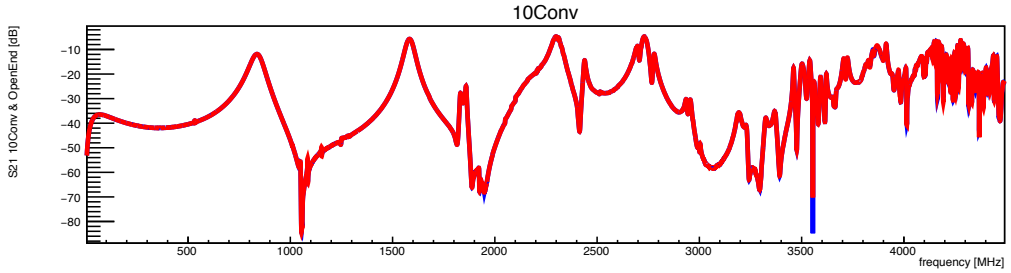

(a) Insertion loss plots drawn top of each other

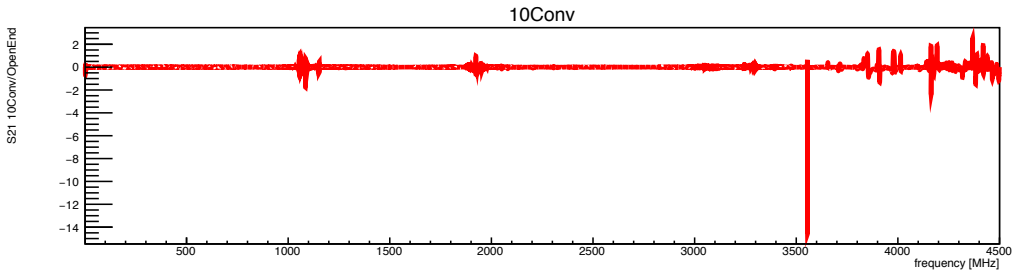

(b) Ratio of the insertion loss plots of the disturbed 10-convolution bellow to the open ended beam pipe

Figure 4.9. Insertion loss comparison of the data taken from open ended beam pipe (blue) and disturbed 10-convolution bellow (red). The ratio of the two plots is shown at the bottom.

The measurement setup in the laboratory had closed ends, unlike the actual setups in the tunnel. In the measurements at the SPS, the beam pipes have open ends which means that the boundaries are not terminated. Sensitivity measurements were done to observe the consequences of the open/close ends at the resonant frequency in the setup. The outcomes indicate that the effect of the opening flanges could be negligible. The reason is that the cutoff frequency of the vacuum flanges is much higher than the frequency at 3.7 GHz. Moreover, this insignificant effect means that

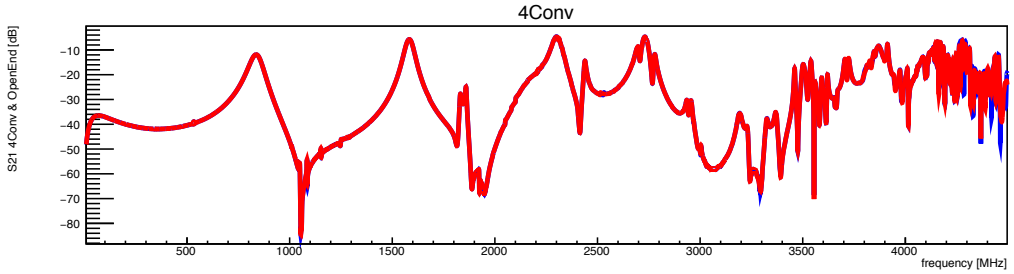

(a) Insertion loss plots drawn top of each other

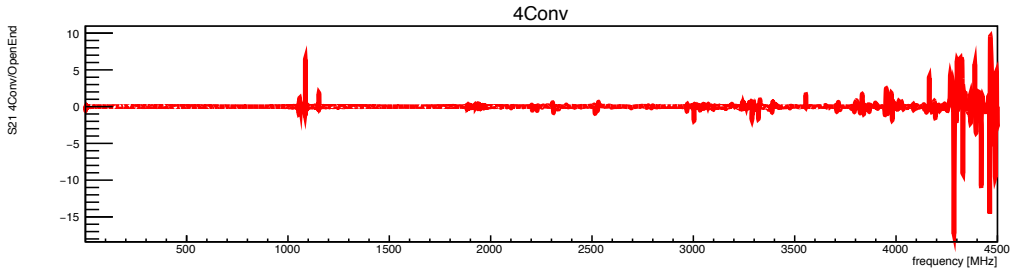

(b) Ratio of the insertion loss plots of the disturbed 4-convolution bellow and open ended beam pipe

Figure 4.10. Insertion loss comparison of the data taken from open ended beam pipe (blue) and disturbed 4-convolution bellow (red). The ratio of the two plots is shown at the bottom.

the chosen indicator at 3.7 GHz is dominant in the BPH system and is independent from the surrounding objects.

5. TUNNEL MEASUREMENTS AND ANALYSIS

During 2017 Year End Technical Stop (YETS), as many of the flanges were measured in the SPS tunnel as permitted by the time constraints. It was not possible to measure some of the flanges due to their locations in highly activated zones such as the sites of beam dumps and septa. The measurements were done using a VNA that is connected to the ports of BPHs that are normally connected to coaxial lines that carry the BPH output signal. (The measurement setup can be seen in Figure 5.1.) The VNA swept the range from 1 MHz to 4 GHz with 8001 sweep points and an IF bandwidth of 1 kHz. In total 104 vacuum flanges of the interest are in the SPS machine, of which 70 were measured [28].

5.1. Measurement

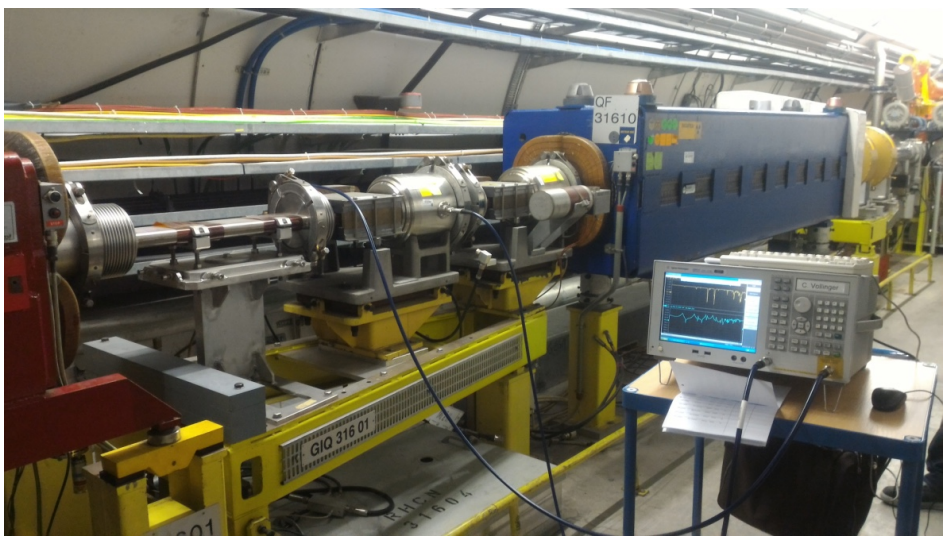

Figure 5.1. Transsmission measurement setup in the tunnel.

In principle, the measurement results should yield whether a given flange falls into one of two broad categories; vacuum flange with a shield or without any shield. However, there is one more slightly different type of behaviour; the case where a shield has only a partial contact resulting in reduced performance. It is worthwhile to mention that the vacuum flanges were labelled according to their shielding status during the

installation period. The measurements were cross-checked the accurateness of the list.

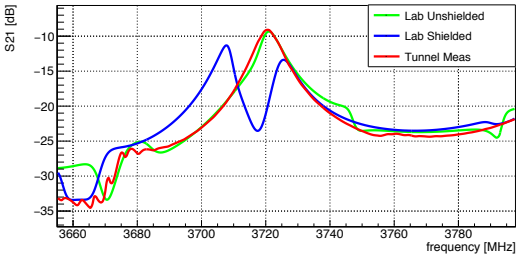

(a) Unshielded

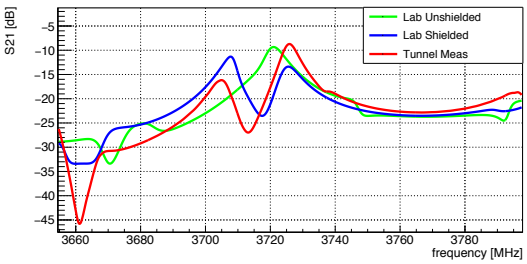

(b) Shielded

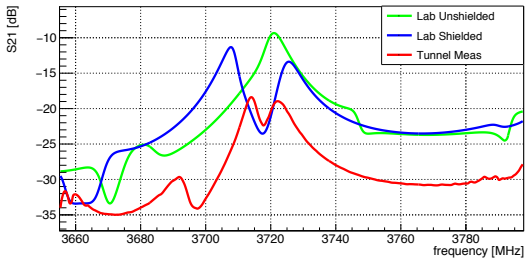

(c) Partially Shielded

Figure 5.2. Three examples of the different cases from the tunnel measurements. Green, blue and red lines are unshielded, shielded and partially shielded data traces respectively.

Figure 5.2 demonstrates examples of the three different kinds of results from the measurements done in the tunnel. Each trace of the tunnel measurement shown in red has been drawn together with the traces taken from the test measurement setups for unshielded (green) and shielded (blue) cases. By comparing to the lab and the tunnel measurements, the status of the shields can be analyzed. Figure 5.2(a) shows an example for the unshielded case. As seen in the figure, data from the SPS tunnel has a good agreement with the lab measurement of the unshielded case and it was indeed labelled as unshielded. Data in Figure 5.2(b) look similar to the shielded lab measurement and the BPH, which the data belongs to had indeed been labelled shielded. An instance of the imperfect shielded is shown in Figure 5.2(c). Although data behave similar to the unshielded lab measurement, it had been labelled as shielded. The reason of this can be the lack of a good RF contact.

The number of shielded and unshielded BPHs are documented as in Table 5.1 by comparing to the expectations from the labels and the observations with the measurement technique.

Table 5.1. Summary of the results from the SPS tunnel measurements

Orijinal Label	**Measured as Shielded**	**Measured as Unshielded**	**Poor Contact or Bad Trace**	**Total**
Shielded	28	4	15	47
Unshielded	5	14	4	23

Among the 70 measurements in the tunnel, 23 of them belong to devices that are listed as unshielded. According to the applied method, only 14 of 23 BPHs are identified to be unshielded, while five appeared to be shielded and the remaining four could not be identified due to bad traces. The misidentification can be caused due to the geometric errors at high frequencies or there is a small possibility that some might have an implemented shield but got mislabelled. (For a full list and whole traces see Appendix A.)

Among the 70 measurements in the tunnel, 47 of them belong to devices that had been labelled as shielded. 28 of these were found to be compatible with the results of the shielded lab measurements. The other 19 BPHs have unclear traces or have a similar behaviour with unshielded condition. The reason can be partial or full loss of RF contact. Amongst that 19, four that appear to be unshielded should especially be investigated during the LS2 because they may contribute to the instability threshold of the beam.

6. RF POWER TRANSMISSION

Until now, we have discussed low amplitude RF waves that carry signals such as beam position monitors. RF waves are also used to carry high power, for example from an RF power supply unit (PSU) to an RF cavity. An RF circulator and transmission line, all operating at 800 MHz have been designed, built and constructed in Turkey to better understand high power transmission lines. In addition to these, the knowledge required for high power and high frequency applications has to be accumulated in Turkey for future projects. The key idea behind a circulator is to transmit power obtained from a PSU while minimizing the dissipated power and to absorb the reflected power at the RF dummy load (also known as RF dump). Hence, the reflected power will not damage the PSU. This goal is usually achieved using a circulator. It operates by applying a magnetic field to a ferrite material such as a calcium, vanadium doped garnet. Operating frequency, maximum power and scattering parameters are the essential specifications of a circulator.

The transmission part of the design consists of 6 basic elements; PSU, PSU to WG converter, waveguides, E and H Bends, 3−port circulator, and finally the WG to coaxial converter to transmit RF power to a pillbox RF cavity. For the purposes of this project, the WR1150 rectangular waveguide series have been chosen. The WR1150 series rectangular waveguides operate from 640 MHz up to 960 MHz and can carry a maximum power of about 35 MWs [29]. Considering the specifications of this series of rectangular waveguides, the design of the RF components was performed in CST MWS's Frequency Domain Solver [30] by fixing the operating frequency to 800 MHz to find the appropriate dimensions. The elements were produced by the local manufacturers in Istanbul, Turkey.

It is worth noting that a klystron operating at 800 MHz (YK 1190 from VALVO) and providing 58 kW continuous wave (CW) power was donated by CERN. The availability of this PSU drove the decision on the operating frequency. A reducer between the klystron output ($\phi = 3\ 1/8''$) and input of the transmission line (inner and outer

radius of a coaxial cable $\phi = 33.40$ mm and $\phi = 76.90$ mm / N-type reducer) has also been designed but not yet produced as of Summer 2018. The schematic view of the transmission line including the circulator can be seen in Figure 6.1.

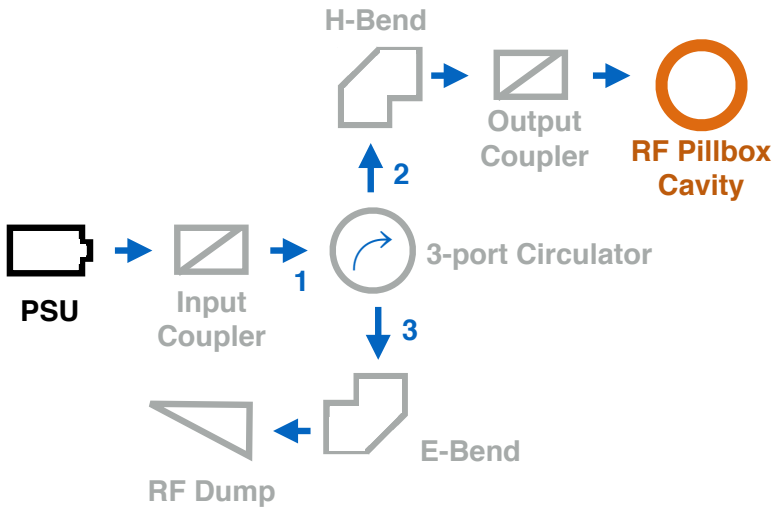

Figure 6.1. Schematic of the transmission line including the circulator.

6.1. Transmission Line Elements

The 90 degree E-bend is to be connected to the third port of the circulator at the side of the RF dump, whereas the H-bend is for the second port of the circulator at the side of the transmission line towards the accelerating cavity. The E and H bends are optimized to achieve better than -56 dB for their reflection characteristics assuming perfect electric conductor (PEC) as the body material. The waveguides (1 m and 1/2 m) together with the TEM-TE and TE-TEM converters, designed using CST MWS, were manufactured from aluminum (6000series). The RF dump was also made from aluminum using a triangularly ending waveguide loaded with silicon carbide (SiC) as the absorber material for reflecting power. As one of the main goals of the project is to gain the necessary know-how in designing and the construction of RF components, a second RF dump and another 1 m rectangular waveguide were made from iron sheets.

The electrical conductivity of iron, 9.93×10^6 S/m is less than that of aluminum, 37.7×10^6 S/m [6]. Because of this, the components made of aluminum give better transmission results. Moreover, metallic corrosion on the iron components, reduce their power transmission efficiency further, as the corrosion puts more dielectric constant into the medium inside the iron waveguide.

For the measurements of S-parameters, a VNA was used in the range of 780 MHz to 820 MHz with 501 sweep points and an IF bandwidth of 1 kHz was chosen. The frequency range was chosen to observe a sharper reflection values from the designed models when frequency shifts are taken into account. (The coaxial line and N-type connectors were chosen according to matched 50 Ω impedance.)

In the sections below, two types of measurements are described with several experimental setups in a slightly different manner. Whereas the experiments for the first type of measurements were done by adjusting tuners independently, the latter group were carried out by adjusting tuners (6.2) during the first measurement, which was done with the converters (TEM to TE and TE to TEM). The second group measurements were important to check the consistency of the simulation results with the measurement results of the elements because the results with decibel, the values of S-parameters are linearly related to each other.

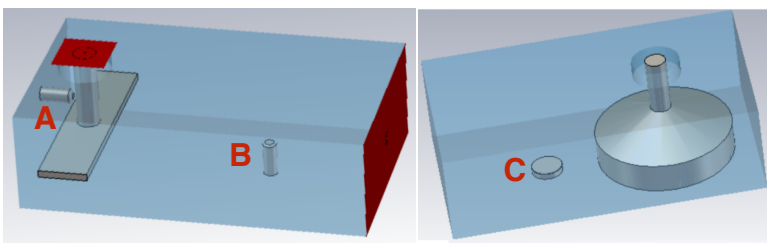

Figure 6.2. CST MWS drawings of the tuners inside the two converters labelled with A,B and C

6.1.1. Measurements With Tuners Adjusted Separately For Each Experiment

6.1.1.1. Experimental setup 1. The reducer was designed for converting the waveguide to N-type of connection (to get measurements from VNA). The efficiency of the one labelled with a star sign was measured in around −23 dB as seen in Figure 6.3(a) and the reflection value from the simulation was obtained as −83 dB.

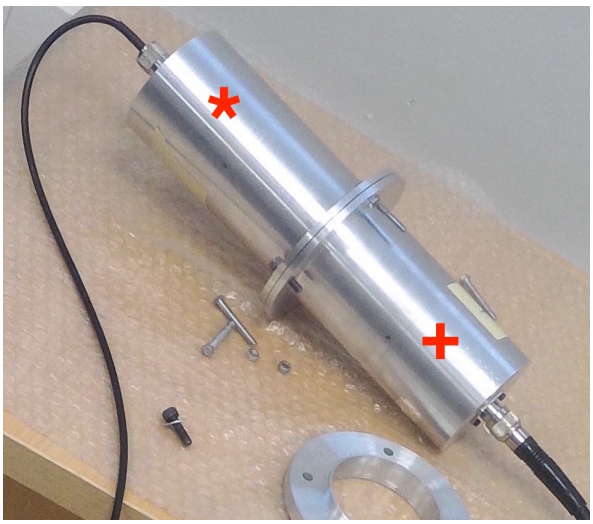

(a) Reducers - one labelled with a plus sign and the other with a star sign

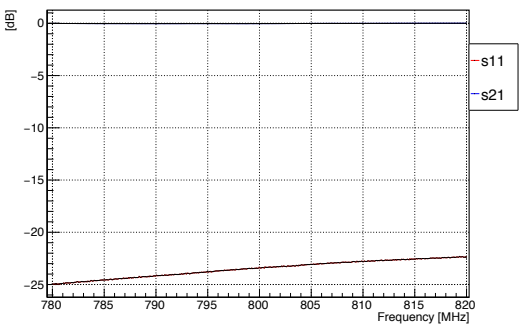

(b) Insertion and Reflection values of the reducer measurement

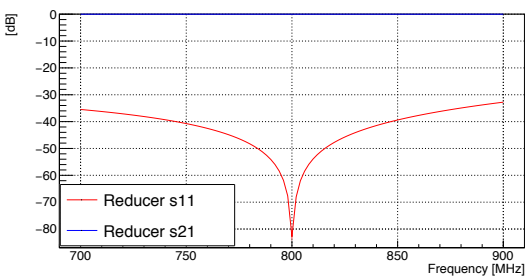

(c) Insertion and Reflection values of the reducer simulation

Figure 6.3. Photograph and the S-parameter plots for the setup with the reducers

6.1.1.2. Experimental setup 2. The 50 cm converter (TEM to TE) was connected to a 1 m waveguide towards the RF dump as seen in Figure 6.4(a). Before the manufacturing stage, the reflection values of the reducer and the TEM to TE converter had been optimized to −83 dB and −67 dB, respectively via CST MWS simulation program. During the measurement, a low power pulse, received from VNA, was eventually absorbed by the RF dump and the tuners, located at the converter, were adjusted to obtain the lowest reflection value from the setup. After tuning the (TEM to TE) converter at the operating frequency of 800 MHz, the obtained S11 value was around −50 dB (as shown in Figure 6.4(b)).

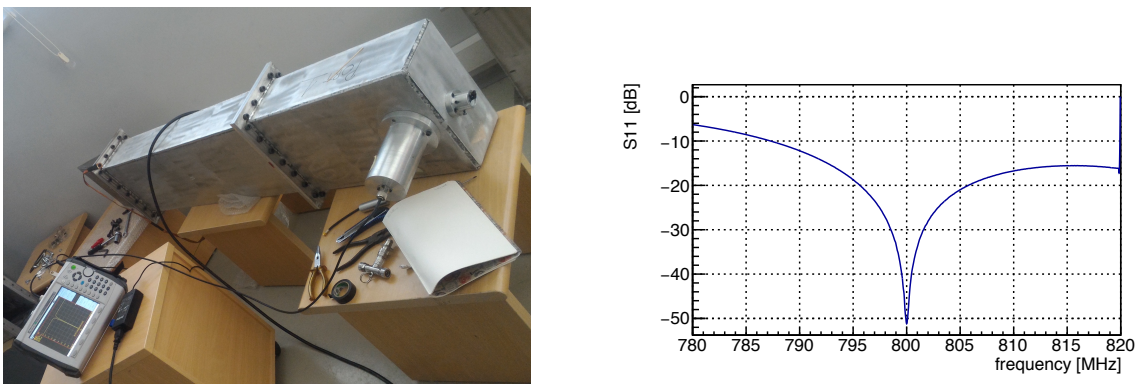

(a) Picture of the RF Dump setup

(b) The reflection value for the setup with RF Dump and TEM to TE converter

Figure 6.4. RF Dump setup with the reflection measurement results

6.1.1.3. Experimental setup 3. For the RF transmission line, the TE to TEM converter was also required and it was also designed by optimizing its S11 value as −56 dB with the computer simulations. For the efficiency of the TE to TEM converter, the setup (as shown in Figure 6.5(a)), which consists of the TEM to TE converter, the 1 m waveguide as well as the TE to TEM converter, was performed and the values of the S-parameters, S11, S12, S21, S22 were obtained as −36.1 dB, −0.06 dB, −0.07 dB and −52.7 dB, respectively by adjusting tuners' location inside the converters (Figure 6.6(a)). The same setup was rerun with the 1 m Al waveguide replaced by 1 m waveguide made from sheet metal and the results were found to be −48.9 dB, −0.14 dB, −0.14 dB and −42.8 dB, respectively (as shown in Figure 6.6(b)).

(a) The two converters with a 1 m WR1150 in between

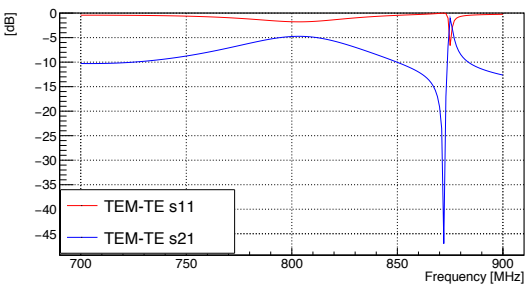

(b) The simulation results for the TEM to TE

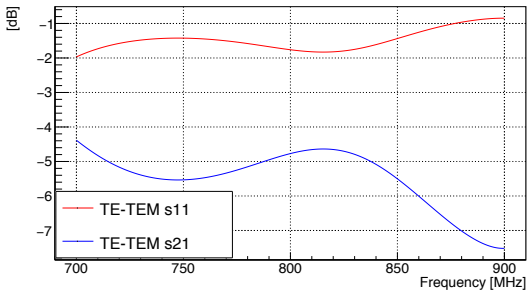

(c) The simulation results for the TE to TEM

Figure 6.5. Photograph and the S-parameter plots of the simulation result for the setup with two converters

6.1.1.4. Experimental setup 4. The E bend was required for the rotating part of the circulator through the RF dummy load. It was designed by optimizing its reflection value to be below −50 dB and its transmission value to be as close to zero dB as possible.

6.1.1.5. Experimental setup 5. H bend was required for the rotating part of the circulator through the accelerating cavity. This was designed asymmetrical and optimized to have its reflection value as below −50 dB and its transmission value to be as close to zero dB as possible. The asymmetry comes from the lengths of the shorts edges. One of them, labelled as A, is 98 mm and the other one, labelled as B, is 100 mm.

6.1.2. Measurements With Tuners Adjusted Only Once

For these measurements, the first experimental setup was put together and the most effective transmission value was obtained by adjusting the tuners. There after, the tuners were fixed using liquid silicone and all the remaining measurements were

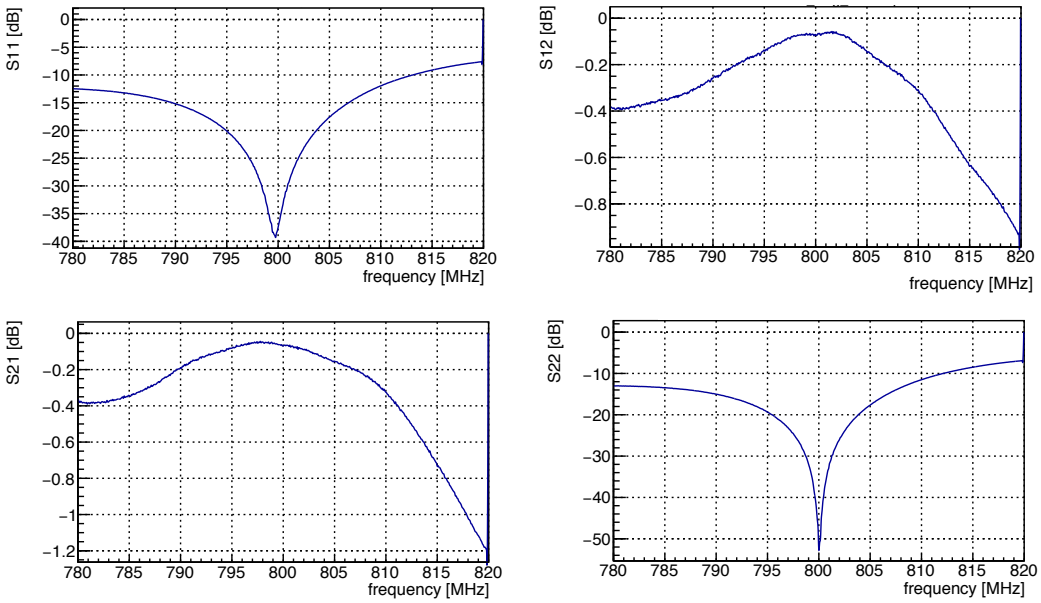

(a) Measured S-parameters for the two converters with 1m Aluminium WR1150 in between

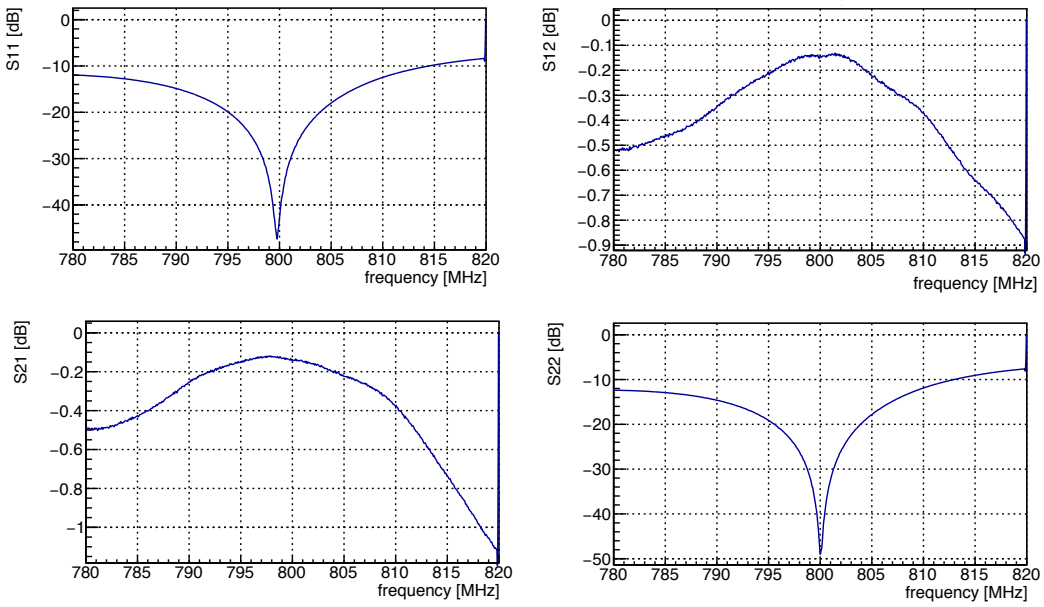

(b) Measured S-parameters for the two converters with metallic sheet WR1150 in between

Figure 6.6. The S-parameter plots of the measurement results for the setup with two converters

(a) The picture of the two converters with a 1 m WG and the E-bend

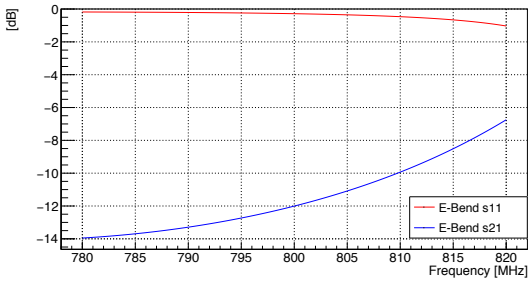

(b) Insertion and reflection values from the E-bend simulation

Figure 6.7. Photograph and the S-parameter plot of the simulation result for the setup with the two converters including a 1 m WG and the E-bend

performed with those fixed tuner positions.

6.1.2.1. Experimental setup 1. For adjusting the values of tuners, the TEM to TE converter was connected to the TE to TEM converter as shown in Figure 6.10. Once tuned, the values of S-parameters S11, S12, S21, S22 were measured to be −30.02 dB, −0.04 dB, −0.05 dB and −45.27 dB, respectively, at 800 MHz.

6.1.2.2. Experimental setup 2. This setup consisted of the TEM to TE converter, the TE to TEM converter and the E-bend as shown in Figure 6.11. The values of S-parameters S11, S12, S21, S22 were measured to be −18.10 dB, −0.09 dB, −0.13 dB and −22.71 dB, respectively, at 800 MHz.

6.1.2.3. Experimental setup 3. This setup consisted of the TEM to TE converter, the TE to TEM converter and the H-bend as shown in Figure 6.12. The values of S-parameters S11, S12, S21, S22 were measured to be −17.17 dB, −0.08 dB, −0.11 dB and −21.07 dB, respectively, at 800 MHz.

6.1.2.4. Experimental setup 4. This setup consisted of the TEM to TE converter, the TE to TEM converter and a 1 m waveguide as shown in Figure 6.13. The values of S-parameters S11, S12, S21, S22 were measured to be −29.45 dB, −0.09 dB, −0.08 dB and −27.41 dB, respectively, at 800 MHz.

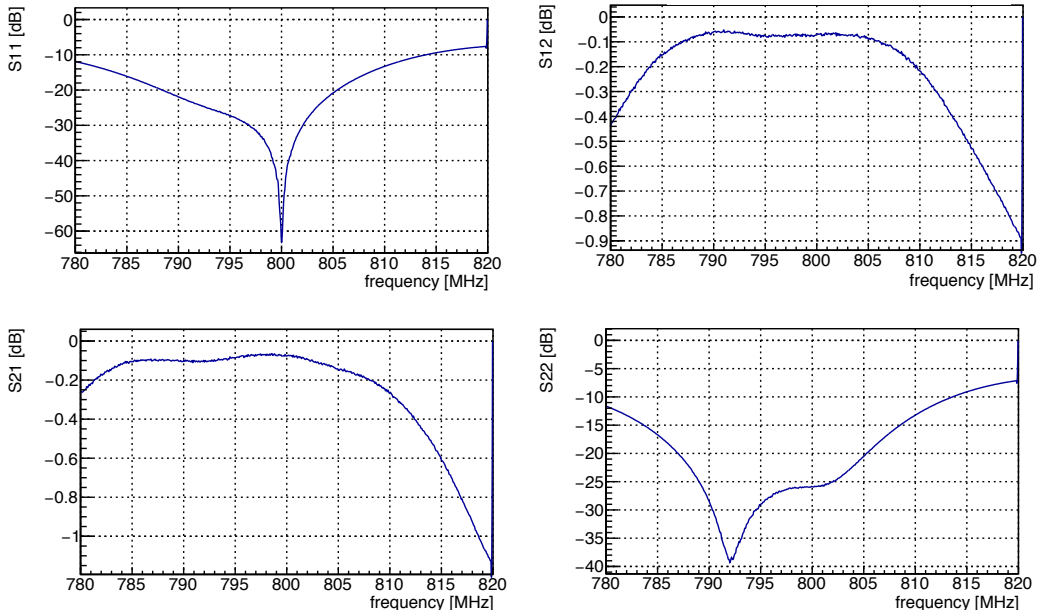

(a) The two converters with a 1 m WG and the E-bend

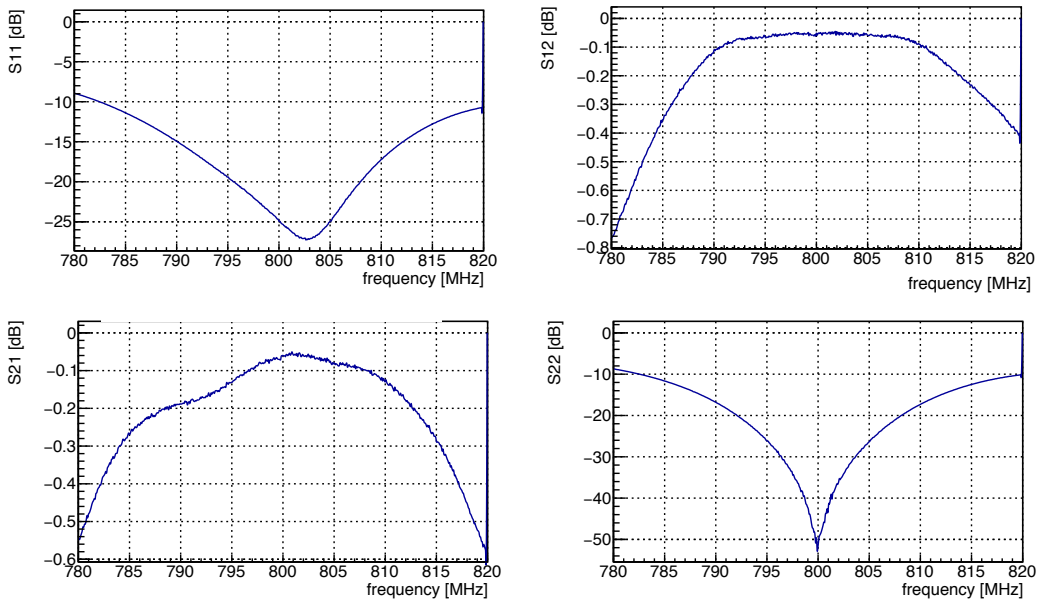

(b) The two converters with a 1 m WG and the E-bend, after the system was tuned by adjusting the tuner of the receiver

Figure 6.8. The S-parameter plots of the measurement results for the setup with the two converters including a 1 m WG and the E-bend

(a) The converters with H-bend

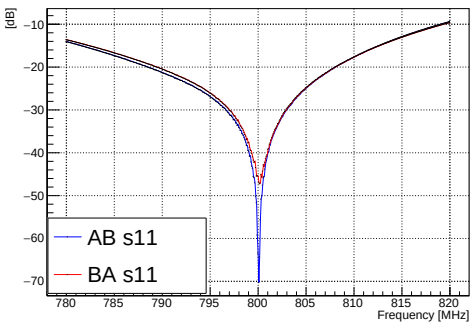

(b) Insertion and reflection values of the converters with H-bend measurement

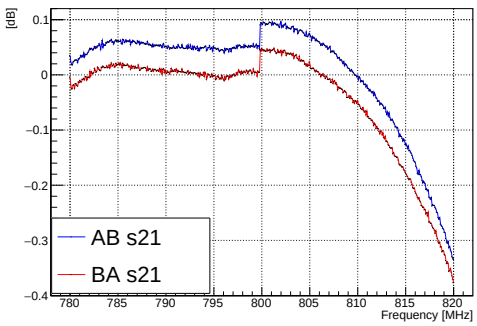

(c) Insertion and reflection values of the H-bend simulation

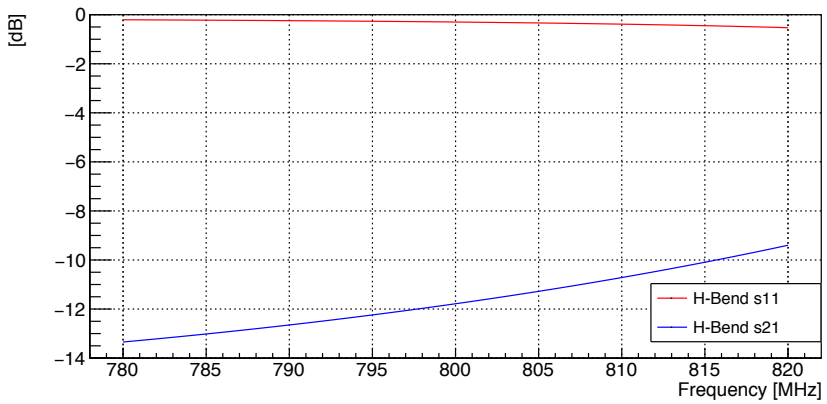

(d) Insertion and reflection values of the H-bend simulation

Figure 6.9. Photograph and the S-parameter plots for the setup with the two converters including the H-bend

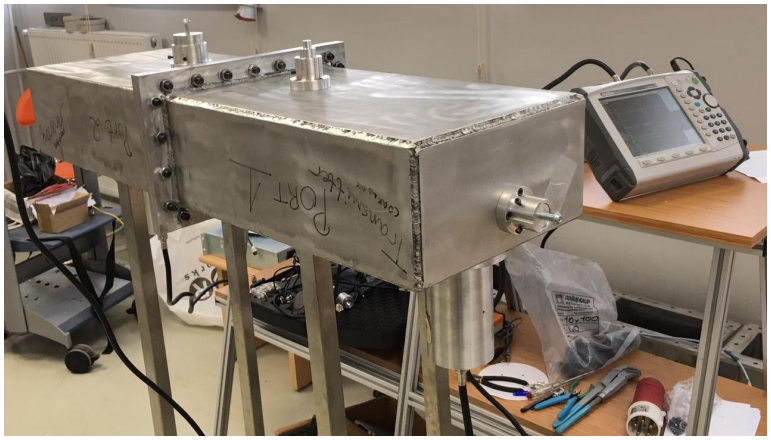

(a) Picture of the setup with the two converters.

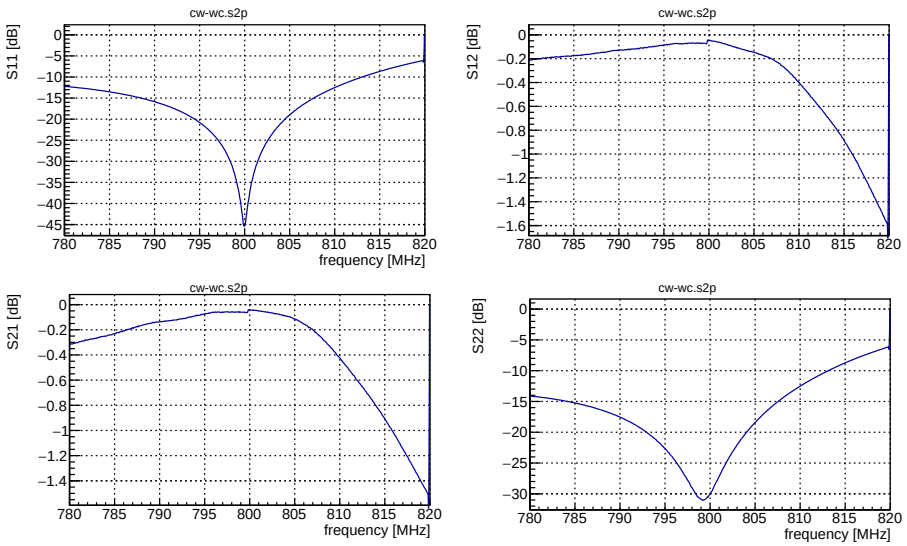

(b) The scattering parameters for the setup.

Figure 6.10. Photograph and the S-parameter plots for the setup with the two converters

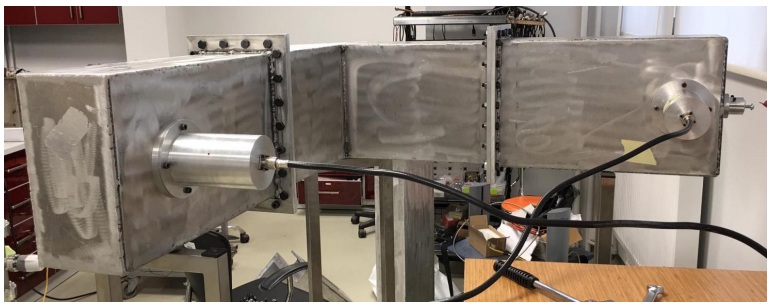

(a) Picture of the setup with the two converters including E-bend.

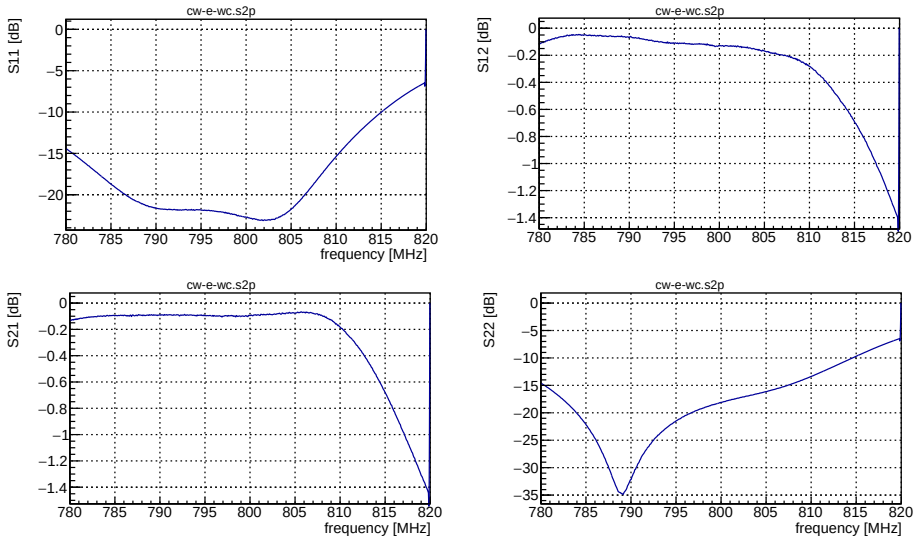

(b) The scattering parameters for the setup.

Figure 6.11. The picture and S-parameter values for the setup with the two converters including the E-bend, in between.

(a) Picture of the setup with the two converters including H-bend.

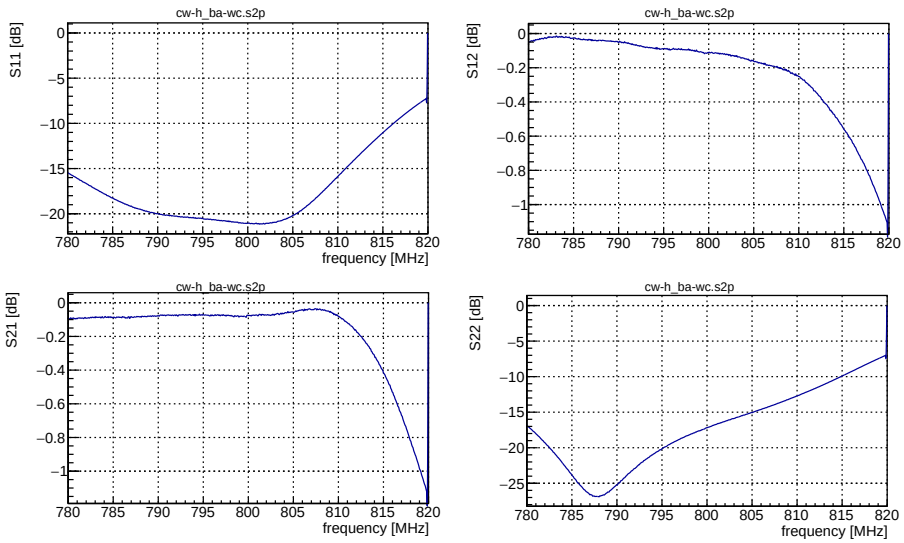

(b) The scattering parameters for the setup.

Figure 6.12. The picture and S-parameter values for the setup with the two converters including the H-bend, in between.

(a) Picture of the setup with the two converters including a 1 m waveguide.

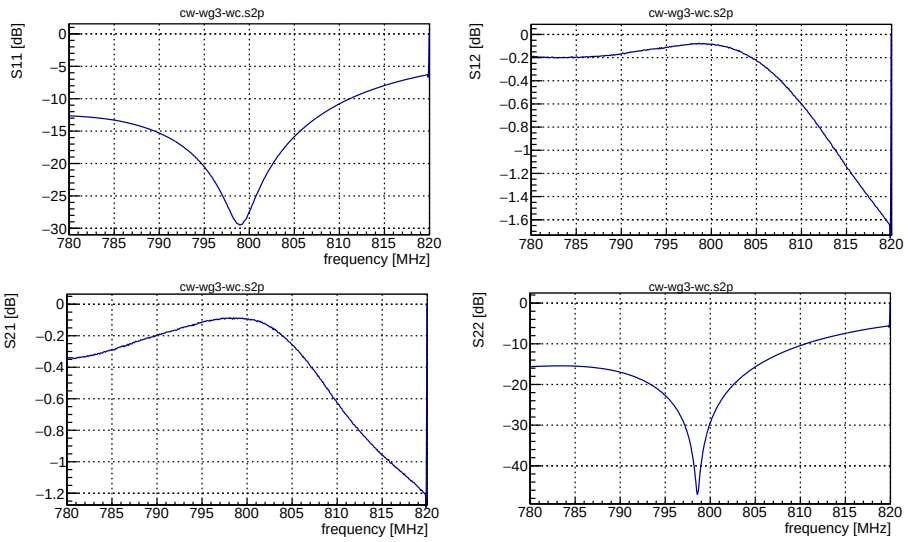

(b) The scattering parameters for the setup.

Figure 6.13. The picture and S-parameter values for the setup with the two converters including a 1 m waveguide.

6.1.2.5. Experimental setup 5. This setup consisted of the TEM to TE converter, the TE to TEM converter, a 1 m waveguide and the H-bend as shown in Figure 6.14(a). The values of S-parameters S11, S12, S21, S22 were measured to be −19.45 dB, −0.04 dB, −0.06 dB and −23.98 dB, respectively, at 800 MHz.

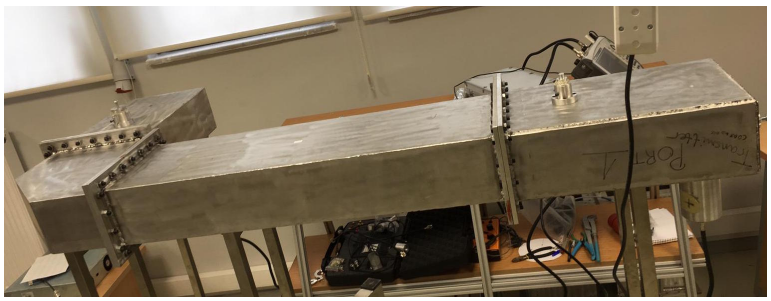

(a) Picture of the setup with the two converters including a 1 m waveguide and the H-bend.

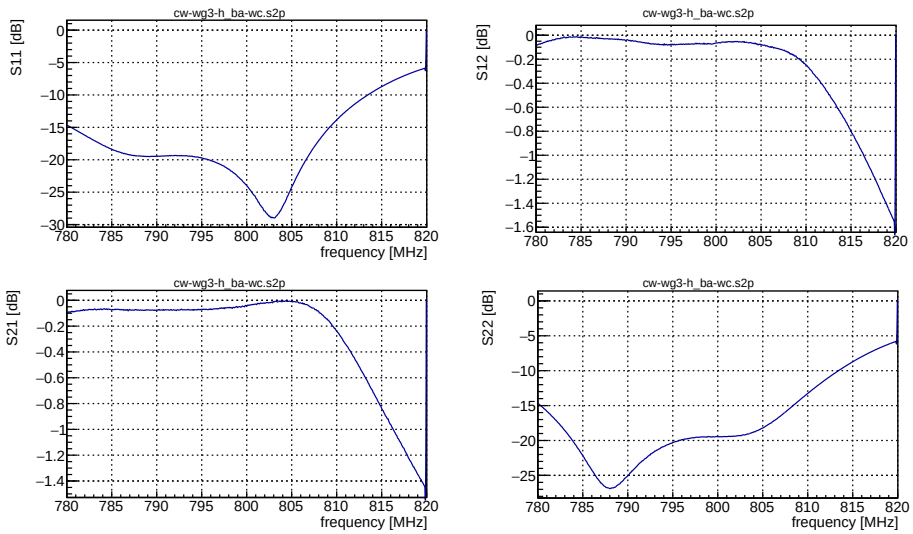

(b) The scattering parameters for the setup.

Figure 6.14. The picture and S-parameter values for the setup with the two converters including a 1 m waveguide and the H-bend, in between.

6.1.2.6. Experimental setup 6. This setup consisted of the TE to TEM converter, the E-bend and the RF dump as shown in Figure 6.15. The reflection value, S11 was measured to be −12.30 dB at 800 MHz in which this dB value is equal to 5.89 percentage of power transmission.

(a) Picture of the setup with the TE to TEM converter including the E-bend and the RF dump.

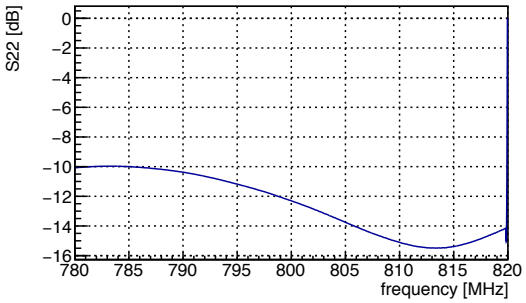

(b) The reflection value of the setup.

Figure 6.15. The picture and the reflection value for the setup with the TE to TEM converter including the E-bend and the RF dump

6.1.2.7. Experimental setup 7. This setup consisted of the TEM to TE converter, the E-bend and the RF dump as shown in Figure 6.16. The reflection value, S11 was measured to be −13.22 dB at 800 MHz in which this dB value is equal to 4.76 percentage of power transmission.

(a) Picture of the setup with the TEM to TE converter including the E-bend and the RF dump.

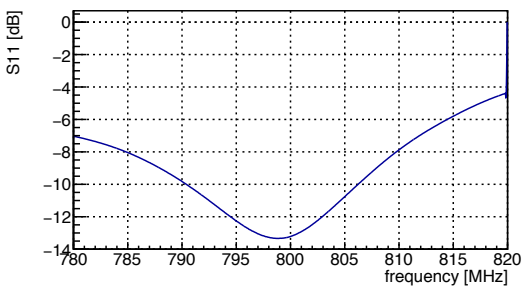

(b) The reflection value of the setup.

Figure 6.16. The picture and the reflection value for the setup with the TEM to TE converter including the E-bend and the RF dump

6.1.2.8. Experimental setup 8. This setup consisted of the TE to TEM converter and the RF dump as shown in Figure 6.17. The reflection value, S11 was measured to be −15.10 dB at 800 MHz in which this dB value is equal to 3.09 percentage of power transmission.

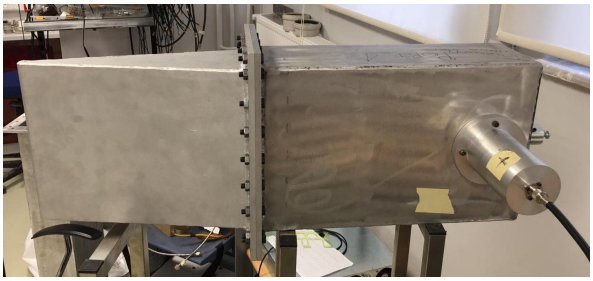

(a) Picture of the setup with the TE to TEM converter including the RF dump.

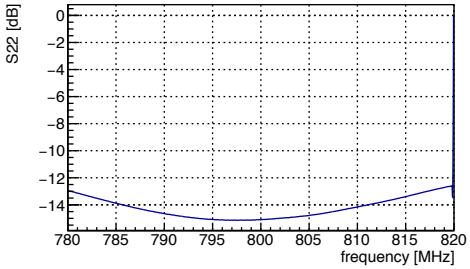

(b) The reflection value of the setup.

Figure 6.17. The picture and the reflection value for the setup with the TE to TEM converter including the RF dump

6.1.2.9. Experimental setup 9. This setup consisted of the TEM to TE converter and the RF dump as shown in Figure 6.18. The reflection value, S11 was measured to be −11.32 dB at 800 MHz in which this dB value is equal to 7.38 percentage of power transmission.

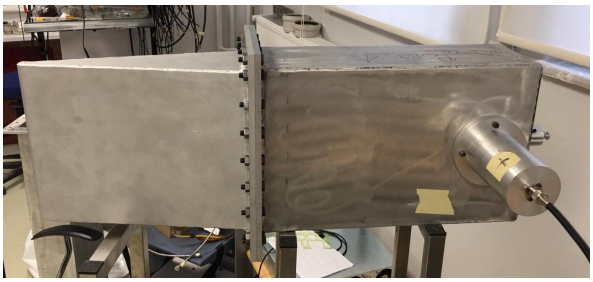

(a) Picture of the setup with the TEM to TE converter including and the RF dump.

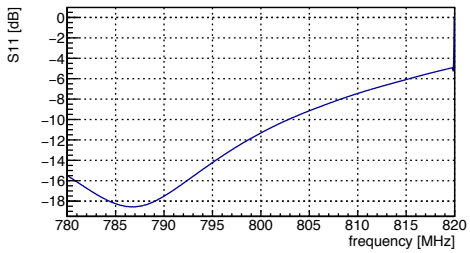

(b) The reflection value of the setup.

Figure 6.18. The picture and the reflection value for the setup with the TEM to TE converter including and the RF dump

6.1.2.10. Comparison between simulation and measurement results. As mentioned before, manipulation of the values in decibel is easier than large numbers. Computations in decibel are made linearly so Table 6.2 was constructed easily with the following steps. (To keep track of components easily, the transmission elements were labelled with some abbreviations as shown in Table 6.1.)

Table 6.1. Notation the transmission line elements

Elements	**Abbreviation**
Receiver (TE-TEM)	WC
Transmitter (TEM-TE)	CW
Waveguide (1m Long)	WG
E-Bend	E
H-Bend (A to B)	H_{AB}
H-Bend (B to A)	H_{BA}
RF Dump	C
Reducer plus	D_p
Reducer star	D_s
Waveguide (metal sheet)	WG_s

Table 6.2 shows that the S-parameter results in dB so that the transmission values of the elements can simply be calculated with linear algebra. For instance, the transmission value of the E-bend can be obtained by subtracting the insertion loss of 6.1.2.1 setup from the insertion loss of 6.1.2.2 setup. The insertion loss value of the E-bend is -0.08 dB which means that 98.2 percentage of the power coming from the system is transmitted. As in this example, this calculation can be done for all the other elements as well. It is worth noting that the S-parameter values have been measured by using the two converters to get the signal so their individual transmission values cannot be obtained with this method. As can be seen in Table 6.2, some level of loss is present in the constructed elements when compared to their simulation results. On the other hand, Experiment 6.1.2.3 and Experiment 6.1.2.5 are not self-consistent with respect to the level of loss due to the systematic errors coming from the sensitivity level of the VNA.

Table 6.2. Table of S-Parameters of the measurements according to the transmission line elements

Experiments : Elements	**S11** [dB]	**S12** [dB]	**S21** [dB]	**S22** [dB]	**Power Ratio**
6.1.1.1: $D_p + D_s$	**-22**	-	-	-	0.00630957
6.1.2.1: CW + WC	-30.02	-0.042	**-0.05**	-45.27	0.988553
6.1.2.2: CW + E + WC	-18.10	-0.09	**-0.13**	-22.71	0.97051
6.1.2.3: CW + H_{BA} + WC	-17.17	-0.08	**-0.11**	-21.07	0.97499
6.1.2.4: CW + WG + WC	-29.45	-0.09	**-0.08**	-27.41	0.981748
6.1.2.5: CW + WG + H_{AB} + WC	-19.66	-0.07	**-0.09**	-23.69	0.97949
6.1.2.5: CW + WG + H_{BA} + WC	-19.45	-0.04	**-0.06**	-23.98	0.986279
6.1.2.6: C + E + WC	**-12.30**	-	-	-	0.0467735
6.1.2.7: C + E + CW	**-13.22**	-	-	-	0.0476431
6.1.2.8: C + WC	**-15.10**	-	-	-	0.030903
6.1.2.9: C + CW	**-11.32**	-	-	-	0.0737904

7. CONCLUSION

In this thesis, we have reported on two projects using RF technology in accelerators. First, we have described work performed to study shields that are meant to eliminate the 1.3 GHz intrinsic resonance arising from the limits of the longitudinal beam coupling impedance. We have demonstrated that the developed methodology has allowed the identification of the status of the shields on the SPS-QF flanges via non-intrusive measurements. The effectiveness of the shields and the feasibility of the using coaxial ports on the BPHs to detect their presence inside the vacuum flanges have been studied with two measurement setups. In the first of these setups, a 1-port measurement of the reflections with a probe that is reaching directly into the flange has been shown to be a direct way of detecting the weak 1.3 GHz resonance. However such measurements are not possible in situ. With the second setup, a transmission measurement through the BPH ports was attempted. It was found that the such a method is not a viable way to identify the presence and status of the shields at 1.3 GHz. Nonetheless we have showed that this resonance can be inferred from 2-port measurements at higher frequencies, for example at 3.7 GHz.

After demonstrating this methodology at 3.7 GHz, 70 of the BPHs in the SPS tunnel were examined in order to categorize them as shielded, unshielded or shielded-but-poorly-contacted. 42 of these were found to be in a good agreement with the installation records. The 19 amongst remaining 28 were flagged as needing further investigation during the SPS upgrade period in the LS2, in 2019-2020. Another 5 of the unshielded BPHs could not be categorized properly due to some variations in the data set taken from the tunnel. Finally, 4 BPHs were identified as needing further attention at the earliest time as possible [28].

In the second project, the long-term aim is to obtain know-how on accelerator construction in Turkey, with various specific subtopics such as designing of various RF transmission components, circulators, converters, cavities as well as their measurements after commissioning. Towards this aim, the design of an RF transmission line and a

circulator operating at a frequency of 800 MHz was carried out with local resources. The EM-simulations of this design have been performed. These simulations have been tested against some benchmark measurements after manufacturing. These include S-parameters of the constructed components which allow us to assess the efficiency of the RF power system as a whole.

In conclusion, simulations and measurements on RF signal and power transmission have been carried out successfully. The obtained know-how and the techniques developed are critical for the development and/or improvements of the accelerators for both projects.

REFERENCES

1. TIARA, *Types of accelerators*, 2014, http://www.accelerators-for-society.org, accessed at September 2018.

2. Mobs, E., *The CERN accelerator complex. Complexe des accélérateurs du CERN*, Jul 2016, https://cds.cern.ch/record/2197559, General Photo.

3. Damerau, H., A. Funken, R. Garoby, S. Gilardoni, B. Goddard, K. Hanke, A. Lombardi, D. Manglunki, M. Meddahi, B. Mikulec, G. Rumolo, E. Shaposhnikova, M. Vretenar and J. Coupard, *LHC Injectors Upgrade, Technical Design Report, Vol. I: Protons*, Tech. rep., Dec 2014, https://cds.cern.ch/record/1976692, CERN-ACC-2014-0337.

4. Munda, N., *Pumping port shielding - BHP/QF bellow s/ass*, 2000, http://edms-service.web.cern.ch/edms-service/cdd/, designed by N. Munda and accessed from CERN Drawing Directory.

5. Wolfram—Alpha, *WolframAlpha Zeros of the Bessel Function*, 2009, http://mathworld.wolfram.com/BesselFunctionZeros.html, accessed at June 2018.

6. Balance, *Conductivity and Resistivity in Metals*, 2017, https://www.thebalance.com/electrical-conductivity-in-metals-2340117, accessed at September 2018.

7. Bailey, R., *An Application for Research: the Large Hadron Collider*, Apr 2014, https://cds.cern.ch/record/1693333.

8. Bohl, T., T. P. R. Linnecar and E. Shaposhnikova, *Measuring the Resonance Structure of Accelerator Impedance with Single Bunches*, Vol. 78, Sep 1996, https://cds.cern.ch/record/311683, CERN-SL-96-062-RF.

9. Shaposhnikova, E., T. Bohl and T. P. R. Linnecar, *Results from the impedance reduction in the CERN SPS*, Vol. 642, 2002, https://cds.cern.ch/record/610244.

10. Campelo, J. E., T. Argyropoulos, T. Bohl, F. Caspers, J. Esteban Müller, J. Ghini, A. Lasheen, D. Quartullo, B. Salvant, E. Shaposhnikova and C. Zannini, *An Extended SPS Longitudinal Impedance Model*, 2015, https://cds.cern.ch/record/2141767.

11. Kaltenbacher, T. and C. Vollinger, *Characterization of Shielding for the CERN-SPS Vacuum Flanges With Respect to Beam Coupling Impedance*, 2017, https://cds.cern.ch/record/2289721, CERN-ACC-2017-108.

12. Kaltenbacher, T., F. Caspers and C. Vollinger, *Machine element contribution to the longitudinal impedance model of the CERN SPS*, 2016, https://cds.cern.ch/record/2304640.

13. Zotter, B. W. and S. A. Kheifets, *Impedances and wakes in high-energy particle accelerators*, World Scientific, 1998, https://cds.cern.ch/record/366784.

14. Pozar, D. M., *Microwave engineering; 4th ed.*, Wiley, 2012, https://cds.cern.ch/record/1432911.

15. Balanis, C. A., *Advanced engineering electromagnetics; 2nd ed.*, John Wiley - Sons, 2012, https://cds.cern.ch/record/1511890, The book can be consulted by contacting: TE-MSC: Farantatos, Panagiotis.

16. Palumbo, L. and V. G. Vaccaro, *Wake fields measurements*, May 1989, https://cds.cern.ch/record/202581, LNF-89-035-P.

17. Palumbo, L., V. G. Vaccaro and M. Zobov, *Wake fields and impedance*, Sep 1994, https://cds.cern.ch/record/276437, LNF-94-041-P.

18. Day, H. A., *Measurements and Simulations of Impedance Reduction Techniques in Particle Accelerators*, Ph.D. Thesis, 2013.

19. Stupakov, G. V., *Wake and impedance*, July 2000, JAS 2000 - High quality beams. Proceedings, Joint US-CERN-Japan-Russia Accelerator School, St. Petersburg and Moscow, Russia AIP Conf. Proc.592.

20. Ferrario, M., M. Migliorati and L. Palumbo, *Wakefields and Instabilities in Linear Accelerators*, Jan 2016, `https://cds.cern.ch/record/1982427`, 19 pages, contribution to the CAS 2013 - CERN Accelerator School: Advanced Accelerator Physics Course, Trondheim, Norway.

21. Herr, W., *Intensity Limitations in Particle Beams*, CERN, 2017, `https://cds.cern.ch/record/2276820`.

22. Zannini, C., L. Rivkin and G. Rumolo, *Electromagnetic Simulation of CERN accelerator Components and Experimental Applications*, Ph.D. Thesis, Mar 2013, `https://cds.cern.ch/record/1561199`, Presented 15 Apr 2013.

23. Bray, J. R. and L. Roy, *Measuring the unloaded, loaded, and external quality factors of one- and two-port resonators using scattering-parameter magnitudes at fractional power levels*, Vol. 151, August 2004.

24. Rohde and Schwarz, *dB or not dB? Everything you ever wanted to know about decibels but were afraid to ask*, 2005.

25. Kurokawa, K., *Power Waves and the Scattering Matrix*, Vol. 13, 1965.

26. Collier, P., M. Ainoux, R. Guinand, J. M. Jiménez, A. Rizzo, A. Spinks and K. Weiss, *Reducing the SPS Machine Impedance*, Jun 2002, `https://cds.cern.ch/record/565833`, CERN-SL-2002-026-MR.

27. Forck, P., *Lecture notes on beam instrumentation and diagnostics: Joint University*

Accelerator School, January - March 2011, CreateSpace, North Charleston, SC, 2015, https://cds.cern.ch/record/2000265.

28. Farricker, A., P. Kramer, B. Popovic, E. Sunar, C. Vollinger and M. Wendt, *Identification of Imperfections in Impedance Shields on the SPS-QF Flanges via Non-Intrusive Measurements*, 2018, Proceedings, 9th International Particle Accelerator Conference (IPAC 2018): Vancouver, BC Canada.

29. Solutions, M. R., *Coaxial Components*, 1997, https://www.megaind.com, accessed at June 2018.

30. CST, *Computer Simulation Technology - Microwave Studio*, 2016, https://www.cst.com/products/cstmws, accessed at June 2018.

31. SPM Laboratory Research, *Cylindrical Waveguide*, 2004, https://www.nhn.ou.edu/ johnson/Education/Juniorlab/Microwave, accessed at June 2018.

APPENDIX A: TUNNEL MEASUREMENT RESULTS

Table A.1. Summary of the results of the measurements done at the SPS tunnel measurement

BPH Name	Expected	Measured	BPH Name	Expected	Measured
BPH10208	Shielded	Shielded	BPH41408	Shielded	Poor Contact
BPH10408	Shielded	Shielded	BPH41608	Shielded	Poor Contact
BPH10608	Shielded	Poor Contact	BPH42208	Shielded	Shielded
BPH10808	Unshielded	Not Shielded	BPH42408	Shielded	Not Shielded
BPH11008	Shielded	Shielded	BPH42608	Shielded	Poor Contact
BPH11208	Shielded	Shielded	BPH42808	Shielded	Shielded
BPH22608	Unshielded	Bad Trace	BPH43008	Shielded	Shielded
BPH22808	Shielded	Poor Contact	BPH43208	Shielded	Shielded
BPH23008	Shielded	Shielded	BPH43408	Shielded	Poor Contact
BPH23208	Shielded	Shielded	BPH43608	Shielded	Poor Contact
BPH23408	Shielded	Shielded	BPH50208	Shielded	Poor Contact
BPH23608	Unshielded	Not Shielded	BPH50408	Unshielded	Not Shielded
BPH30208	Shielded	Shielded	BPH50608	Shielded	Poor Contact
BPH30408	Shielded	Shielded	BPH50808	Unshielded	Not Shielded
BPH30608	Shielded	Not Shielded	BPH51208	Shielded	Poor Contact
BPH30808	Unshielded	Not Shielded	BPH51808	Unshielded	Misidentified
BPH31008	Shielded	Shielded	BPH52008	Unshielded	Not Shielded
BPH31208	Unshielded	Misidentified	BPH52208	Unshielded	Not Shielded
BPH31408	Shielded	Not Shielded	BPH52608	Unshielded	Bad Trace
BPH31608	Unshielded	Misidentified	BPH60208	Shielded	Shielded
BPH31808	Unshielded	Misidentified	BPH60408	Shielded	Shielded
BPH32008	Unshielded	Not Shielded	BPH60608	Shielded	Shielded
BPH32208	Unshielded	Not Shielded	BPH60808	Unshielded	Bad Trace
BPH32608	Unshielded	Not Shielded	BPH61008	Unshielded	Bad Trace
BPH32808	Shielded	Poor Contact	BPH61208	Shielded	Not Shielded
BPH33008	Shielded	Shielded	BPH61408	Shielded	Shielded
BPH33208	Shielded	Shielded	BPH61608	Unshielded	Bad Trace
BPH33408	Unshielded	Not Shielded	BPH62208	Unshielded	Not Shielded
BPH33608	Shielded	Shielded	BPH62408	Shielded	Poor Contact
BPH40208	Shielded	Poor Contact	BPH62608	Unshielded	Not Shielded
BPH40408	Shielded	Poor Contact	BPH62808	Shielded	Shielded
BPH40608	Shielded	Shielded	BPH63008	Shielded	Shielded
BPH40808	Unshielded	Not Shielded	BPH63208	Shielded	Shielded
BPH41008	Shielded	Poor Contact	BPH63408	Shielded	Shielded
BPH41208	Shielded	Shielded	BPH63608	Shielded	Shielded

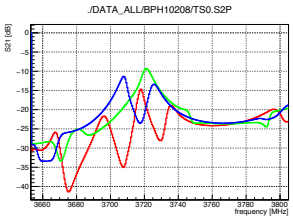

(a) BPH10208

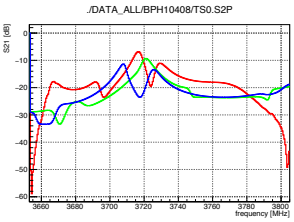

(b) BPH10408

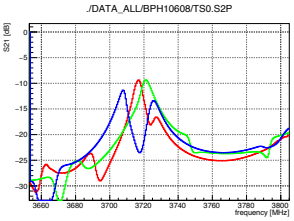

(c) BPH10608

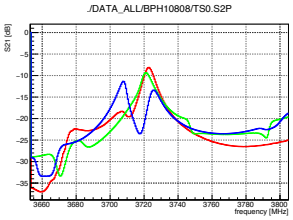

(d) BPH10808

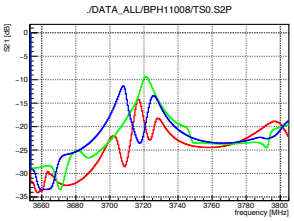

(e) BPH11008

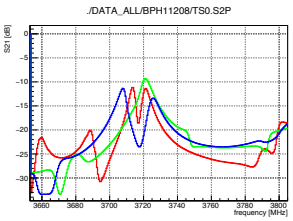

(f) BPH11208

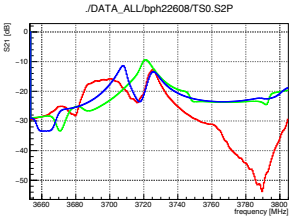

(g) BPH22608

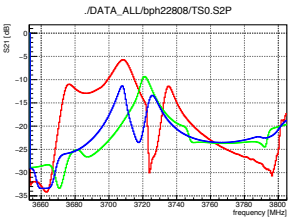

(h) BPH22808

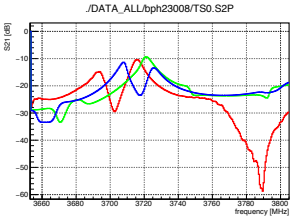

(i) BPH23008

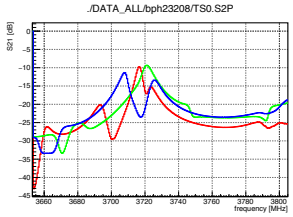

(j) BPH23208

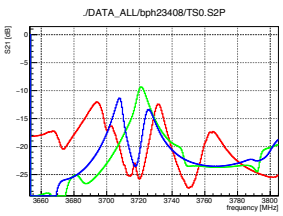

(k) BPH23408

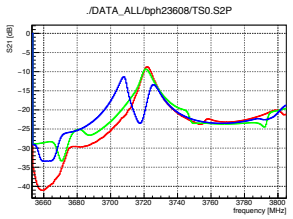

(l) BPH23608

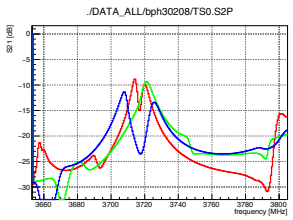

(m) BPH30208

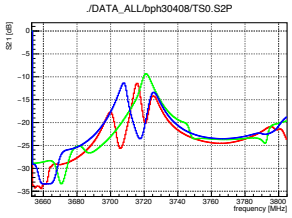

(n) BPH30408

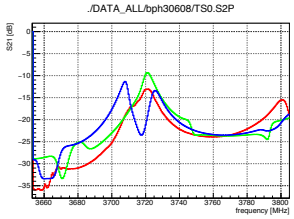

(o) BPH30608

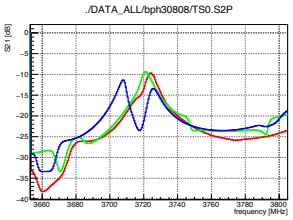

(p) BPH30808

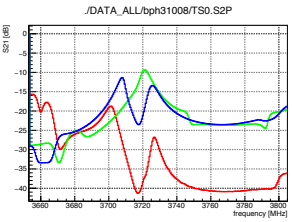

(q) BPH31008

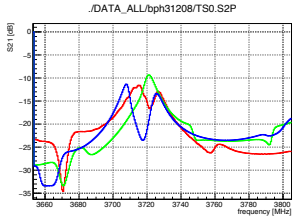

(r) BPH31208

Figure A.1. The result plots of the measurements done at the SPS tunnel

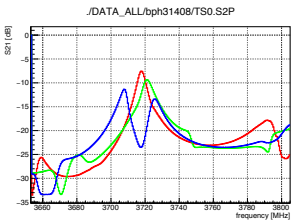

(a) BPH31408

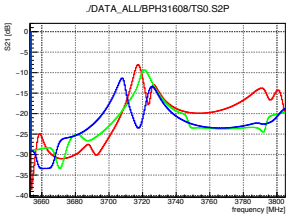

(b) BPH31608

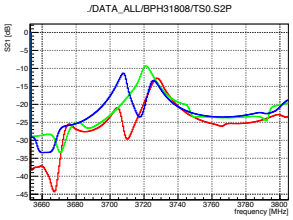

(c) BPH31808

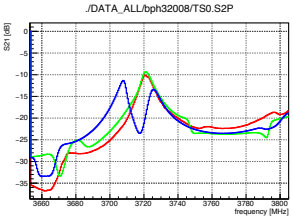

(d) BPH32008

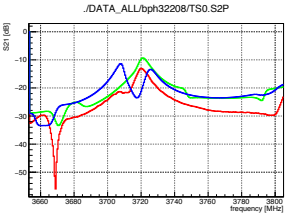

(e) BPH32208

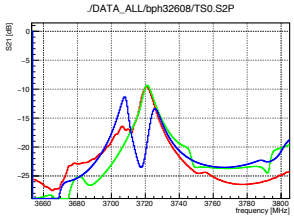

(f) BPH32608

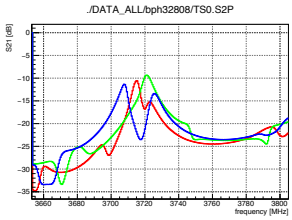

(g) BPH32808

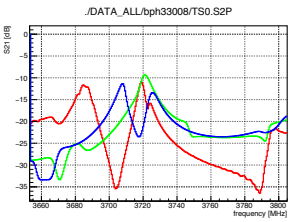

(h) BPH33008

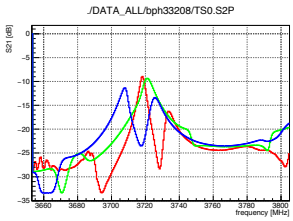

(i) BPH33208

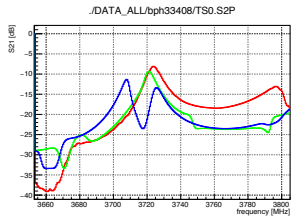

(j) BPH33408

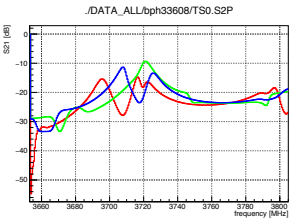

(k) BPH33608

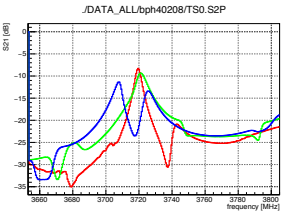

(l) BPH40208

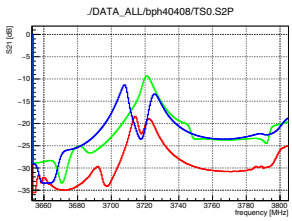

(m) BPH40408

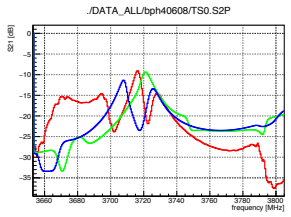

(n) BPH40608

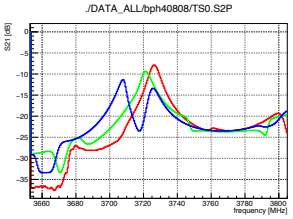

(o) BPH40808

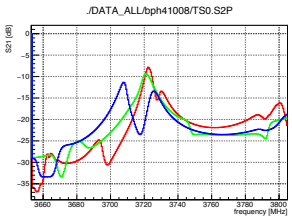

(p) BPH41008

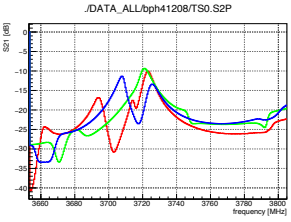

(q) BPH41208

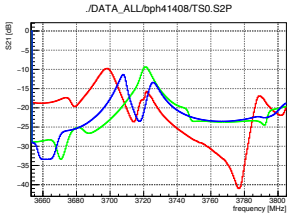

(r) BPH41408

Figure A.2. Continued to the result plots of the measurements done at the SPS tunnel

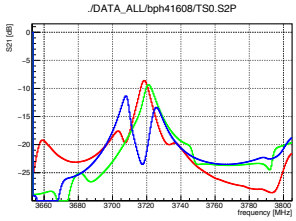

(a) BPH41608

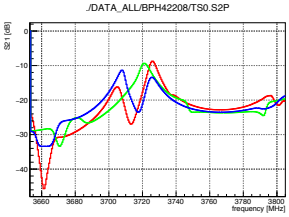

(b) BPH42208

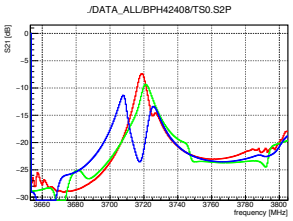

(c) BPH42408

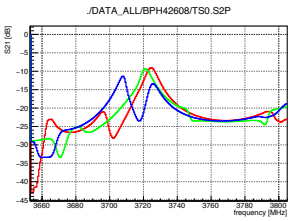

(d) BPH42608

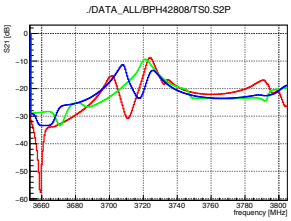

(e) BPH42808

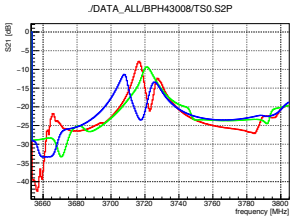

(f) BPH43008

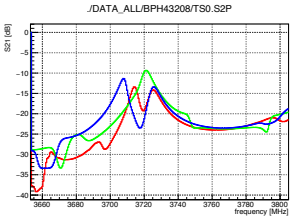

(g) BPH43208

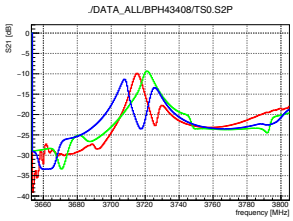

(h) BPH43408

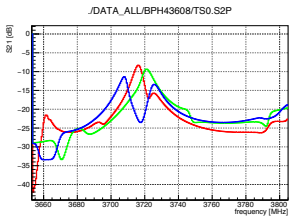

(i) BPH43608

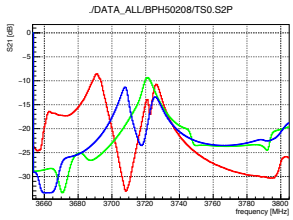

(j) BPH50208

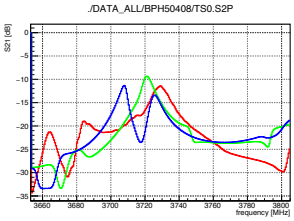

(k) BPH50408

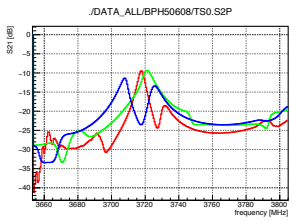

(l) BPH50608

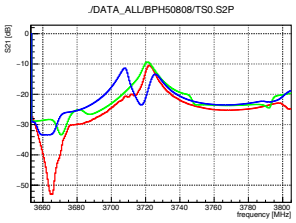

(m) BPH50808

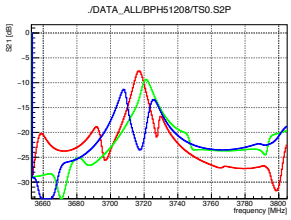

(n) BPH51208

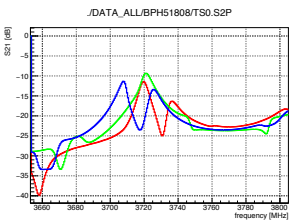

(o) BPH51808

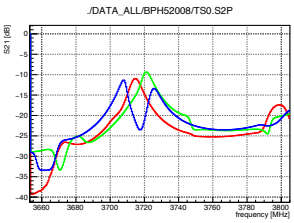

(p) BPH52008

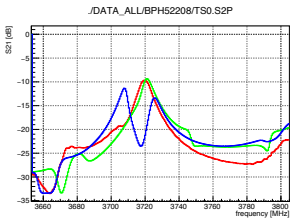

(q) BPH52208

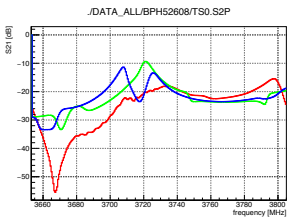

(r) BPH52608

Figure A.3. Continued to the result plots of the measurements done at the SPS tunnel

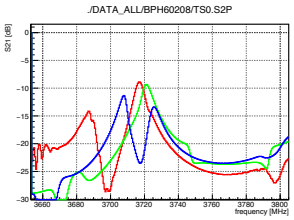

(a) BPH60208

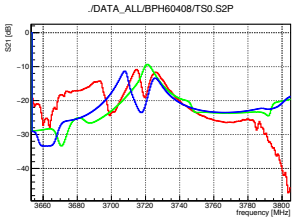

(b) BPH60408

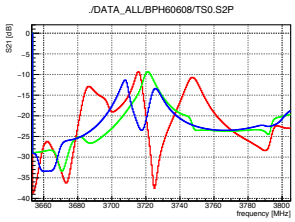

(c) BPH60608

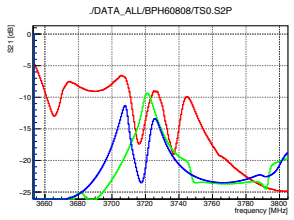

(d) BPH60808

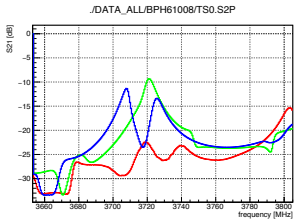

(e) BPH61008

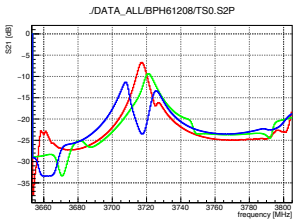

(f) BPH61208

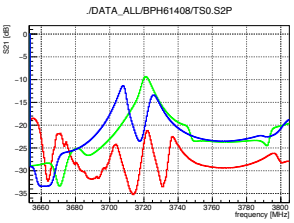

(g) BPH61408

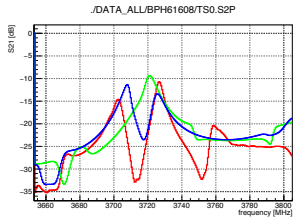

(h) BPH61608

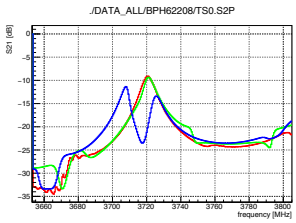

(i) BPH62208

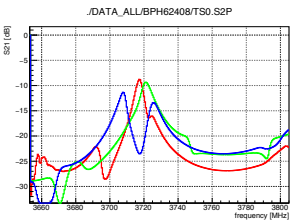

(j) BPH62408

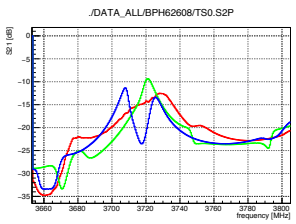

(k) BPH62608

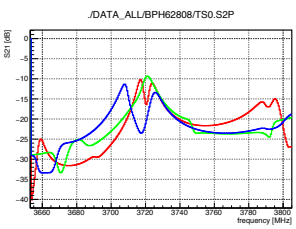

(l) BPH62808

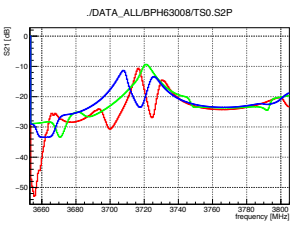

(m) BPH63008

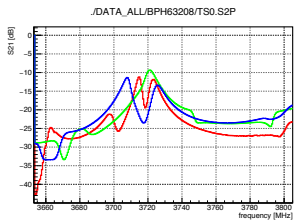

(n) BPH63208

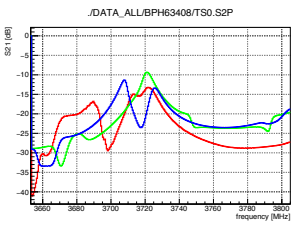

(o) BPH63408

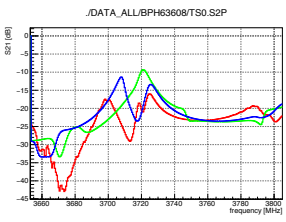

(p) BPH63608

Figure A.4. Continued to the result plots of the measurements done at the SPS tunnel

APPENDIX B: ELECTRICAL CONDUCTIVITY

Table B.1. Conductivity of some common materials, in units of mho/m [6]

Material	**Electrical conductivity [mho/m]**
Aluminum	$37.7\ 10^6$
Beryllium	$31.3\ 10^6$
Cadmium	$13.8\ 10^6$
Calcium	$29.8\ 10^6$
Chromium	$7.74\ 10^6$
Cobalt	$17.2\ 10^6$
Copper	$59.6\ 10^6$
Copper (annealed)	$58.0\ 10^6$
Gold	$45.2\ 10^6$
Iron	$9.93\ 10^6$
Nickel	$14.3\ 10^6$
Niobium	$6.93\ 10^6$
Silver	$63\ 10^6$
Stainless Steel	$1\ 10^6$
Tantalum	$7.61\ 10^6$
Thorium	$6.53\ 10^6$
Tin	$9.17\ 10^6$
Tungsten	$18.9\ 10^6$
Zinc	$16.6\ 10^6$

APPENDIX C: WAVE EQUATION & TE-MODE FOR CYLINDRICAL WG

Assume that there is a cylindrical waveguide as shown in Figure 2.2. The structure is filled with the material of permittivity μ and permeability ε.

The below forms written in cylindrical coordinates can be possible solutions for Maxwell equations:

$$\vec{E}(\rho,\phi,z,t) = \vec{E_0}(\rho,\phi)e^{i(wt-kz)} \quad , \tag{C.1}$$

$$\vec{B}(\rho,\phi,z,t) = \vec{B_0}(\rho,\phi)e^{i(wt-kz)} \quad . \tag{C.2}$$

For TE mode, when the magnetic field solution, $\vec{B}(\rho,\phi,z,t)$ is inserted in the wave equation (Equation 2.3), given form can be written as:

$$\nabla^2\vec{B}(\rho,\phi,z,t) - \frac{1}{c^2}\frac{\partial^2}{\partial t^2}\vec{B}(\rho,\phi,z,t) = 0 \quad , \tag{C.3}$$

$$\nabla^2\vec{B_0}(\rho,\phi)e^{i(wt-kz)} - \frac{1}{c^2}\frac{\partial^2}{\partial t^2}\vec{B_0}(\rho,\phi)e^{i(wt-kz)} = 0 \quad , \tag{C.4}$$

$$\Big(\nabla_\perp^2 + \nabla_z^2\Big)\vec{B_0}(\rho,\phi)e^{i(wt-kz)} - \frac{(iw)^2}{c^2}\vec{B_0}(\rho,\phi)e^{i(wt-kz)} = 0 \quad , \tag{C.5}$$

$$\Big(\nabla_\perp^2 + (-ik)^2\Big)\vec{B_0}(\rho,\phi)e^{i(wt-kz)} + \frac{w^2}{c^2}\vec{B_0}(\rho,\phi)e^{i(wt-kz)} = 0 \quad , \tag{C.6}$$

$$\Big(\nabla_\perp^2 - k^2\Big)\vec{B_0}(\rho,\phi)e^{i(wt-kz)} + \frac{w^2}{c^2}\vec{B_0}(\rho,\phi)e^{i(wt-kz)} = 0 \quad , \tag{C.7}$$

$$\Big(\nabla_\perp^2 - k^2 + \frac{w^2}{c^2}\Big)\vec{B_0}(\rho,\phi)e^{i(wt-kz)} = 0 \quad , \tag{C.8}$$

$$\Big(\nabla_\perp^2 - k_c^2\Big)\vec{B_0}(\rho,\phi)e^{i(wt-kz)} = 0 \quad . \tag{C.9}$$

where $\nabla_\perp^2 = \frac{1}{\rho}\frac{\partial}{\partial\rho}\Big(\rho\frac{\partial}{\partial\rho}\Big) + \frac{1}{\rho^2}\frac{\partial^2}{\partial\phi^2}$ is the Laplace operator in transverse Cylindrical coordinates, k is the propagation coefficient and $k_c^2 = \frac{w^2}{c^2} - k^2$, where k_c is the cutoff wave number of the waveguide. By using the separation of variables, the transverse

component of the magnetic field equation is written as:

$$B_0(\rho,\phi) = R(\rho)\Phi(\phi) \tag{C.10}$$

By inserting $B_0(\rho,\phi)$ to the above simplified wave equation, the magnetic field function can be solved:

$$\begin{aligned}
\frac{1}{\rho}\frac{\partial}{\partial\rho}\Big(\rho\frac{\partial}{\partial\rho}R\Phi\Big) + \frac{1}{\rho^2}\frac{\partial^2 R\Phi}{\partial\phi^2} + k_c^2 R\Phi &= 0 \quad , &\text{(C.11)}\\
\frac{\Phi}{\rho}\frac{\partial}{\partial\rho}\Big(\rho\frac{\partial R}{\partial\rho}\Big) + \frac{R}{\rho^2}\frac{\partial^2\Phi}{\partial\phi^2} + k_c^2 R\Phi &= 0 \quad , &\text{(C.12)}\\
\frac{\Phi}{\rho}\Big(\frac{\partial R}{\partial\rho} + \rho\frac{\partial^2 R}{\partial\rho^2}\Big) + \frac{R}{\rho^2}\frac{\partial^2\Phi}{\partial\phi^2} + k_c^2 R\Phi &= 0 \quad . &\text{(C.13)}
\end{aligned}$$

Multiplying by ρ^2 and dividing $R\Phi$ both sides of the equation, it becomes as:

$$\begin{aligned}
\frac{\rho^2}{R\Phi}\frac{\Phi}{\rho}\Big(\frac{\partial R}{\partial\rho} + \rho\frac{\partial^2 R}{\partial\rho^2}\Big) + \frac{\rho^2}{R\Phi}\frac{R}{\rho^2}\frac{\partial^2\Phi}{\partial\phi^2} + \frac{\rho^2}{R\Phi}k_c^2 R\Phi &= 0 \quad , &\text{(C.14)}\\
\frac{\rho}{R}\frac{\partial R}{\partial\rho} + \frac{\rho^2}{R}\frac{\partial^2 R}{\partial\rho^2} + \frac{1}{\Phi}\frac{\partial^2\Phi}{\partial\phi^2} + \rho^2 k_c^2 &= 0 \quad . &\text{(C.15)}
\end{aligned}$$

If this equation regulates with respect to the variables and uses simpler notation at the derivations, it can be written as:

$$\frac{\rho^2}{R}\ddot{R} + \frac{\rho}{R}\dot{R} + k_c^2\rho^2 + \frac{1}{\Phi}\ddot{\Phi} = 0 \quad . \tag{C.16}$$

Now, this equation can be separated to two terms and each term can be equal to a constant, l^2 :

$$\begin{aligned}
\frac{\rho^2}{R}\ddot{R} + \frac{\rho}{R}\dot{R} + k_c^2\rho^2 &= l^2 \quad , &\text{(C.17)}\\
\frac{1}{\Phi}\ddot{\Phi} &= -l^2 \quad , &\text{(C.18)}\\
l^2 - l^2 &= 0 \quad . &\text{(C.19)}
\end{aligned}$$

The equation C.18 is a second order linear differential equation. Hence, the solution is well-known as:

$$\Phi(\phi) = A\sin(l\phi) + B\cos(l\phi) \quad . \tag{C.20}$$

where A and B are constant coefficients. The equation C.17 is known as Bessel's differential equation. Hence, the solution is a linear combination of Bessel functions:

$$\frac{\rho^2}{R}\ddot{R} + \frac{\rho}{R}\dot{R} + k_c^2\rho^2 - l^2 = 0 \quad , \tag{C.21}$$

$$R(\rho) = CJ_n(k_c\rho) + DN_n(k_c\rho) \quad . \tag{C.22}$$

where $J_n(k_c\rho)$ is the Bessel function of the first kind of order n and $N_n(k_c\rho)$ is the Bessel function of the second kind of order n. In conclusion, the solution of the magnetic field function of ρ and ϕ can be written as:

$$B_0(\rho,\phi) = \Big(A\sin(l\phi) + B\cos(l\phi)\Big)\Big(CJ_n(k_c\rho) + DN_n(k_c\rho)\Big) \quad . \tag{C.23}$$

Due to the periodicity in which is $B_0(\rho,\phi) = B_0(\rho,\phi + 2\phi m)$ where m is the solution of the magnetic field, C.23 can be rewritten as:

$$B_0(\rho,\phi) = \Big(A\sin(m\phi) + B\cos(m\phi)\Big)\Big(CJ_n(k_c\rho) + DN_n(k_c\rho)\Big) \quad . \tag{C.24}$$

The Bessel function of the second kind of order n, $N_n(k_c\rho)$ diverges when ρ goes to zero which is the starting point at the waveguide. The constant coefficient of D, hence, should be equal to zero to get rid of the divergent case. Then, the solution C.23 turns into:

$$B_0(\rho,\phi) = \Big(A\sin(m\phi) + B\cos(m\phi)\Big)J_n(k_c\rho) \quad . \tag{C.25}$$

where C can be neglect due to being A, B, C are arbitrary constants [31].

APPENDIX D: BESSEL FUNCTION PLOT

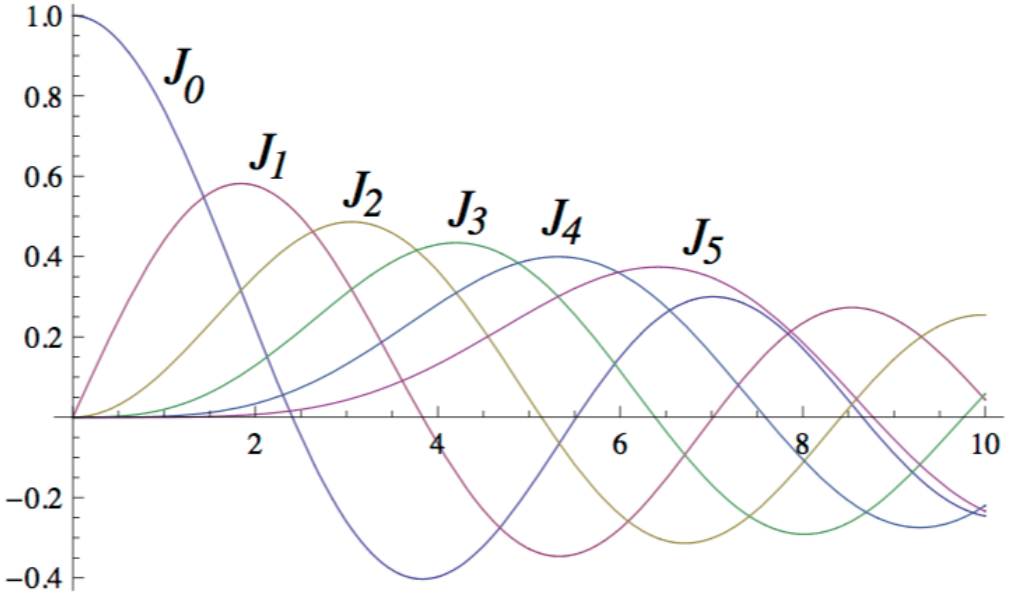

Figure D.1. Cylindrical Bessel Functions [5]

APPENDIX E: BPH ITSELF

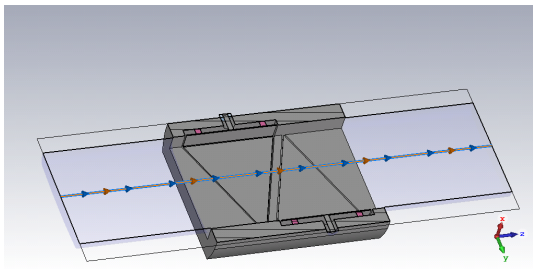

(a) Cut plane of the model including the shield - top view

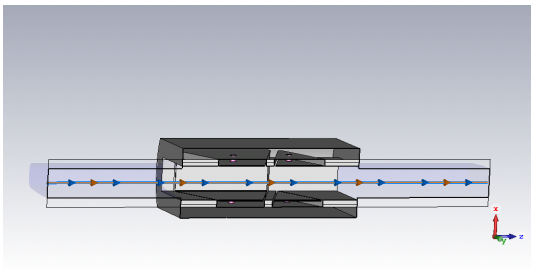

(b) Cut plane of the model including the shield - side view

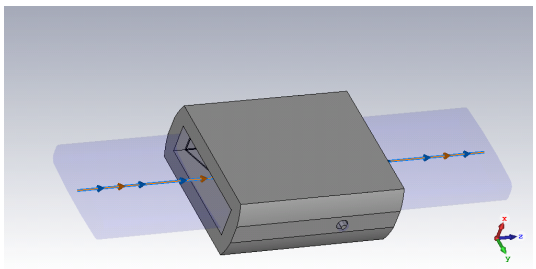

(c) Full 3D geometry in CST.

Figure E.1. BPH standalone model in CST MWS

APPENDIX F: IMPEDANCE PLOT AND EM-FIELD CONFIGURATIONS

Impedance Plot and EM-Field Configurations for the model with and without shield as well as BPH itself from Eigenmode Solver Results in CST MWS

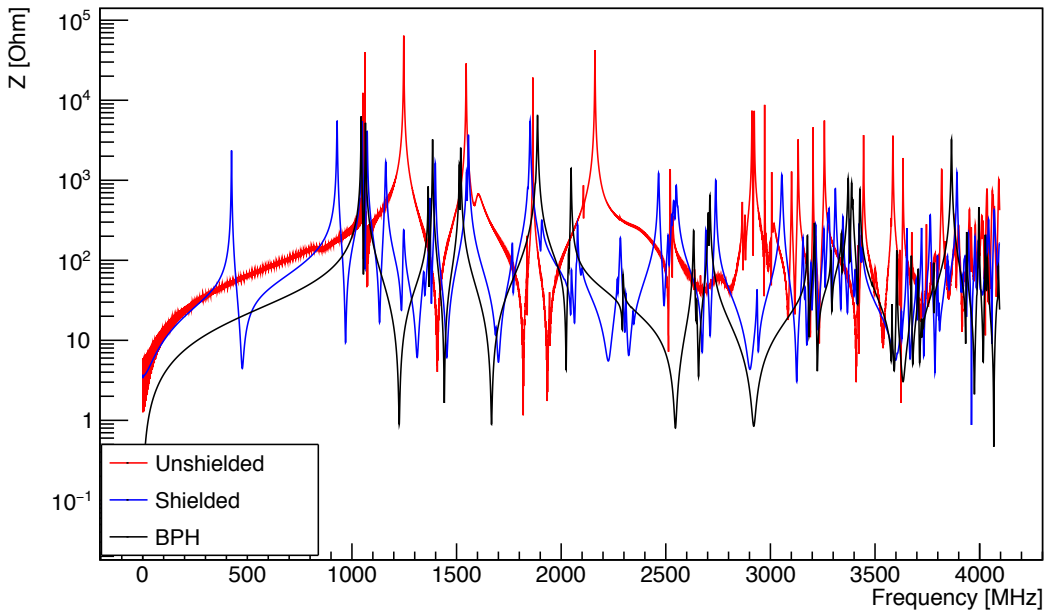

Figure F.1. Longitudinal beam impedance as a function for mode frequency obtained from wakefield simulation. BPH denote simulations without the BPH tank, the 10-convolution bellow and the vacuum flange.

Figure F.2. Electromagnetic configuration of specific resonance frequencies.

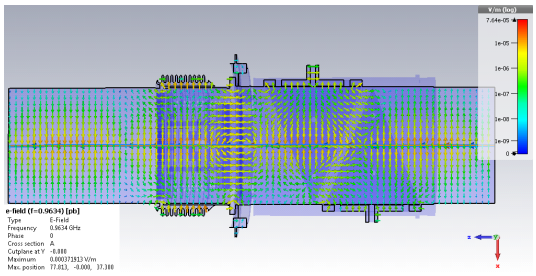

(a) 0.9634 GHz

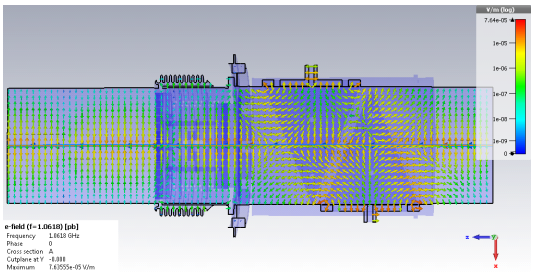

(b) 1.0618 GHz

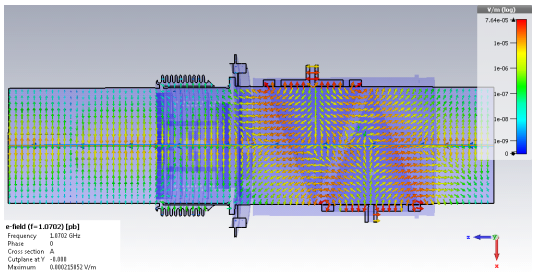

(c) 1.0702 GHz

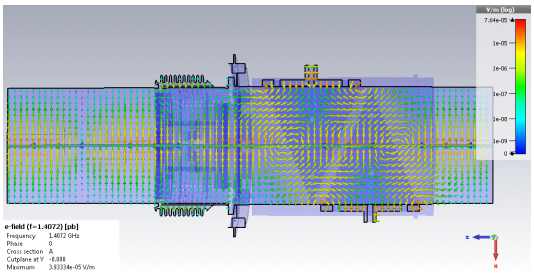

(d) 1.0906 GHz

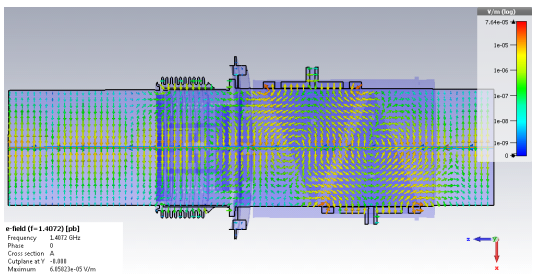

(e) 1.4072 GHz

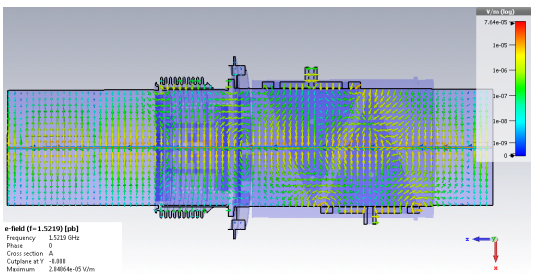

(f) 1.5219 GHz

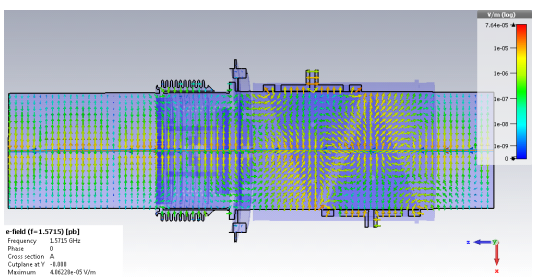

(g) 1.5715 GHz

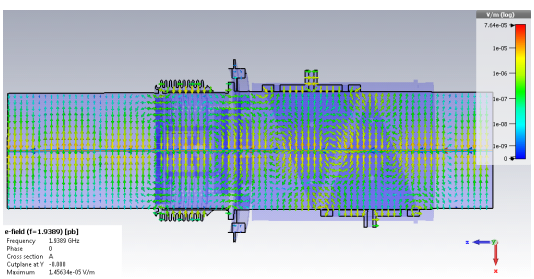

(h) 1.9389 GHz

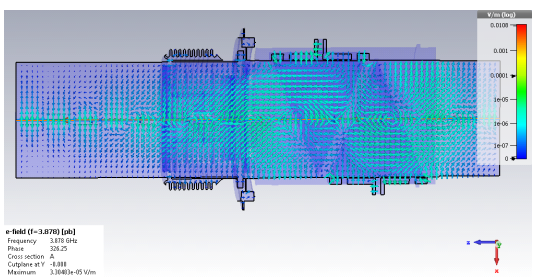

(i) 3.878 GHz

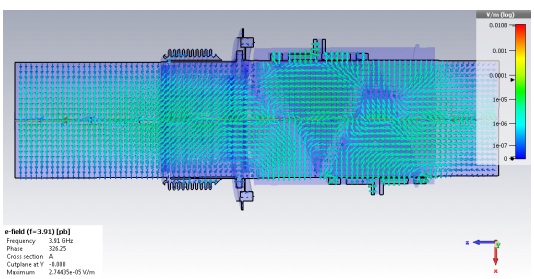

(j) 3.91 GHz

APPENDIX G: IMPEDANCE FUNCTION FOR FREQUENCY MODES

The term "resonator" is used to describe an object with a single resonance, for which the admittance is given by:

$$Y(j\omega) = \frac{1}{R} + j\omega C + \frac{1}{j\omega L} \quad . \tag{G.1}$$

Impedance is the reciprocal of admittance. Hence, impedance function can be written as:

$$\begin{aligned} Z(j\omega) &= \frac{1}{\frac{1}{R} + j\omega C + \frac{1}{j\omega L}} \quad , \\ &= \frac{R}{1 + j\omega CR + \frac{R}{j\omega L}} \quad , \\ &= \frac{R}{1 + j\omega CR\frac{\omega_{res}}{\omega_{res}} + \frac{R}{j\omega L}\frac{\omega_{res}}{\omega_{res}}} \quad , \\ &= \frac{R}{1 + jQ\frac{\omega}{\omega_{res}} + Q\frac{R}{j\omega}} \quad , \\ &= \frac{R}{1 + jQ\left(\frac{\omega}{\omega_{res}} - \frac{\omega_{res}}{\omega}\right)} \quad , \end{aligned} \tag{G.2}$$

where ω_{res} is the resonance frequency and Q-factor is equal to $Q = \frac{R}{\omega_{res}L} = R\omega_{res}C$. (One of the useful properties of the resonator impedance is the fact that it can be decomposed into linear fractions [13]).